

Analysis of Mechanical Properties of Crumpled Graphene: A Molecular Dynamics Approach

by

MD FARHAN - 1710035

MD SHAHED HOSSAIN SOHAN - 1710043

*A thesis submitted to the Department of Mechanical Engineering, BUET
in partial fulfilment of the requirements for the degree of Bachelor of Science
in
Mechanical Engineering*



BANGLADESH UNIVERSITY OF ENGINEERING AND TECHNOLOGY
DHAKA-1000, BANGLADESH
MAY 2023

CANDIDATE'S DECLARATION

It is hereby declared that this thesis/project or any part of it has not been submitted elsewhere for the award of any degree or diploma.

May 2023

MD FARHAN

Date:

MD SHAHED HOSSAIN SOHAN

Date:

Verified by:

Dr. Md. Ashiqur Rahman

Date:

Dedicated to our beloved parents.....

Table of Contents

List of Tables and Figures	vi
List of Tables and Abbreviations of Technical Symbols and Terms	vii
Acknowledgement	viii
Abstract.....	ix

CHAPTER 1	1
Introduction	1
1.1 Background	1
1.2 Graphene	2
1.2.1 Graphene Structure.....	3
1.2.2 Graphene synthesis.....	3
1.3 Crumpled Graphene	4
1.3.1 CG Synthesis.....	6
1.4 Literature Review	7
CHAPTER 2	12
Computational Methodology	12
2.1 Atomistic Simulation.....	12
2.2 Molecular Dynamics Simulation.....	13
2.2.1 Basic Introduction to LAAMPS.....	13
2.2.1.1 Modelling of the physical system	14
2.2.1.2 Lennard-Jones Potential.....	15
2.2.1.3 AIREBO Potential	16
2.2.1.4 Time Integration Algorithm.....	17
2.2.1.5 Verlet Algorithm.....	17
2.2.1.6 Units.....	18

2.2.1.7	Simulation Box and Boundary Conditions	19
2.2.1.8	Ensembles used in LAMMPS.....	21
2.2.2	Limitation of MD Simulations:	22
2.2.2.1	Uses of classical forces	22
2.2.2.2	Time and Size Limitations:.....	23
2.2.2.3	Reality of Forces:.....	23
2.2.3	General Procedure of Molecular Dynamics Simulations.....	24
2.2.4	System Modelling	24
2.2.4.1	Crumpled Graphene from 2D graphene sheet	24
2.2.4.2	Crumpling method of graphene	25
2.2.4.3	Molecular dynamics codes and utilities.....	28
2.2.4.4	Modelling of Porous Crumpled Graphene.....	28
2.2.5	Simulation method	29
2.2.5.1	Simulation Parameters	29
2.2.5.2	Relaxation	29
2.2.5.3	Tensile Loading	29
2.2.5.4	Elastic Modulus	31
2.2.5.5	Strain Energy	32
2.2.5.6	Compressive Loading	33
2.2.5.7	Timesteps	35
2.2.5.8	Temperature	35
CHAPTER 3		36
Results and Discussion.....		36
3.1	Graphene and CG under uniaxial tensile loading.....	37
3.1.1	Fracture under uniaxial tensile load on non-porous CGs.....	37
3.1.2	Fracture under uniaxial tensile load along y axis on porous CGs.....	40

3.1.2.1	Flat graphene ($r = \infty$) with different randomly added defect levels	40
3.1.2.2	Fracture under uniaxial tensile load on CG at $r = 24.3 \text{ \AA}$	42
3.1.2.3	Fracture under uniaxial tensile load on CG at $r = 19.3 \text{ \AA}$	43
3.1.2.4	Fracture under uniaxial tensile load on CG at $r = 14.7 \text{ \AA}$	45
3.1.2.5	Fracture under uniaxial tensile load on CG at $r = 12.3 \text{ \AA}$	46
3.1.2.6	Fracture under uniaxial tensile load on CG at $r = 7.6 \text{ \AA}$	48
3.1.3	Comparison in light of elastic modulus under uniaxial tensile load on non-porous CGs	50
3.1.3.1	Effect of elastic modulus on non-porous CG with varying radius	50
3.1.3.2	Effect of elastic modulus on non-porous CG with varying porosity	52
3.1.4	Strain Energy analysis under tensile deformation.....	61
3.1.4.1	Strain energy in non-porous crumpled graphene.....	61
3.1.4.2	Variation in strain energy in porous crumpled graphene.....	64
3.1.5	CG under Uniaxial Compressive Load	69
3.1.5.1	Fracture under Uniaxial Compressive Load on Non-porous CGs along x-axis	69
3.1.5.2	Fracture under Uniaxial Compressive Load on Non-porous CGs along y-axis	73
3.2	Validation	75
CHAPTER 4		78
Conclusion and Future Recommendations		78
4.1	Conclusion.....	78
4.2	Future Recommendations.....	79

List of Tables

Table 1. Number of atoms of graphene sheet that is crumpled per defect level.	28
Table 2. Crumpleness radius and %porosity that has been considered for Tensile test.	36
Table 3. Fracture toughness at different levels of crumpling radius, where lower radius means more crumpling.	38
Table 4. Fracture toughness of flat graphene with different defect levels under uniaxial tensile loading along y axis.	42
Table 5. Fracture toughness in GPa for CG with 24.3 Å crumpling radius at different levels of porosity.	42
Table 6. Fracture toughness in GPa for CG with 19.3 Å crumpling radius at different levels of porosity.	44
Table 7. Fracture toughness in GPa for CG with 14.7 Å crumpling radius at different levels of porosity.	46
Table 8. Fracture toughness in GPa for CG with 12.3 Å crumpling radius at different levels of porosity.	47
Table 9. Fracture toughness in GPa for CG with 7.6 Å crumpling radius at different levels of porosity.	49
Table 10. Fracture toughness in GPa for CG at different crumpling radius at 10% and 20% porosity.	50
Table 11. Graphene states under uniaxial tensions along x, y, z direction.....	60
Table 12. Different stages of CG at crumpling radius of 7.6 Å under uniaxial compressive loading along x.	71
Table 13. CG under compressive loading along y.	74
Table 14. Young's modulus values reported in previous articles.	76

List of Figures

Figure 1. Schematic of different types of corrugated graphene. (a) Rippled graphene; (b) wrinkled graphene and (c) crumpled graphene.[23].....	5
Figure 2. Interaction potential as a function of distance between two adjacent molecules in Lennard-Jones Potential.[68]	15
Figure 3. Hexagonal lattice of a 5nm x 5nm graphene sheet, the armchair position is placed vertically.	25
Figure 4. Crumpling a graphene sheet (50Å x 50Å) step by step.	27
Figure 5. Diagram of an MD simulation model for displacement-controlled tensile tests. The boundary layer on the right is movable, but the boundary layer on the left is fixed (blue).	30
Figure 6. Application of displacement control method for uniaxial tensile loading along z axis in a non-porous crumpled graphene domain.....	31
Figure 7. Arrangement for uniaxial compression testing of crumpled graphene (7.6 Å) by applying displacement control method.	34
Figure 8. Variation of stress as a function of strain at different levels of crumpling in non-porous condition of graphene under uniaxial tensile loading along y axis. (Radius in Å)	38
Figure 9. Gradual deformation under tensile loading for states I to V for a CG with radius of 7.6 Å, where state IV is the maximum fracture point.	39
Figure 10. Gradual deformation of CG having crumpling radius 12.3 Å from initial (I') state to maximum stress state (III''), where at state III' the CG is under maximum stress.....	40
Figure 11. Variation of stress as a function of strain for flat graphene at different amount of porosity under uniaxial tensile loading along y axis.....	41
Figure 12. Variation of stress as a function of strain for CG with 24.3 Å crumpling radius	43
Figure 13. Variation of stress as a function of strain in case of a CG with a crumpling radius of 19.3 Å at different levels of porosity under uniaxial tensile loading along y axis.	44

Figure 14. Variation of stress as a function of strain in case of a CG with a crumpling radius of 14.7 Å at different levels of porosity under uniaxial tensile loading along y axis.	45
Figure 15. Variation of stress as a function of strain in case of a CG with a crumpling radius of 12.3 Å at different levels of porosity under uniaxial tensile loading along y axis.	47
Figure 16. Variation of stress as a function of strain in case of a CG with a crumpling radius of 7.6 Å at different levels of porosity under uniaxial tensile loading along y axis.	49
Figure 17. Variation in Elastic Modulus (GPa) with a change in crumpling radius (Å) for different grades (%) of porosity under uniaxial tensile loading along y axis.....	52
Figure 18. Variation of elastic modulus with % of porosity in electrode at different degree of crumpling under uniaxial tensile loading along y axis.....	53
Figure 19. (c) Variation of elastic modulus with % of porosity in crumpled graphene with $r = 12.3$ Å under uniaxial tensile loading along y axis.	57
Figure 20. Variation of stress with strain for 7.6 Å CG for uniaxial tension added towards x, y and z directions under uniaxial tensile loading along y axis.	58
Figure 21. Variation of strain energy in non-porous crumpled graphene with applied strain at different degree of crumpling under uniaxial tensile loading along y axis..	61
Figure 22. (a) Variation of strain energy in non-porous crumpled graphene with applied strain for flat graphene under uniaxial tensile loading along y axis.....	62
Figure 23. (b) Variation of strain energy in non-porous crumpled graphene with applied strain at $r = 7.6$ Å under uniaxial tensile loading along y axis.	63
Figure 24. Variation of strain energy in Flat graphene with applied strain at different degree of porosity under uniaxial tensile load along y axis.	64
Figure 25. Variation of strain energy in crumpled graphene with applied strain at different degree of porosity with crumpling radius 19.3 Å under uniaxial tensile load along y axis.	65
Figure 26. Variation of strain energy in crumpled graphene with applied strain at different degree of porosity with crumpling radius 14.7 Å under uniaxial tensile load along y axis.	66

Figure 27. Variation of strain energy in crumpled graphene with applied strain at different degree of porosity with crumpling radius 12.3 Å under uniaxial tensile load along y axis.	67
Figure 28. Variation of strain energy in crumpled graphene with applied strain at different degree of porosity with crumpling radius 7.6 Å under uniaxial tensile load along y axis.	68
Figure 29. Variation of stress as a function of strain under uniaxial compressive loading for a non-porous CG of radius 7.6Å along x direction.	69
Figure 30. Variation of stress as a function of strain under uniaxial compressive loading for a non-porous CG of radius 7.6Å along x axis.	70
Figure 31. Variation of stress as a function of strain under uniaxial compressive loading for a non-porous CG of radius 7.6Å along y axis.	73
Figure 32. Variation of stress with applying strain along the armchair direction on a flat graphene for uniaxial tensile load along armchair direction.....	76

List of Abbreviations of Technical Symbols and Terms

MD	Molecular Dynamics
CG	Crumpled Graphene
CR	Crumpling Radius
LAMMPS	Large-scale Atomic/Molecular Massively Parallel Simulator
np	Non-porous
SSA	Specific Surface Area
F	Interacting force between atoms in N
m	Mass of individual atom
a	Acceleration of atom
ε	Bonding/dislocation energy function
σ	Finite distance at which potential between two particles becomes zero
r	distance between two particles
ts	Timestep
n_c	Number of current steps
n_e	Number of steps at equilibrium
r	Radius of Crumpleness current step
r_0	Initial radius
x_{lo}, y_{lo}, z_{lo}	Minimum value of the coordinates x, y, z.
L_0	Initial Box length before applying strain

Acknowledgement

We would like to start by giving our profound thanks to Almighty ALLAH, for giving us the motivation, fortitude, and skills necessary to complete this thesis project.

We sincerely thank Dr. Md. Ashiqur Rahman, Professor in the Department of Mechanical Engineering at BUET, who served as our thesis advisor, for his constant support, mentorship, priceless advice, and astute ideas during this study. The successful completion of this difficult task would not have been possible without his creative solutions, encouragement, and thorough oversight.

There are some persons who have supported this initiative in numerous direct and indirect ways. We would like to thank Tousif Jamee Hemel and Sazid Noor Rabi bhai for their constant support.

We would like to thank all others who are directly or indirectly related to this thesis by sharing their ideas, suggestions and finally by supporting us. We would like to express our warmest gratitude to our family members - our mother, father and brother for their continuous inspirations, moral supports and immeasurable sacrifices during this project.

Abstract

Graphene has attracted a great deal of interest due to its extraordinary mechanical properties, which find use in a variety of fields including electronics, energy storage, and composites. Crumpled graphene (CG) has special qualities such as high surface area, conductivity, and aggregation resistance. These characteristics indicate why it has a higher capacitance than flat graphene sheets, which frequently have lower surface area as a result of aggregation. Up to a certain percentage of porosity in CG can increase the energy storage performance of CG based supercapacitors. This work examines mechanical characteristics of crumpled graphene (CG) and a molecular dynamic study is carried out into how different parameters affect these mechanical properties. To figure out their impact on the material's response, factors like the amount of crumpling, the size and structure of the crumpled regions, and the characteristics of the underlying substrate are examined. In this study, CG formed from a single graphene sheet (5 nm x 5 nm) is considered and studied using LAMMPS under Molecular Dynamics (MD) environment. Results show that mechanical properties e.g., fracture toughness, elastic modulus, strain energy under tensile loading are severely affected by the porosity and crumpling stage of CG structure. With increased crumpling of graphene, the fracture toughness first drops, but after exceeding a certain threshold (14.7 Å), begins to rise. The Vander Waals forces between the graphene layers cause the strength of CG to increase, with the maximal fracture toughness being noted at a crumpling radius of 7.6 Å, which is 49.5 GPa. CG's mechanical properties are strongly impacted by the existence of porosity as well. A comparison of porous and non-porous CG shows that the porous CG displays lower fracture toughness, which indicates lesser fracture resistance. The mechanical properties of flat graphene are significantly influenced by even minor porosity. However, with higher grades of crumpling i.e., lower crumpling radius has lesser effect of porosity on its mechanical performance. The CGs with radius 12.3 Å and 7.6 Å showed almost similar mechanical characteristics at 10% and 20% defect levels. The study further looks at the effect of porosity on the ability of crumpled graphene to store strain energy. It is found that the quantity of strain energy that may be stored is decreased by the presence of pores in CG. To obtain the optimum performance, the porosity content needs to be carefully adjusted. Additionally, how crumpled graphene responds to a uniaxial compressive load is also studied. It is found that when crushed along the X-axis, CG cracks and deforms plastically. The minimum stress needed for fracture being around 11 GPa. Compression along y axis shows higher fracture resistance and deforms

plastically around 25 GPa. The loading unloading phenomenon depends on the morphology of the CG structure. Because of irreversible or inelastic deformation, the unloading curve does not travel in the same direction as the loading curve.

Overall, this study offers considerable insight regarding the mechanical characteristics of crumpled graphene. The development of graphene-based materials with specialized mechanical properties for various purposes can be facilitated by an understanding of the fracture behavior and the effects of porosity of CG.

CHAPTER 1

Introduction

1.1 Background

With the advent of bulk nanomaterials based on carbon nano-polymorphs, the study of materials physics just achieved an important milestone. These developments have made it possible to investigate innovative nanoscale structures in fascinating new ways. Among these advancements, the creation of three-dimensional (3D) graphene nanostructures has attracted a lot of interest, stoking the flames of this developing field of study. Many researchers have been trying to synthesize and study the performance of these bulk materials. Zhang et al.[1] offered a straightforward, environment friendly process for creating porous materials based on three-dimensional graphene with an ultrahigh SSA (3523 m²/g) and outstanding bulk conductivity, which demonstrate superior supercapacitor performance (specific capacitance of 231 F/g, energy density of 98 Wh/kg). Levchenko et al.[2] reported a revolutionary method for producing high-quality graphene flakes on a wide scale uses magnetically accelerated arc discharges between carbon electrodes. Carbon structures with unique electrical, mechanical, and thermal properties are of great interest today.[3-6]

Crumpled sheet materials represent a new class of structures attracting a great interest because of their unique mechanical and physical properties. Such materials seem to be very promising for applications in the fields where extremely large specific surface area is required.[7]

To meet the world's ever-increasing energy demands, we must turn to alternative, renewable energy sources due to changing weather patterns, depletion of fossil fuels, and unequal distribution of energy sources. To cope with such a shifting energy paradigm, it is necessary to develop and implement economical, efficient, and dependable energy storage technologies in order to harvest energy from infinite but intermittent renewable energy sources such as wind, tidal, and sunlight.

There are various types of energy storage devices, but electrochemical energy storage technologies are the most viable, environmentally friendly, and long-term clean energy solutions. Batteries, capacitors, and fuel cells are the most common commercial energy storage systems today. There are mainly two types of charge storage mechanisms. They are: (a)

Electrostatic storage at intersection of capacitor electrode as electric double layer capacitance, (b) Faradaic storage at electrode surface as pseudo capacitance. Although batteries have high power density but for slow power capability they are ruled out from many application[8]. The use of 'Electrochemical capacitors,' also known as supercapacitors or ultracapacitors, could be a potential solution to this problem. Supercapacitors have sparked a lot of interest due to their fast charge/discharge rate, long life cycle, and high power density[9].

The problematic issue that supercapacitors face is their low energy density. So increasing energy density of supercapacitor becomes a prominent factor. Researchers continued experiment to enhance the performance of supercapacitors using different electrode materials. Because of its high thermal and electrical conductivity and high specific area, graphene is the most commonly used electrode material [10]. Graphene electrode shows positive response to increase energy storage[11]. Capacitance of graphene-based electrode can be increased by modification of surface geometry of electrode. Tarek et al. recently discovered a significant increase in capacitance with a wrinkled flower-like graphene structure[12]. Recent research suggests that crumpled graphene based electrode material can improve the interaction between electrode and electrolyte[13].

1.2 Graphene

Graphene is a single layer of carbon atoms arranged in a hexagonal lattice. It is the thinnest and strongest material ever known, and it has a wide range of potential applications in electronics, energy, and other fields.

Graphene was first isolated in 2004 by Andre Geim and Konstantin Novoselov at the University of Manchester, and they were awarded the Nobel Prize in Physics in 2010 for their work. Graphene is made from graphite, the same material that is used in pencils. Graphite is made up of many layers of graphene, and it can be separated into individual layers by a variety of methods, including mechanical exfoliation and chemical vapor deposition[14].

Graphene has a number of unique properties that make it a promising material for a wide range of applications[15]. It is strong, lightweight, and transparent. It is also an excellent conductor of

heat and electricity. Graphene is also very flexible and can be easily processed into different shapes and sizes.

1.2.1 Graphene Structure

Graphene is a single layer of carbon atoms arranged in a hexagonal lattice. It is a two-dimensional material, which means that it has thickness but no width or length. Individual graphite layers make up the two-dimensional structure known as graphene. The interplanar distance between each layer of graphene is 3.35 Å, and the length of the C-C bond is 0.142nm. It consists of three σ -bonds and one π -bond. This allows the electron cloud to move around freely, which contributes to graphene's exceptional electrical conductivity. Compared to most metals, graphene has a higher electrical and thermal conductivity. Graphene is the thinnest and strongest material ever known, and it has a wide range of potential applications in electronics, energy, and other fields.

Each carbon atom in graphene is covalently bonded to three other carbon atoms, forming a hexagonal lattice. The carbon atoms are sp^2 hybridized, which means that they have one unhybridized p-orbital. The unhybridized p-orbitals of the carbon atoms overlap to form π bonds, which are responsible for the unique properties of graphene.[16]

Graphene is a very strong material. It has a Young's modulus of 1 TPa, which is about 200 times stronger than steel.[17] Graphene is also very flexible. It can be stretched to twice its original length without breaking.

Graphene is an excellent conductor of heat and electricity. It has a thermal conductivity of 5300 W/mK, which is about twice that of copper. Graphene also has an electrical conductivity of 60000 S/m. Graphene is a very transparent material. It has a transparency of about 97%, which is comparable to that of glass.[18]

1.2.2 Graphene synthesis

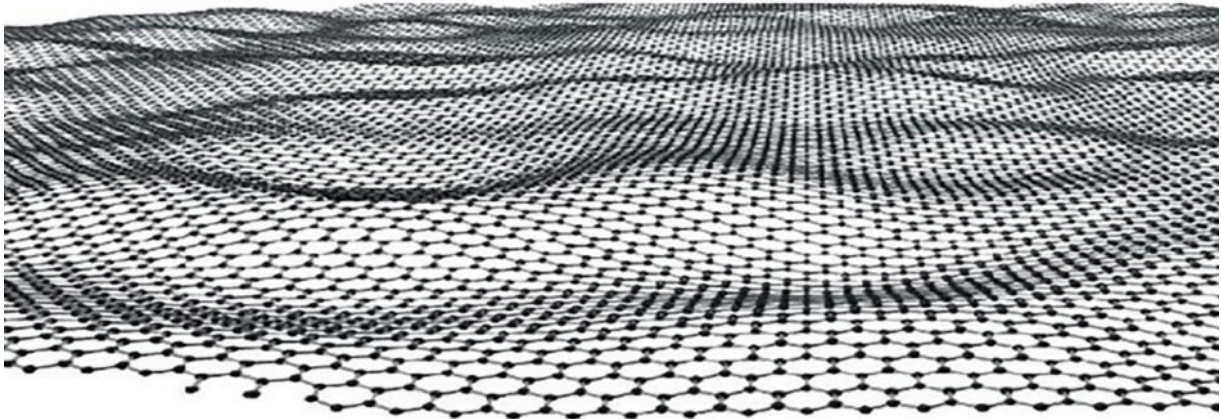
There are a number of different methods for synthesizing graphene. The most common methods are:

- **Mechanical exfoliation:** This method involves using a scotch tape to repeatedly peel off layers of graphite until a single layer of graphene is left.[19]
- **Chemical vapor deposition:** This method involves depositing carbon atoms on a substrate in a high-temperature environment. The carbon atoms then arrange themselves into a single layer of graphene.[20]
- **Epitaxial growth:** This method involves growing graphene on a substrate that has a similar crystal structure. The graphene then grows in the same direction as the substrate, resulting in a single layer of graphene.[21]

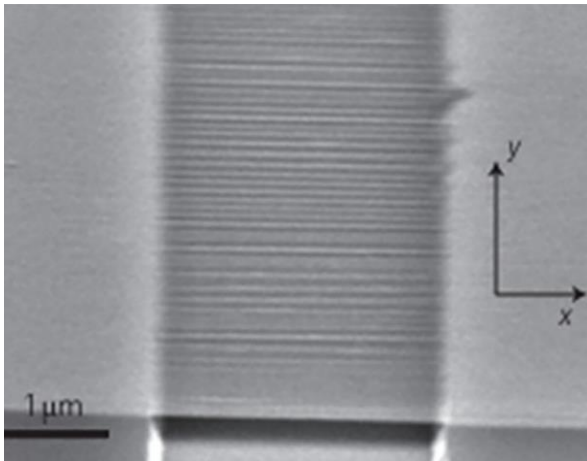
Each of these methods has its own advantages and disadvantages. Mechanical exfoliation is the simplest method, but it is also the least scalable. Chemical vapor deposition is more scalable, but it requires high temperatures and can be expensive. Epitaxial growth is the most scalable and controllable method, but it requires a substrate with a suitable crystal structure. To create graphene with a controllable number of layers, a large surface area, and good quality, CVD is currently used extensively.

1.3 Crumpled Graphene

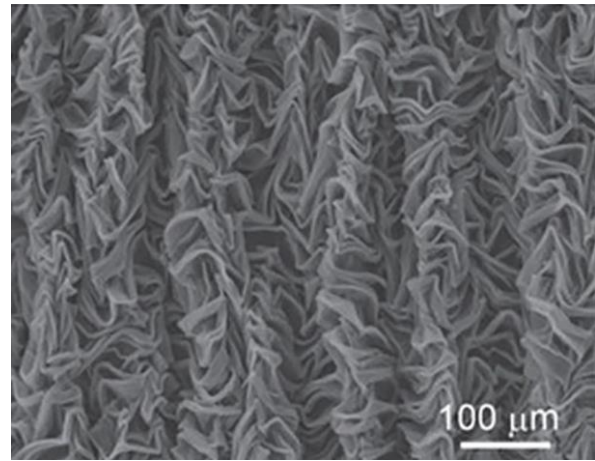
Surface corrugation on graphene can modify its properties. Deng et al. categorized the surface corrugation as wrinkles, ripples and crumples based on their aspect ratio, physical dimensions, topology and order. Wrinkles and ripples predominantly manifest on a two-dimensional plane. Wrinkles exhibit a high aspect ratio, with widths ranging from one to tens of nanometers, heights below 15 nm, and lengths exceeding 100 nm (aspect ratio > 10). In contrast, ripples possess a more isotropic nature, characterized by valleys and peaks with feature sizes below 10 nm (aspect ratio ~ 1) (**Figure 1**). On the other hand, crumples represent densely formed deformations, resembling folds and wrinkles, occurring isotropically in either two or three dimensions, akin to crumpled paper.[22]



(a)



(b)



(c)

Figure 1. Schematic of different types of corrugated graphene. (a) Rippled graphene; (b) wrinkled graphene and (c) crumpled graphene.[23]

The three-dimensional deformations of graphene known as crumples are dense. A dense deformation of a graphene sheet called crumpled graphene happens isentropically.[24] This compact deformed structure is the result of multidirectional compressive force. Deformation of graphene is influenced by mechanical parameters like tensile strength, Young's modulus, and the number of layers. Importantly, we have the ability to manipulate and fine-tune graphene's physical properties, such as wettability, transmittance, chemical potential, and conductivity, by regulating the extent of deformation.

Due to their distinct mechanical and physical properties, crumpled sheet materials represent a novel class of structures that are generating a lot of interest. These substances appear to hold great promise for use in domains that demand exceptionally large specific surface areas.[7] For certain encouraging findings and emerging possibilities, exploration of crumpled graphene structures is one of the most recent fields in current materials science.[25] One of the most significant findings is that crumpling, which can be produced commercially at a reasonable cost, eliminates layer stacking followed by the transition to graphite.[26]

1.3.1 Crumpled Graphene Synthesis

Due to graphene's incredible flexibility, researchers have been actively debating how to controllably create ripples, folds, or wrinkles in the material, as well as how to make use of these corrugations.[27]

- Aerosol spray drying method
- Hydrothermal method
- Thermal reduction of graphene oxide method
- Mechanical method

Luo et al. described how crumpled graphene balls were created using capillary compression in rapidly evaporating aerosol droplets.[28] The high-temperature-induced rapid evaporation of graphene oxide (GO) droplets leads to their shrinkage, resulting in the formation of crumpled GO nanostructures resembling crumpled paper balls. Crumpled graphene sheets have garnered significant attention from researchers due to their unique characteristics, making them suitable for use in energy-related devices, especially where a high specific surface area (SSA) is desired. The impact of structural deformations on various properties has been investigated both theoretically and experimentally. While the SSA of flat GO sheets was less than 5 m²/g, crumpled GO sheets exhibited an SSA of 82 m²/g, demonstrating the substantial increase in surface area offered by the crumpled structure. This enhanced surface area is a crucial factor for the development of graphene-based supercapacitor electrodes.[28] Tang et al. utilized an aerosol spray technique to create crumpled graphene structures. They combined graphene oxide (GO) sheets with KOH and subjected the mixture to thermal reduction to induce crumpling. Additionally, they investigated the crumpling process by employing an aerosol spray technique

with water as the medium. This approach allowed for the controlled formation of crumpled graphene.[29] Steven et al. conducted a study to assess the potential capacitance of graphene-based ultracapacitors by examining the packing efficiency and accessible surface area of crumpled graphene. The investigation focused on understanding how the crumpling process impacts the electrode's performance in terms of capacitance. By analyzing the packing efficiency and surface area of crumpled graphene, the researchers aimed to gain insights into its electrochemical properties and its suitability for ultracapacitor applications. The findings of this study contribute to the understanding and development of high-performance graphene-based ultracapacitors.[30] Becton et al. conducted a molecular dynamics simulation to investigate the crumpling phenomenon in nanosheets of graphene induced by confinement.[31]

1.4 Literature Review

Tsai and Tu compared graphene sheet and graphite flakes and found graphene sheet have higher modulus than graphite flakes[32]. They suggested that exfoliation of graphite flakes into graphene layers is required for improved mechanical properties of graphite-reinforced nanocomposites. To find Young's modulus and Poisson's ratio they applied two approach axial stress and axial strain on the simulation box using NPT and NVT ensemble respectively. Ranjbartoreh et al. experimentally investigated Graphene paper application in engineering[33]. They used three tests like tensile, indentation and bending tests to find mechanical properties of graphene paper. During bending tests graphene paper showed outstanding bending rigidity and elastic modulus. Crumpled particles exhibit strain-hardening behaviors, making them exceptionally resistant to aggregation in both solution and dried states investigated by Luo et al. using capillary compression[34].

Cranford and Buehler studied stable crumpled graphene for different length and determined once crumpled, 60% of graphene's specific surface area is solvent accessible and can be tuned with applied compression and crumpling[35]. Chang et al. found that the size, functionalization, and defects all have a significant influence on the phase transition between a flat-membrane phase and a crumpled phase[36]. Crumpled graphene is used in consumer electronics and hybrid vehicles[37] because the crumpling process can be tailored to the device's intended application.

The most effective method has been proven to be the conversion of two-dimensional graphene sheets to three-dimensional crumpled graphene structure to increase surface area of graphene.

Zang et al. demonstrated a method reversible and unfold large graphene area and observed properties of graphene in a controlled manner[38]. They observed improvement of superhydrophobicity, high transparency, tunable wettability and transmittance property of graphene. The crumpled graphene ridges and vertices are highly deformed and microscopically patterned, which could lead to new properties and functions such as patterned chemical reactions.

Baimova et al. reviewed on crumpled graphene mechanical property[39] and stated that due to extremely high specific surface area, high conductivity and stability against graphitization crumpled graphene material can be used as electrode in supercapacitor, ultracapacitor, electronics and energy storage devices. Montazeri et al. simulated hydrogenated graphene to characterize the stability behavior of graphene[40]. They suggested that when analyzing the mechanical and loadbearing properties of nanodevices made from these nanostructures, the coverage dependent stability behavior of hydrogenated graphene nanoribbons should be taken into account.

Becton et al. conducted a simulation to compare polycrystalline graphene with pristine graphene under some geometric confinement while crumpling process was kept same[41]. They found that average grain size of crumpled polycrystalline graphene has a slight negative correlation with measured hardness, bulk modulus, and crumpled size. Zang et al.[42] explored that supercapacitor electrodes made from crumpled graphene papers have a unique combination of high stretchability, high electrochemical performance specific capacitance, and high reliability. Baimova et al. investigated mechanical responses of new bulk carbon nanostructures under hydrostatic pressure or shear strain[43].

Baimova et al. estimated mechanical response of crumpled graphene under hydrostatic compression and uniaxial compression[44]. They observed crumpled graphene as a non-Hookean medium showing non-linear stress-strain relationship even for small strain.

Nicholl et al. experimentally observed that temperatures below 400 K, graphene softens due to static wrinkling, with only a minor contribution from flexural phonons[45]. They observed that when the strain is less than 10%, the droplet contact angle increases linearly with increasing biaxial tensile strain and it remains stable if strain is larger than 10%. Yamaletdinov and Pershin used pull and release experiment by removing stretching force from single layer graphene[46].

Katin et al. described system bending behavior of nickel coated graphene by carbon-nickel interaction, rather than the individual properties of isolated graphene and nickel films[47]. Xia et al. demonstrated[48] that at elevated temperatures, bulk graphene materials exhibit a fluid-like behavior similar to linear polymer melts, and these materials transform into a glassy-like "foam" state at temperatures below their glass-transition temperature. Special high-temperature treatment was discovered to be an efficient method of fabricating metal-carbon nanocomposites[49].

Hydrostatic compression at high temperatures ranging from 1000 to 2000 K improves the mixing of Ni atoms within the structure and results in the formation of strong covalent bonds between neighboring flakes[49]. Effect of temperature on the Young's modulus and shear modulus of armchair and zigzag carbon nanotubes were studied[50]. It was found that strain energy density of single-walled carbon nanotubes (SWCNTs) decreases with the increase of temperature as well as Young's modulus increases with tube diameter while decreasing with temperature[50]. Using Atomic Force Microscopy, mechanics of crumpled graphene and graphene oxide nanostructures using force indentation routines was investigated[51]. It also observed that crumpled graphene and crumpled graphene oxide exhibit a multi-regime power law deflection response with exponents ranging from 1.2 to 2.5[51].

Different types of interatomic potential are used to characterize performance of graphene electrode depends on metal type which will interact with graphene due to binding energy hold by the bond[52]. The power-law scaling relationships with the radius of spherical confinement volume can be used to predict structural properties such as radius of gyration, hydrodynamic radius, and viscometric radius during the crumpling of graphene sheets of various sizes[53]. Function of radial distribution calculated for the graphene-polypyrrole systems revealed a strong,

but non-chemical bonding interaction[54]. Within the specified temperature range, the interaction energy of binary systems exhibits a linear relationship[54].

Baimova et al. examined the impact of temperature and stress on the mechanical characteristics of carbon nano polymorphs, emphasizing the materials' resistance to compression as well as the possibility of improving stiffness and strength via thermo mechanical processes[55]. Future work should focus on researching graphene flakes with flaws and looking at how shear deformation affects the production of new carbon structures. A size-effect rule and a multifractal scaling law govern the yield strength of graphene, according to research by Javvaji et al. using molecular dynamics simulations to examine the effects of domain size, crack length, and lattice orientation[56]. The findings shed light on the yield behavior of the Graphene under study by demonstrating how shorter starting crack lengths, greater domain sizes, and certain lattice orientations affect yield values.

Zhang et al. successfully created graphene fibers that resembled experimental materials and pinpointed interlayer slipping/shearing and nanocrack initiation as important deformation mechanisms[6]. The results offered suggestions for creating high-performance fibers and help to understand how graphene fibers behave. The graphene helicoids (GH) investigated by Zhan et al. demonstrated their high yield strain and full recovery capability[57]. Geometrical parameters can be used to predict the tensile behavior and critical forces of the GH, making them suitable candidates for nanoscale elastic springs.

Through simulations, Liao et al. investigated the crumpling of graphene sheets and discovered elastic bending, self-adhering, and compression mechanisms[53]. Insights for designing and engineering crumpled materials were gained from the identification of scaling relationships and size-dependent structural features. Using molecular dynamics simulations, Valentini et al. looked at the structural behavior of compressed nanoparticles[58]. The outcomes demonstrated a phase-transition plasticity method via the inverse change of the particles from a compressed condition to their initial shape. This discovery corroborates experimental findings and sheds light on the behavior of silicon nanoparticles.

Molecular dynamics simulations of nanoindentation on multilayered thin films were presented by Fang and Wu[59]. The findings indicate mechanical twins and slide lines in the material as well as depth-dependent adhesion and maximum load as well as temperature-induced fluctuations in indentation load. In order to ascertain the material characteristics and constitutive models for the mineral Jennite in cement paste, Muril et al. provided a molecular dynamics modeling methodology[60]. In order to improve predictions of the isothermal bulk modulus and mechanical reaction, the results showed correlations between pressure, specific volume, and specific internal energy. By examining the impact of size and shape on plasticity mechanisms, Kilymis et al. studied the mechanical response of silicon nanoparticles to compression[61]. The results highlight the necessity of additional research in covalent and metallic materials by illuminating the intricate connection between nanoparticle shape and the commencement of flexibility.

Zhang et al. examined the compressibility and molecular characteristics of nitrate energetic materials during hydrostatic and uniaxial compression, shedding light on their behavior and offering potential future research topics for comprehending and creating such materials[62]. In order to better understand and synthesize nitrate energetic materials, Baimova et al. looked at the compressibility and molecular characteristics of these materials during hydrostatic and uniaxial compression[63].

Porosity is another parameter to be investigated along crumpleness as it also increases graphene electrode performances.[64-66] The introduction of porosity in crumpled graphene structures increase surface area for electrochemical reactions, enhancing overall performance. Methods like sacrificial templates or additives create voids and pores. Porous crumpled graphene allows faster diffusion of ions or reactants, improving mass transport. Porosity and crumpled morphology provide mechanical stability, preventing collapse. Investigating porosity alongside crumpleness optimizes electrochemical performance, impacting efficiency and cyclability.

This thesis work is motivated by the lack of previous studies analyzing the mechanical properties of crumpled graphene with both porous and non-porous structures. Thus, the aim of this research is to investigate the mechanical characteristics of crumpled graphene in relation to its porosity, filling an important gap in the existing knowledge.

CHAPTER 2

Computational Methodology

Computer simulation enables researchers to explore a system's behavior under certain initial conditions, bridging the gap between theory and experiment. Simulations are getting more sophisticated and realistic as a result of developments in computer technology and the creation of cutting-edge graphical user interfaces, allowing researchers to more accurately and intricately replicate real-world processes. As a result, computer simulation has developed into a crucial tool for research and experimentation in science.

2.1 Atomistic Simulation

Computer simulations provide a methodology for detailed modeling of complex systems and atomistic simulation occupies an important position among other simulation methods. Ab initio calculation is a quantum mechanics method that can be used to determine the properties of a system, and it is useful in the design of advanced materials or medicine. However, it is computationally inefficient and can only be applied to treat systems with fewer than 100 atoms. To study large molecular systems beyond the limits of ab initio calculations, nonquantum mechanics simulation methods should be adopted, which utilize an empirical force field to describe the atomic interactions. The Monte Carlo simulation and the MD simulation are the most widely applied methods in atomistic simulation.

The Monte Carlo approach uses probability distributions based on statistical mechanics concepts to derive statistical thermodynamic properties from atoms, which are treated as single point masses with random movements. It is helpful in dealing with phase change processes and complicated systems, but it can only forecast dynamic properties related to nonequilibrium processes precisely at equilibrium levels.

The MD simulation method, which can offer both statistical and dynamic aspects of a system, describes atom movement using classical mechanics. It is more straightforward and computationally efficient than quantum mechanics approaches, accurate, and applicable to a wide range of material systems. For various molecular systems, multiple force fields have been

developed, and with faster computing power, MD simulations will be able to mimic larger and more complex systems.

2.2 Molecular Dynamics Simulation

As a technique for particle tracing, molecular dynamics is typically divided into three main components[67]:

- i. Assuming that the interatomic potential has a known function, the model's initial step is to describe it. The molecular modeling and force field potentials sections will cover this topic later.
- ii. The second method requires numerically calculating the equations of motion directly using a time integrator.
- iii. The third involves obtaining measurable thermodynamic parameters from systems with numerous particles and degrees of freedom by employing statistical ensembles.

The system follows the classical Newton's laws of motion in an MD simulation. For a molecular system with N interacting particles, if the position vector and momentum vectors are denoted as $\mathbf{r}^N = (\mathbf{r}_1, \mathbf{r}_2, \dots, \mathbf{r}_N)$ and $\mathbf{p}^N = (\mathbf{p}_1, \mathbf{p}_2, \dots, \mathbf{p}_N)$ respectively, then the Hamiltonian H of the system is written as,

$$H(p^N, r^N) = \sum_{i=1}^N \frac{p_i^2}{2m_i} + U(r^N), \quad (0.1)$$

where H is the sum of kinetic and potential energy terms. The equations of motion of the system are given by Hamilton's equation:

$$\frac{dr_i}{dt} = \frac{\delta H}{\delta p_i}, \quad \frac{dp_i}{dt} = -\frac{\delta H}{\delta r_i}, \quad (0.2)$$

2.2.1 Basic Introduction to LAMMPS

LAMMPS stands for Large Scale Atomic/Molecular Massively Parallel Simulator. It is distributed as open-source code under the GPL terms and conditions by Sandia National Laboratories, a US Department of Energy facility. LAMMPS has the potential to be useful in a variety of material science domains. LAMMPS can be used to investigate solid-state materials such as metals and semiconductors, as well as soft materials such as biomolecules and polymers and coarse-grained or mesoscopic systems. It can be used to create atomic models at all atomic,

meso, and continuum scales, as well as to simulate particles in real time. LAMMPS can be run on a single processor or in parallel via message-passing mechanisms. Using multiple computer processor cores to reduce the computational time required to solve any problem. Individual atoms are numerically integrated using Newton's second law of motion, and their interactions are described by empirical potential fields.

$$F_i = m_i a_i \quad (0.3)$$

2.2.1.1 Modelling of the physical system

The first step to conduct a molecular dynamics simulation is to make a physical model. This physical model must hold all atoms, molecules, dihedrals, impropers etc. with their respective bond and angle if required. This entails selects a potential function that is invariant with translation and rotation. The potential function $V(r_1, \dots, r_N)$ of the nuclei locations that represents the system's potential energy when the atoms are grouped in that particular configuration.

Forces are then calculated using the gradients of the potential with respect to atomic displacements.

$$F_i = -\Delta_{r_i} V(r_1, \dots, r_N) \quad (0.4)$$

This formulation refers to the presence of a total energy conservation law $E = K + V$, where K denotes instantaneous kinetic energy. The total of pair-wise interactions is a simple way to express V is,

$$V(r_1, \dots, r_N) = \sum_i \sum_{j>i} \phi(|r_i - r_j|) \quad (0.5)$$

In the second summation, the condition $j > i$ ensures that each atom pair is only considered once. Previously, pairwise interactions were the only parameter used to construct the majority of potentials; however, this has recently changed. Furthermore, the two-body approximation performs poorly for a wide range of important systems, including metals and semiconductors. A variety of many-body potentials are used in modern condensed matter simulations to describe the best force field for the simulation.

2.2.1.2 Lennard-Jones Potential

The Lennard-Jones (LJ) potential is a simple mathematical model that approximates the interaction of two neutral atoms or molecules. John Lennard-Jones proposed a common form of this interatomic potential in 1924. The common expression for LJ potential is

$$E = 4\epsilon \left[\left(\frac{\sigma}{r} \right)^{12} - \left(\frac{\sigma}{r} \right)^6 \right] \quad (0.6)$$

at shorter distance forces is repulsive and with increasing distance forces between two molecule becomes attractive for larger r . The term $1/r^{12}$ models the repulsion between atoms when they are very close to each other. Because of the Paulie principle, when the electronic clouds surrounding the atoms overlap, the system's energy increases. The second term $1/r^6$ represents the appealing portion, which is more dominant from a distance. It is the result of the Van der Waals forces, which are weaker but dominate the nature of closed shell systems.

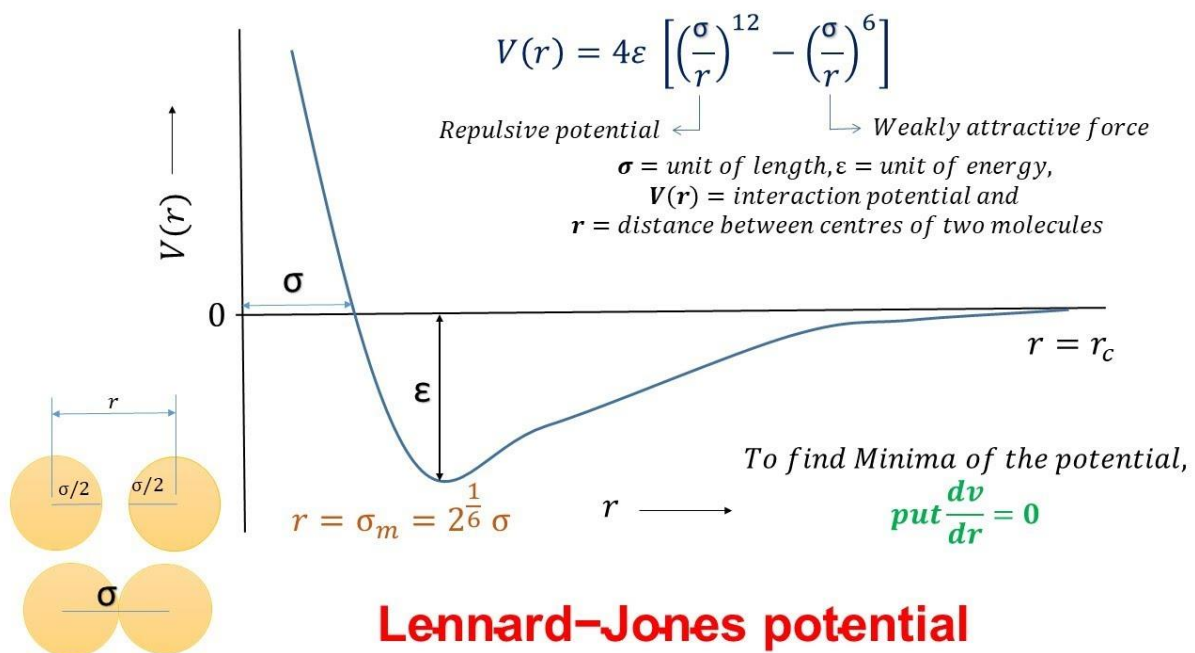


Figure 2. Interaction potential as a function of distance between two adjacent molecules in Lennard-Jones Potential.[68]

However, the LJ 12-6 potential is an important model system for studying various geometries such as solids, liquids, surfaces, clusters, and two-dimensional systems, among others. When investigating fundamental issues rather than studying specific material properties, LJ is the standard potential to use. The research done with the LJ system is assisting in understanding the fundamentals of various fields such as condensed matter physics and is still being used to explain new insights.

To isolate atoms a cut-off distance r_c is defined when applying LJ parameters to a simulation study, and this cut-off radius is used to isolate atom interactions. When the value of r exceeds this threshold, the interatomic forces become very weak and can be ignored. This saves a tremendous amount of computational power and time while having no effect on the outcome.

2.2.1.3 AIREBO Potential

The AIREBO (Adaptive Intermolecular Reactive Empirical Bond Order) potential is a versatile interatomic potential widely used in molecular dynamics simulations for studying graphene. It combines reactive and non-reactive components to accurately model the bonding behavior of carbon atoms in graphene and other carbonaceous materials.

The AIREBO potential captures the intricate carbon-carbon interactions, including bond breaking and formation, as well as bond stretching and bending. It accurately reproduces key properties of graphene, such as lattice parameters, elastic constants, and vibrational modes.

Researchers employ the AIREBO potential to investigate a range of phenomena in graphene, including mechanical properties, thermal conductivity, defect formation, and surface interactions. It provides valuable insights into the behavior and stability of graphene under different conditions, enabling the exploration of its unique properties at the atomic scale.

The AIREBO potential's capability to accurately capture the reactivity and structural characteristics of graphene makes it an essential tool for simulating and understanding the behavior of this remarkable two-dimensional material in various research areas, from nanoelectronics to nano-mechanics and beyond.

The AIREBO pair style calculates the potential energy using the original formulation of the Adaptive Intermolecular Reactive Empirical Bond Order (AIREBO) potential developed by Stuart in 2000. It is specifically designed for systems containing carbon and/or hydrogen atoms. The AIREBO potential consists of three terms:

$$E = \frac{1}{2} \sum_i \sum_{j \neq i} i \left[E_{ij}^{REBO} + E_{ij}^{LJ} + \sum_{k \neq i, j} \sum_{l \neq i, j, k} E_{kijl}^{TORSION} \right] \quad (0.7)$$

2.2.1.4 Time Integration Algorithm

The molecular dynamics simulation is powered by the time integration algorithm. It works by integrating the interacting particles' motion equations and tracking their motion trajectories. Finite difference techniques underpin this algorithm. Time is first discretized using a finite grid network, with time step Δt defined as the distance between consecutive grid points. The integration technique provides the position and some of their time derivatives at the final time $t + \Delta t$ by using known data at time t . This process can be extended by repeating the technique in accordance with the passage of time. There are different time integration techniques in MD simulation like Verlet algorithm, Leapfrog algorithm, predictor-corrector algorithms etc.

2.2.1.5 Verlet Algorithm

In molecular dynamics, the Verlet method is the most widely used time integration algorithm[69]. The basic algorithm employs third-order Taylor expansions for positions $r(t)$. There will be two equations in total, one moving forward and one moving backward in time. If v denotes velocity, a denotes acceleration, and b denotes the third derivative of $r(t)$ with respect to t , we get:

$$r(t + \Delta t) = r(t) + v(t)\Delta t + \frac{1}{2}a(t)\Delta t^2 + \frac{1}{6}b(t)\Delta t^3 + O(\Delta t^4) \quad (0.8)$$

$$r(t - \Delta t) = r(t) - v(t)\Delta t + \frac{1}{2}a(t)\Delta t^2 - \frac{1}{6}b(t)\Delta t^3 + O(\Delta t^4) \quad (0.9)$$

Adding these two equations we get,

$$r(t + \Delta t) = 2r(t) - r(t - \Delta t) + a(t)\Delta t^2 + O(\Delta t^4) \quad (0.10)$$

This is the basic form of Verlet algorithm. Since we are integrating Newtons equations $a(t)$ which is just force divided by mass and thus forces turned into a function of $r(t)$.

$$a(t) = -\left(\frac{1}{m}\right)\nabla V(r(t)) \quad (0.11)$$

This algorithm's truncation error is of order Δt^4 . Because of its simplicity, precision, and ability to create stable conditions, this algorithm is widely used in molecular dynamics simulations. This algorithm, however, has a flaw. The inability of the Verlet algorithm to generate velocities immediately cancels out the high degree of flexibility. While velocities are not required for time evolution, they are required for calculating kinetic energy K . The kinetic energy must be determined to confirm the conservation of total energy $E = K+V$. This is one of the most important checks to make to ensure that an MD simulation is functioning properly.

Computing velocity from position is possible using:

$$v(t) = \frac{r(t + \Delta t) - r(t - \Delta t)}{2\Delta t} \quad (0.12)$$

This equation is associated with error order of Δt^2 . Several method have been developed to handle velocity related issue experienced in Verlet algorithm. The Leapfrog algorithm can efficiently handle this velocity related issue rather than Verlet algorithm[2]. The speed Verlet scheme is an improved implementation of the fundamental Verlet algorithm. Location, velocities and acceleration in this method can be calculated using the following equation:

$$r(t + \Delta t) = r(t) + v(t)\Delta t + \frac{1}{2}a(t)\Delta t^2 \quad (0.13)$$

$$v(t + \frac{\Delta t}{2}) = v(t) + \frac{1}{2}a(t)\Delta t \quad (0.14)$$

$$a(t + \Delta t) = -\left(\frac{1}{m}\right)\nabla V(r(t + \Delta t)) \quad (0.15)$$

$$v(t + \Delta t) = v(t + \frac{\Delta t}{2}) + \frac{1}{2}a(t + \Delta t)\Delta t \quad (0.16)$$

2.2.1.6 Units

A set of units is available for use in LAMMPS and must be declared at the beginning of the input file. It determines the units of all quantities stated in the input script and data file, as well

as quantities output to the screen, log file, and dump file. This is the start of an input script for this purpose.

In our study we used metal units because of atom style for defining the parameters that are listed below.

- mass = grams/mole
- distance = Angstroms (\AA)
- time = ps
- energy = eV
- velocity = $\text{\AA}/\text{ps}$
- force = eV/ \AA
- torque = eV
- temperature = K
- pressure = bars
- dynamic viscosity = Poise
- charge = multiple of electron charge (1.0 is a proton)
- dipole = charge* \AA
- electric field = volts/ \AA
- density = $\text{gram}/\text{cm}^{\text{dim}}$

2.2.1.7 Simulation Box and Boundary Conditions

Before running a simulation in LAMMPS to study behavior of atom and molecule a simulation box with a specified region must be defined. Within simulation box, atoms and molecules will interact with each other. We have to define upper and lower faces of simulation box along the axis of simulation box.

The create command generates a simulation box based on the specified region. As a result, a region command must first be used to define a geometric domain. It also divides the simulation box into a regular 3D grid of rectangular bricks, one for each processor, based on the number of processors used and the settings of the processors command.

The partitioning can later be changed using the balance or fix balance commands. Boundary condition have also be defined along each axis of simulation box to run simulation.

There are two boundary condition available in LAMMPS. One is periodic another one is non-periodic.

2.2.1.7.1 Periodic Boundary Condition

Periodic boundary conditions (PBCs) are a group of boundary conditions that are frequently used to approximate a large (infinite) system using a small part known as a unit cell. Computer simulations and mathematical models frequently employ PBCs. PBC are commonly used in molecular dynamics simulation to calculate bulk gasses, liquids, crystals, or mixtures. PBC is frequently used to simulate solvated macromolecules in an explicit solvent bath. PBC are commonly used in molecular dynamics simulation to calculate bulk gasses, liquids, crystals, or mixtures. PBC is frequently used to simulate solvated macromolecules in an explicit solvent bath. The simulation box is replicated in the X, Y, and Z axes in periodic boundary conditions, as are all fictitious atoms. As a result, any atom can interact with the boundary by exiting one end of the box and reentering the other. As a result, number of atoms remain unchanged during periodic boundary condition.

2.2.1.7.2 Non-Periodic Boundary Conditions (f, s and m)

In non-periodic boundary conditions particles are restricted to interact with boundary wall as well as move from one box to another box. The possible three styles f, s, and m indicate that the box is non-periodic, which means that particles do not interact across the boundary and do not move from one side of the box to the other. The position of the face is fixed in style f. If an atom moves outside the face, it will be deleted on the next timestep of neighboring. This will almost always result in an error. For style s, the position of the face is set to encompass the atoms in that dimension no matter how far they move (shrink-wrapping). When running in parallel, the difference between the current box dimensions and the shrink-wrap box dimensions can result in lost atoms at the start of a run. This is due to the large change in (global) box dimensions causing significant changes in individual sub-domain sizes. If these changes extend beyond the communication cutoff, atoms will be lost. The third one is "m," which stands for non-periodic and shrink-wrapping boundary condition with a minimum value that is similar to the second.

2.2.1.8 Ensembles used in LAMMPS

All conceivable states combinedly form an ensemble. Different ways are available to regulate pressure and temperature. Based on the fixed state variable (energy E , enthalpy H (that is, $U+PV$), number of particles N , pressure P , stress S , temperature T , and volume V), various statistical ensembles can be generated. In LAMMPS, the commonly available ensembles are as follows:

NPT: Constant number of Particles, pressure, and temperature

NVT: Constant number density, volume, and temperature

NVE: Constant number of particles, volume, and energy.

NPH: Constant particle number, constant pressure, and constant enthalpy

2.2.1.8.1 NPT Ensemble

NPT ensemble is used for constant number of particles, constant pressure, and temperature. This ensemble can also solve non-Hamiltonian Nose-Hoover equations of motion using time integration. The unit cell vectors can be changed in this procedure, and the volume can be changed by adjusting the pressure. The Berendsen, Andersen, or Parrinello-Rahman approaches may be used to manage pressure. Temperature regulations is possible using Noose-Hoover, Andersen, and Berendsen method.

2.2.1.8.2 NVT Ensemble

This ensemble is used for particles with a fixed number, temperature, and volume. The command integrates time for non-Hamiltonian Nose-Hoover equations of motion. Its goal is to generate sampled locations and velocities from the canonical ensemble (NVT). Direct temperature scaling is used to manage the temperature during the initialization phase of this procedure. Temperature-bath coupling is also implemented during the data collection phase. Temperature-controlled MD simulation is critical for many different types of systems.

2.2.1.8.3 NVE Ensemble

In every timestep, NVE ensemble use plain time integration to update the position and velocity of the atoms in the group. This produces a system trajectory that is consistent with the microcanonical ensemble (NVE) if there are (full) periodic boundary conditions and no other

"manipulations" of the system. Thermodynamically, NVE Ensemble is isolated from its surrounding. Energy Conservation is the primary purpose of NVE ensemble.

2.2.1.8.4 NPH Ensemble

The NPH ensemble is used for constant particle number, constant pressure, and constant enthalpy (sum of U and PV). This ensemble also performs time integration using non-Hamiltonian Nose-Hoover equations of motion. This ensemble does not change temperature and this setting can be done during simulation equilibrium phase. It is possible to keep the temperature within defined limits by scaling the velocities on a regular basis.

2.2.2 Limitation of MD Simulations:

Despite its effectiveness, molecular dynamics has some drawbacks. We spend a short time focusing on the most important of them. Some limitations are discussed below.

2.2.2.1 Uses of classical forces

As molecular dynamics uses newtons 2nd law of motion to move atom that's why validity is not clear. MD simulation is primarily concerned with microscopic particle motion. As is widely acknowledged, quantum rules are more applicable to the atomic level than classical laws. The de Broglie thermal wavelength[70] is a simple test of the validity of the classical approximation.

$$\lambda = \sqrt{\frac{2\pi h^2}{Mk_B T}} \quad (0.17)$$

Where, M is the mass of an atom and T refers to the temperature. This approximation is valid under the condition $\lambda \ll a$. Where a represents the mean distance between the two closest neighbors. Taking liquids as an example, λ/a is on the order of 0.1 for light elements such as Li and Ar, and decreases further for heavier elements. The classical approximation is less useful for extremely light systems such as H₂ and Ne.

2.2.2.2 Time and Size Limitations:

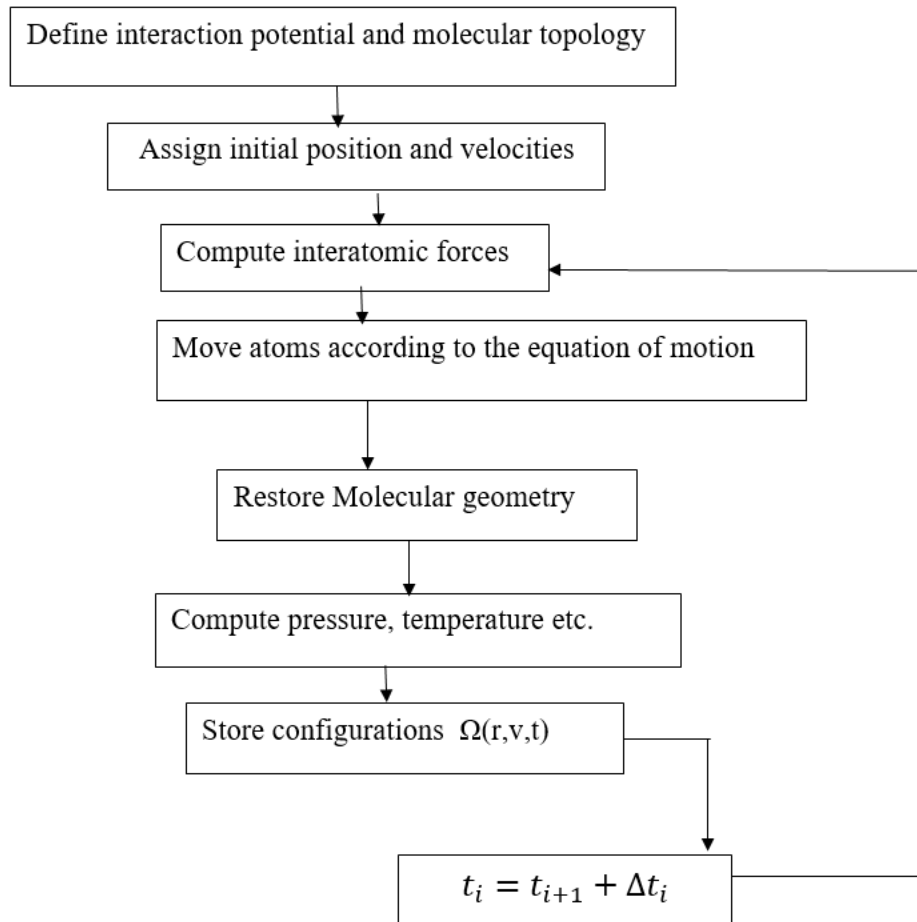
MD simulations can be performed on systems containing tens of thousands or even millions of atoms, with simulation timeframes ranging from a few picoseconds to hundreds of nanoseconds. The simulation is safe in terms of length when the simulation period is significantly longer than the relaxation time of the values, we're interested in. For getting perfect outcome every timestep Δt should be as small as possible. Relaxation time can be different depending on process and properties. System becomes sluggish and slow during phase transition. As a result, the simulation time may be less than the relaxation period of a physical feature. Another important factor to consider in MD simulation is the size of the simulation cell. We model a small portion of the system to investigate various characteristics, which limits the size of the model.

It is necessary to compare the MD cell size to the correlation lengths of the spatial correlation functions of interest. Close to phase transitions, correlation lengths may rise or even diverge. Correlation lengths cannot be accurately compared with the box dimension in these cases. Despite its potential, it may be limited due to computer efficiency.

2.2.2.3 Reality of Forces:

In the field of molecular dynamics, instantaneous forces are generated as a result of atoms interacting with one another. Atoms move because they are subject to these instantaneous forces that act on them. The relative positions and forces have altered as a result of this movement. The simulation will be more accurate if the interatomic forces are represented realistically. Because the forces are obtained as the gradient of a potential energy function, the realism will be determined by the potential's ability to reproduce the material's behavior. Only by comparing the interatomic forces to the actual values when assembled in the same manner can this be determined. Potential must be chosen in order to simulate the actual behavior of the material under the simulation's operating conditions.

2.2.3 General Procedure of Molecular Dynamics Simulations



2.2.4 System Modelling

2.2.4.1 Crumpled Graphene from 2D graphene sheet

Two-dimensional carbon allotrope known as graphene is made up of a single layer of atoms organized in a hexagonal lattice. Interplanar distance of each layer of graphene is 3.34 Å, where the C - C bond length is 0.142nm. Each carbon atom in graphene has sp^2 hybridization. It is a promising material for a variety of applications, from electronics to energy storage, thanks to its exceptional mechanical, electrical, and thermal properties. The strongest and thinnest material known to man, graphene is also one of the most conductive materials, allowing electrons to go through it more quickly than through any other substance. Due to its special characteristics, there has been a great deal of research on its possible uses, which include flexible electronics, sensors, batteries, and composite materials. The graphene sheet has a dimension of 5 nm x 5 nm.

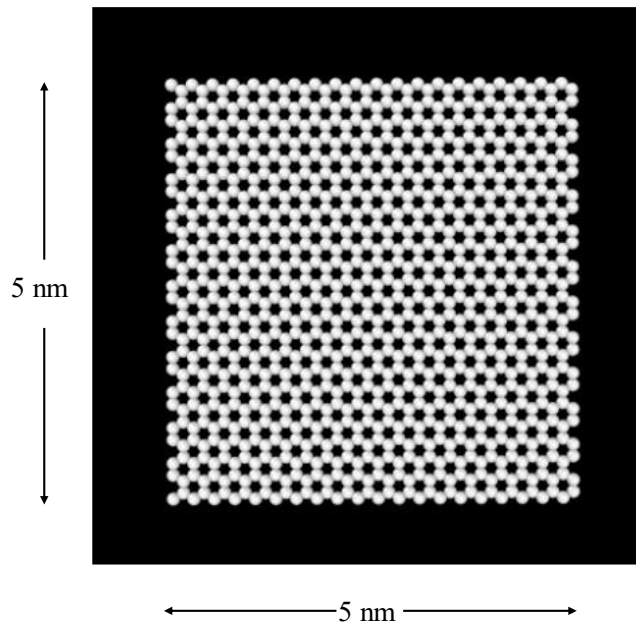


Figure 3. Hexagonal lattice of a 5nm x 5nm graphene sheet, the armchair position is placed vertically.

Crumpled graphene is a form of graphene that has been crumpled into a three-dimensional structure, similar to crumpled paper. This crumpling causes significant changes in the mechanical properties of graphene, as well as increased surface area, improved flexibility, and altered electrical conductivity. Crumpled graphene is of interest for various applications, including energy storage, sensing, and catalysis. The mechanical properties of crumpled graphene are closely related to its crumpling pattern and degree of crumpling, which can be controlled through various methods, including thermal annealing and chemical doping. By tuning these parameters, researchers can tailor the mechanical properties of crumpled graphene for specific applications.

2.2.4.2 Crumpling method of graphene

Folding graphene is different from folding a sheet of paper as graphene has a preference for folding axes due to its anisotropic nature. The crumpling of graphene can be compared to the organization of dislocations in a stressed crystal, where the energy condenses into a limited subset of accessible volume in the form of a network of ridges[71]. Using the adaptive

interatomic reactive empirical bond-order (AIREBO)-morse potential for carbon-carbon interactions, a square sheets of graphene (50Å x 50Å, 100Å x 100Å, 150Å x 150Å) is simulated atomistically[72].

It has been demonstrated that the AIREBO/morse potential accurately describes the chemical and mechanical properties of hydrocarbons, including graphene. In LAMMPS, the MD simulations were carried out. Because controlling bending energy was more important for the simulation than regulating temperature or pressure, it was carried out in an NVE ensemble. By squeezing the graphene sheets into a sphere and applying a spring-force constraint, the graphene sheets are randomly crumpled. The force's equation is provided below:

$$F(r) = -K(r - r(t))^2 \quad (0.18)$$

By invoking the "fix indent" command, a compelling force is exerted within the simulation framework. An indenter is strategically placed within the simulation box, capable of both facilitating material penetration and acting as a flow impediment by repulsing atoms upon contact. Moreover, it can be leveraged to confine the simulation within a constrained environment, effectively limiting the accessible space for atomic motion.

Crumpling steps that are followed:

- i. **Initialization:** The boundary conditions were carefully set to ensure periodicity in all three dimensions, thus avoiding any unwanted edge effects that could compromise the simulation accuracy. A graphene layer, with a lattice constant of 3.567, was constructed using carbon atoms arranged in a hexagonal pattern. To initiate the simulation, each atom was imparted with a specific initial velocity, thereby imparting an initial temperature to the system. Such meticulous attention to detail in setting up the simulation ensures that the obtained results are both reliable and reproducible.
- ii. **Equilibrium:** The simulation was optimized through the implementation of the "fix balance" command, which dynamically adjusted the size and shape of processor sub-domains to ensure an even distribution of particles and computing load across processors. Through continuous rebalancing during the simulation, optimal performance was achieved. The simulation was then run to reach a state of thermal equilibrium.
- iii. **Crumpling:** To initiate the crumpling process, a spherical indentation force was applied, followed by a gradual reduction in the effective crumpling radius at a rate of 1.25Å/step

and a timestep of 0.001 picoseconds. The reduction rate was carefully chosen to prevent atom loss due to temperature rise. Furthermore, adjustments were made to all three boundary conditions to facilitate the crumpling process. The following equation was used to calculate the radius of the crumpled graphene after each step:

$$r = r_0 - (n_c - n_e) * rate * ts \quad (0.19)$$

$$r_0 = \sqrt{x_{lo}^2 + y_{lo}^2 + z_{lo}^2} \quad (0.20)$$

iv. **Final run:** In order to obtain the necessary crumpling level, the final simulation was run with a predetermined number of steps.

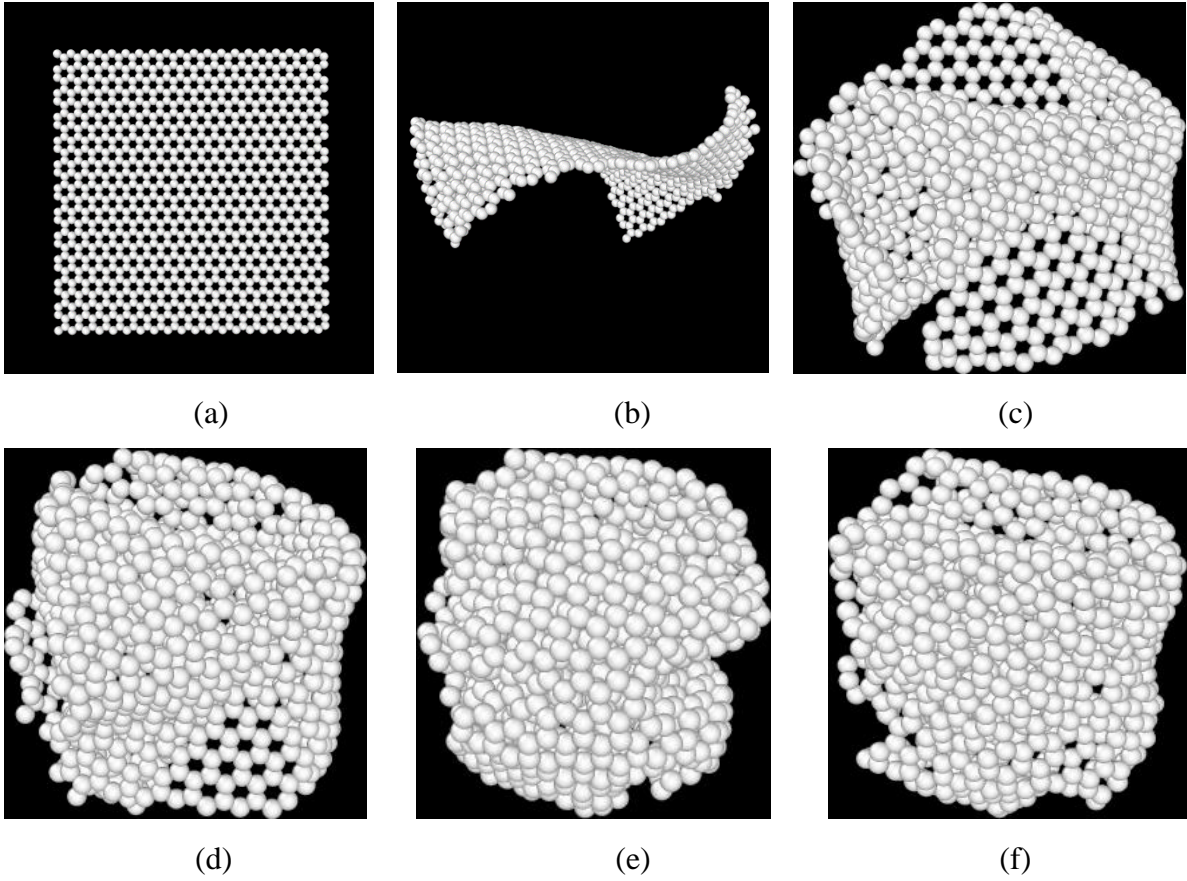


Figure 4. Crumpling a graphene sheet (50Å x 50Å) step by step.
(a) $r = \infty$ (Flat), (b) 26.5 Å, (c) 19.3 Å, (d) 14.7 Å, (e) 12.3 Å, (f) 7.6 Å.

2.2.4.3 Molecular dynamics codes and utilities

There are numerous reliable and well-known software programs that can be used for MD simulations, both in the public domain and commercially. Some of the widely used public domain programs are DL-POLY, NAMD, LAMMPS, Gromacs, TINKER, and GULP, among others. In comparison, some commercial codes include GROMOS, CHARMM, AMBER, and Forcite module in Materials Studio. Besides, several visualization software tools are available to view simulation configurations and trajectories, such as OVITO, VMD, gOpenMol, VESTA, and Rasmol. Additionally, many of these programs come equipped with built-in analysis tools to compute a wide range of properties from the MD trajectories.

In this attempt LAMMPS and OVITO has been utilized for simulation and visualization of the system.

2.2.4.4 Modelling of Porous Crumpled Graphene

Porous electrode always provides an additional benefit to the supercapacitor device's performance. Therefore, in this investigation, a variety of defects were introduced onto the previous models of graphene with different Crumpleness for analyzing the mechanical properties with defects.

The amounts of defects were 5%, 10%, 20%, 30%. Vacancies in the surface of the graphene were created by using MATLAB code. 5% porosity means 5% of the total atoms will be removed randomly which simulates the porous state of a graphene system.

Table 1. Number of atoms of graphene sheet that is crumpled per defect level.

Percentage Porosity	Number of atoms
0%	960
5%	912
10%	864
20%	768
30%	672

2.2.5 Simulation method

2.2.5.1 Simulation Parameters

The basic definition has been established using *metal* units for this simulation in the initialization steps of the input script. As was previously said, the boundary conditions are defined as *s*, *p*, and *p*. The shrink-wrapped boundary condition has only been used in the loading direction, whereas periodic boundary conditions have been employed in both directions to prevent unintended atom losses. Atomic type data have been used since they are consistent with the thesis's goals and model. The AIREBO/morse potential was used to cause the graphene sheet to crumple. According to earlier studies, the AIREBO[73] potential was used for mechanical analysis involving Vander wall forces.

Previously created *atomic* style graphene data files has been used through *read_data* command. The non-porous graphene has 960 atoms and less when it has been defected as discussed before. The pair coefficient was defined for all carbon atoms through the potential file.

2.2.5.2 Relaxation

The process of relaxation enables the atoms to modify their locations in order to reduce the system's potential energy and return the substance to its equilibrium configuration. Using techniques like energy minimization or molecular dynamics simulation, relaxation in the context of molecular simulations entails repeatedly changing the locations of the atoms until the forces acting on each one is minimized. To accurately simulate the behavior and characteristics of graphene under diverse circumstances, such as mechanical deformation, thermal expansion, or chemical interactions, relaxation of the material is required. Calculated parameters like the elastic modulus, fracture strength, or electrical conductivity may not be accurate if the graphene lattice is not sufficiently relaxed.

The system has been relaxed with NVT for 1ps until the residual stress is removed and the system reached minimum potential energy.

2.2.5.3 Tensile Loading

The parameters elastic modulus, shear modulus, yield strain and strength, ultimate strain, fracture strength, Poisson's ratio, and hardness are frequently used to quantify the properties of

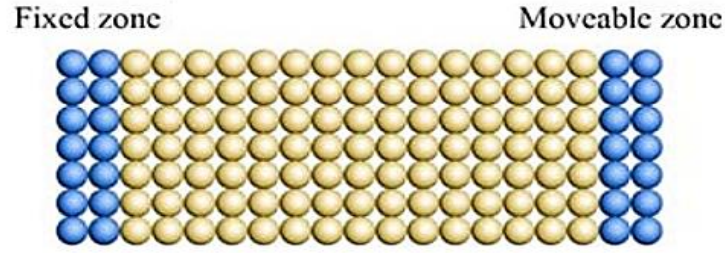


Figure 5. Diagram of an MD simulation model for displacement-controlled tensile tests. The boundary layer on the right is movable, but the boundary layer on the left is fixed (blue).

materials. These properties can be measured by experimental procedures such as tensile, shear, and indentation testing. These tests can be modeled to precisely predict the mechanical characteristics of materials in molecular dynamics simulations.

To simulate a tensile test in molecular dynamics, two common approaches are often used. The first approach involves defining two boundary layers at the outset. To apply a tensile load to the system, one of the boundary layers is held in place, while the other moves in the loading direction, as shown in Figure 3[74].

The latter determines the strain rate based on the magnitude of its velocity. This strategy is known as the displacement-control method. The movable boundary layer in an MD simulation can be displaced in two ways: dynamically or incrementally. In the dynamic approach, the layer is continuously displaced, while in the incremental approach, the layer is moved incrementally, followed by a relaxation process with the boundary layers held fixed. These approaches typically yield similar predictions for the elastic modulus and ultimate strain of metallic materials. However, the dynamic approach can overestimate the fracture strength of covalent systems due to insufficient structure relaxation during tensile loading, leading to brittle fracture instead of ductile fracture in covalent bond networks.

The second approach for modeling a tensile test in MD simulations involves expanding the simulation box at a constant rate by rescaling the coordinates of atoms along the direction of the tensile load. The coordinates of each atom are rescaled by the same factor, maintaining their fractional coordinates constant throughout the loading process. This approach is called the rescaling method and uses the equation $x_i = x_i^0 [1 + \dot{\epsilon}_x (t - t_0)]$ to scale the x-coordinates of atoms,

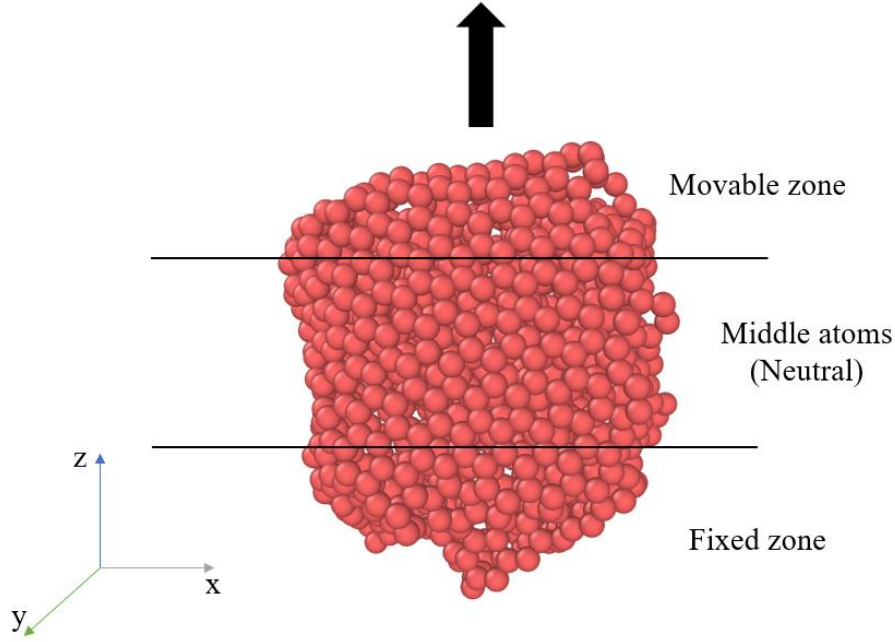


Figure 6. Application of displacement control method for uniaxial tensile loading along z axis in a non-porous crumpled graphene domain.

where x_i^0 is the initial x-coordinate of atom i , x_i is its x-coordinate at time t , and $\dot{\epsilon}_x$ is the strain rate in the direction of the tensile load.

The displacement control approach has been adopted in order to apply strain to the plain and crumpled graphene models. Because the rescaling method creates difficulty to add strain in case of the non-uniform crumpled graphene systems. Figure 4 resembles the displacement control method applied in the concerned crumpled graphene system. The strain rate applied to the modeled system in MD simulations of the tensile tests is typically in the order of $10^8 - 10^9 \text{ s}^{-1}$ [75]. Strain rate was set by applying velocity to the upper atoms at 0.001 ps^{-1} or 10^9 s^{-1} for tensile loading until fracture. The stress, strain, potential energy was computed. While the boundary (Fixed and the Movable zone) employs NVE, the middle atoms' motion is integrated using NVT ensembles.

2.2.5.4 Elastic Modulus

An essential mechanical characteristic called the elastic modulus characterizes a material's capacity to withstand deformation in the face of an applied load. Due to the distinct structural

and mechanical characteristics of graphene and crumpled graphene, the elastic modulus is particularly significant in these cases.

Due to its outstanding mechanical strength and stiffness, graphene, a two-dimensional material, holds promise for use in a variety of applications. It has one of the greatest elastic moduli of all known materials, often in the range of 0.5 - 2TPa[17], making it incredibly deformation resistant. Graphene's stress-strain curve was calculated for this study using the molecular dynamics approach (Figure), and the calculated Young's modulus using the slope of the curve was found to be about 1TPa for a non-porous plain graphene. Moreover, an overall comparison between porous and crumpled graphene has been discussed in the following chapter.

On the other hand, crumpled graphene is a three-dimensional substance with an intricate network of folds and creases. Despite having a lower elastic modulus than pure graphene, it nonetheless possesses exceptional mechanical qualities because of its unusual structure. Crumpled graphene's elastic modulus can change based on the degree of crumpling, size, and shape of the crumpled structures.

In all situations, knowledge of and ability to anticipate the mechanical behavior of these materials under various loading scenarios, such as tensile or compressive loads, depends on their elastic modulus. It is also a crucial factor in designing and enhancing graphene-based structures and gadgets for a range of uses in nanotechnology and other fields.

2.2.5.5 Strain Energy

The stress-strain curve acquired from a tensile or compressive test can be used to determine strain energy, which is a measure of the elastic potential energy stored in a material as it is deformed. It is used to compute several parameters including elastic modulus, yield strength, and ultimate strength and is essential in determining the mechanical properties of materials like toughness and resilience. Understanding the deformation and failure behavior of materials under external loads and gaining knowledge of microstructural alterations and failure causes are helpful in molecular dynamics simulations. Moreover, materials that have experienced strain, or a change in dimension, store this particular type of potential energy as strain energy[76].

By calculating the system's potential energy at various deformation levels, strain energy can be calculated in molecular dynamics (MD) simulations[77]. The system is brought into equilibrium at a reference state, and then a load or deformation is applied to produce a distorted state. The

strain energy of the system is represented by the difference in potential energy between the reference state and the deformed state. Calculating the strain energy, which may be utilized to examine mechanical characteristics and deformation and failure mechanisms of materials at the atomic level, can be done using MD analysis tools like LAMMPS, GROMACS, or CHARMM. This investigation approach has used LAMMPS to obtain the strain energy of graphene and crumpled graphene deformation from the potential energy difference of the maximum potential energy and energy at deformed state.

In this study the strain applied to the system by assigning the movable boundary with a constant velocity which was determined from the strain rate through following equation:

$$velocity = strain_rate * L_0 \quad (0.21)$$

Which shows the dependency of movable atoms velocity on the initial system length, L_0 .

2.2.5.6 Compressive Loading

To investigate the mechanical properties of a material under compressive loading, compressive tests are conducted, yielding parameters such as the compressive modulus, yield strength, and compressive strength. While ductile materials show similar mechanical properties in both tensile and compressive tests, brittle materials like ceramics behave differently in these two tests. Therefore, conducting compressive tests is crucial to fully characterize the mechanical properties of brittle materials. By either rescaling atomic coordinates to reduce the simulation box or by fixing one boundary layer and moving the other, MD simulations can simulate compressive tests in a manner comparable to tensile tests.

For compressive test, crumpled graphene with radius 7.6 Å has been implemented. Compression load along all 3 axes has been investigated. To simulate a compression system two graphene sheet has been placed below and above the crumpled graphene system as shown in Figure 5. In the single crumpled graphene model, the boundaries were configured as s (shrink-wrapped) in the loading direction and p (periodic) in the other directions. Beside this, a continuous film

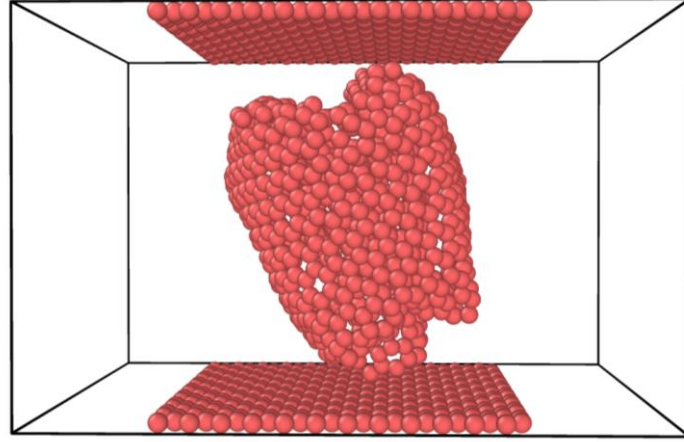


Figure 7. Arrangement for uniaxial compression testing of crumpled graphene (7.6 Å) by applying displacement control method.

structure was required in order to prevent the molecules at the borders from bulging into the open space. The periodic boundary conditions for the non-loading axes could be used to accurately represent a continuous film structure. The dimensions of the blocks were chosen to be sufficiently large to cover the distorted dimensions of the graphene molecule in the simulation as seen in Figure 5.

Number of atoms in the crumpled graphene system was 960 and in total 1728 atoms in the whole system. As it has been discussed, this simulation has also been performed under AIREBO potential environment. The potential also includes the Lennard-Jones (L-J) and torsional terms in addition to the reactive empirical bond-order (REBO) term. Moreover, AIREBO was able to explain intermolecular interactions and more precisely define single bond torsion by adding L-J and torsional terms to the original REBO potential.[72] The interatomic behavior of carbon and carbon atoms between the sheet and crumpled graphene was described using the L-J 6-12 potential as follows:

$$E = 4\varepsilon\left[\left(\frac{\sigma}{r}\right)^{12} - \left(\frac{\sigma}{r}\right)^6\right] \quad (0.22)$$

where r is the distance between two atoms during an interaction. The AIREBO potential had a cutoff distance of 3.0 scale factors (10.2). A Nosé-Hoover thermostat (NVT) was used in a canonical ensemble during the MD simulation, with a target temperature of 300 K. With an average speed of 300 K, the initial atom speeds were Gaussian-distributed. Heat was produced

throughout the compression process as a result of bond breaking and the production of carbon atoms, maintaining the system's energy in accordance with the rules of thermodynamics (NVE). The heat produced inside the control volume was transferred to a heat sink by the canonical ensemble, which still kept the temperature constant. Because graphene plates had no motion other than displacement during compression and unloading, they were removed from the ensemble and were simulated as rigid entities. To relax the system at 300 K, a relaxation simulation was conducted before the main simulation for each model. Three steps made up the simulation: relaxation, compression or loading, and unloading.

The loading and unloading steps were simulated under strain rate of 0.02 ps^{-1} . And the system was relaxed for 30ps before applying the strain.

2.2.5.7 Timesteps

For precise and reliable findings in molecular dynamics simulations for a tensile test, selecting the right timestep is important. The timestep should be large enough to avoid unnecessarily high processing costs while still being small enough to capture dynamics. The right timestep is determined by things like the size of the simulation box, the integration algorithm's timestep, and the force field being used. As too large or too little of a timestep might result in unstable or computationally expensive results, choosing the proper timestep is essential for accuracy and efficiency in the simulation.

In case of tensile testing, the timestep was kept at 0.0005ps and for compressive testing it was kept 0.0002 ps.

2.2.5.8 Temperature

Temperature is a crucial parameter in molecular dynamics simulations, as it determines the kinetic energy and dynamics of particles in a system. It is typically controlled using a thermostat and can affect the material properties and behavior of the system being studied. The simulations were performed under a controlled temperature of 300 K throughout the entire study. A constant and well-managed simulation environment was made possible by the employment of a thermostat, such as the Nosé-Hoover thermostat, which helped control the temperature and preserve the canonical ensemble.

CHAPTER 3

Results and Discussion

Mechanical properties including tensile and compressive analysis of a 50 x 50 Å graphene sheet with a range of crumpling radius and porosity has been investigated. In the tensile testing section stress-strain curve, strain energy-strain curve, elastic modulus, fracture toughness will be discussed with variation in the radius of crumpling with different grades of defects for uniaxial tensile load along y axis. The crumpling radius and defects considered are arranged in **Table 2**. Crumpleness radius and %porosity that has been considered for Tensile test.. Moreover, compressive stress-strain curve along with strain energy analysis for uniaxial loading and unloading criteria, shear stress analysis for a particular CG will be discussed in this chapter.

Table 2. Crumpleness radius and %porosity that has been considered for Tensile test.

r, Å	% defects
∞ *	0, 5, 10, 20, 30
26.5	0, 5, 10, 20, 30
24.3	0, 5, 10, 20, 30
19.3	0, 5, 10, 20, 30
14.7	0, 5, 10, 20, 30
12.3	0, 5, 10, 20, 30
7.6	0, 5, 10, 20, 30

*r = ∞ is referring to flat graphene

3.1 Graphene and CG under uniaxial tensile loading

The tensile strength of the CG is represented by the peak stress in the stress-strain curve. Uniaxial tensile loading involves applying an external force to a sample along one axis while holding the other axes stationary. It is frequently employed while researching a material's mechanical attributes, such as strength, ductility, and elasticity. Deformation has been implemented along the y-axis for each simulation under AIREBO potential for a temperature of 300 K under constant strain rate of 0.001 ps^{-1} .

3.1.1 Fracture under uniaxial tensile load on non-porous CGs

Crumpleness has an adverse effect on Graphene tensile strength. **Figure 8** shows the variation in the stress-strain relationship among the different crumpling radii of CG. With each curve on the graph denoting a distinct radius, the graph displays the relationship between stress and strain for CG at various crumpling radii. The graphene electrode's strain is probably represented by the x-axis, and the stress that results on the material is probably represented by the y-axis. These curve most illustrates how the stress changes as more strain is applied. The crucial finding is that CGs fracture toughness decreases initially with addition of crumples, i.e., the CG becomes more crumpled, up to 19.7 \AA . Interestingly, when more crumpling is added the structure shows higher resistance against fracture. This shows, up to a certain limit, crumpling the graphene can decrease its resistance to fracture but more crumpling causes higher strength. The curve for $r = 7.6 \text{ \AA}$ shows the highest fracture at around 50 GPa which is close to the value (60 GPa) estimated by Krylova et al.[78]. This gradual increase after a certain crumpleness may be the result of vander wals force between graphene layers. As increase in crumpling raises brittleness in graphene, the fracture stress decreases initially but when the graphene layers come in close contact their strength rises with crumple. Consequently, one layer compensating other layers' fracture. This curve exhibits nonlinear behavior. This is another pattern that needs to be mentioned. This is common for many materials, particularly those that may deform or sustain damage. Finally, we found that the CGs ability to resist stress decreases as crumpling radius increases. This shows that there might be an optimal point for crumpling radii where the graphene electrode's fracture toughness is maximized.

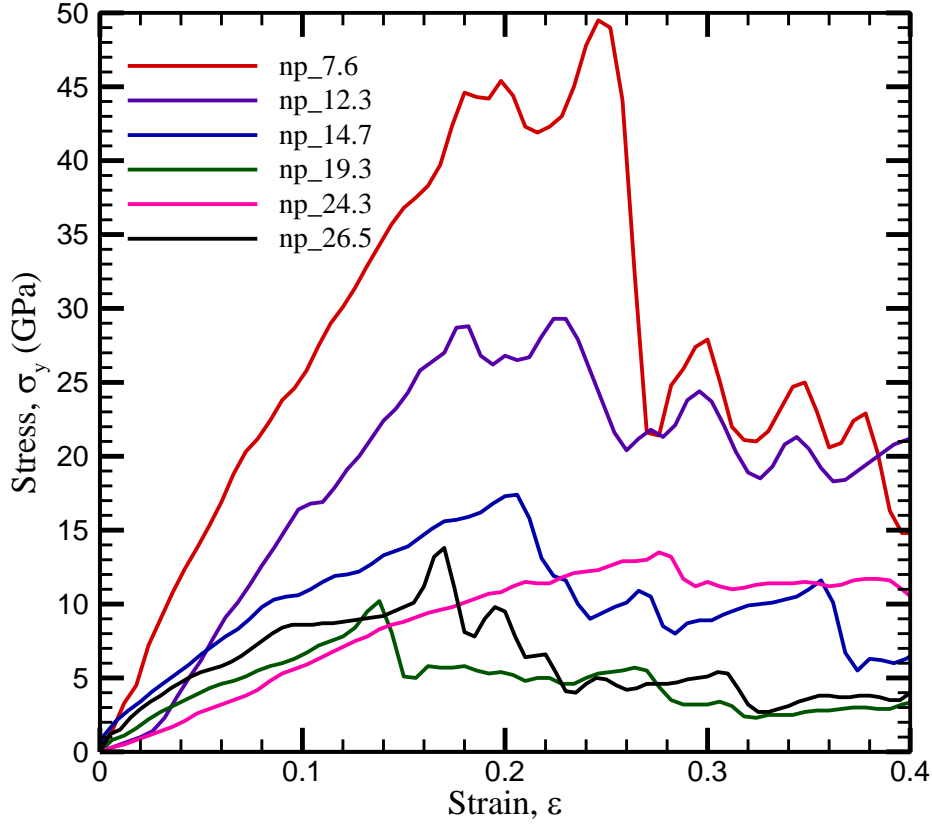


Figure 8. Variation of stress as a function of strain at different levels of crumpling in non-porous condition of graphene under uniaxial tensile loading along y axis. (Radius in Å)

Table 3. Fracture toughness at different levels of crumpling radius, where lower radius means more crumpling.

r, Å	Fracture Toughness, GPa
26.5	13.3
24.3	12.7
19.3	10.1
14.7	17.8
12.3	29.2
7.6	49.5

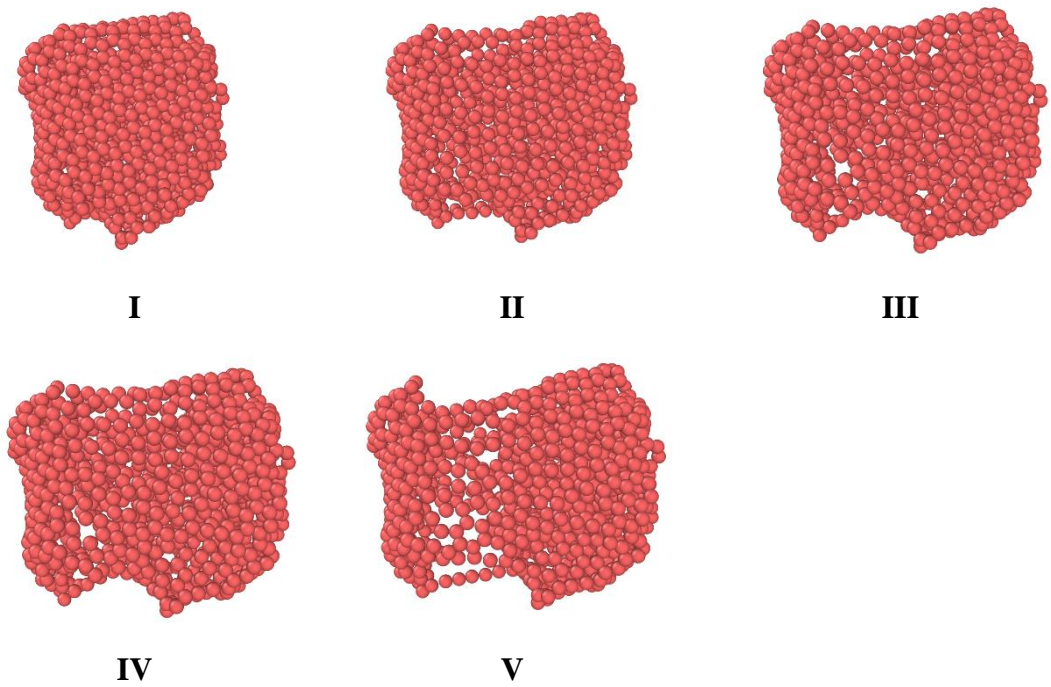
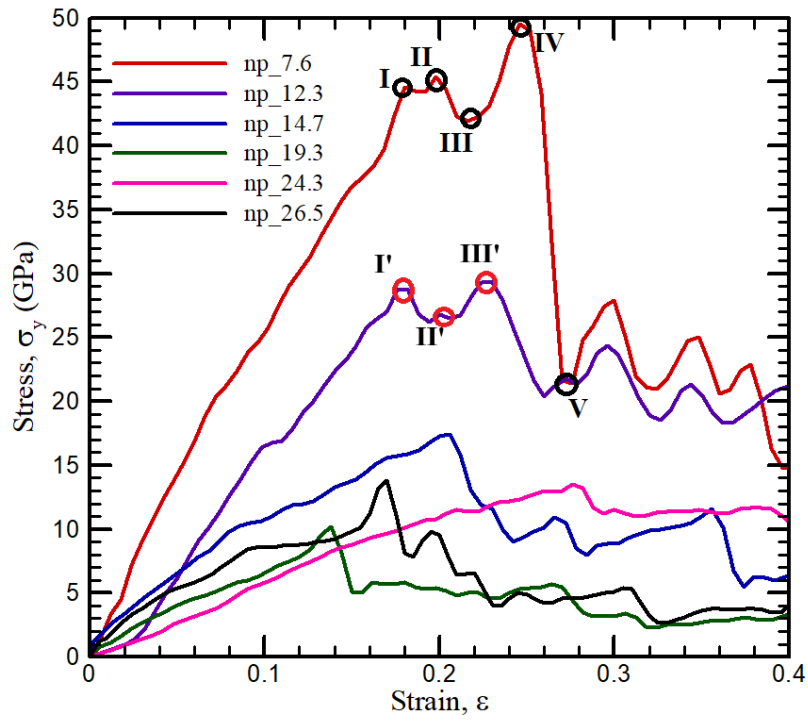


Figure 9. Gradual deformation under tensile loading for states *I* to *V* for a CG with radius of 7.6 Å, where state *IV* is the maximum fracture point.

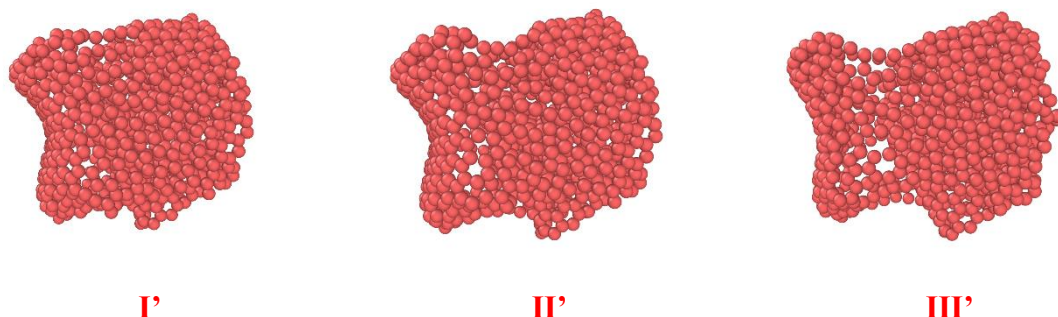


Figure 10. Gradual deformation of CG having crumpling radius 12.3 Å from initial (I') state to maximum stress state (III'), where at state III' the CG is under maximum stress.

The previous illustration in **Figure 9** is a pointed depiction of figure 6. Five points here are describing the gradual deformation of CG with radius of 7.6 Å. Point *I* is at non deformed state and gradually point *II* to *V* showing subsequent CG deformation states. At point *IV* the CG reaches its peak at 49.5 GPa and after that the stress falls down to state *V*.

Figure 10 shows the step-by-step deformation of CG with 12.3 Å radius. At state *I'* the deformation is just starting and stress is reaching the peak at around point *III'* in **Figure 9**.

3.1.2 Fracture under uniaxial tensile load along y axis on porous CGs

Porosity has an adverse effect on the mechanical properties of graphene. Porosity as well as crumple in graphene increases the effectiveness of graphene in various applications i.e., supercapacitor electrode as it increases the surface area and capacitance of CG. Optimum crumpling radius and porous combination should be found with greater mechanical performance. A through discussion on this issue is conducted in the following sections.

3.1.2.1 Flat graphene ($r = \infty$) with different randomly added defect levels

A comparison through stress strain analysis based on different porous configuration of flat graphene is encompassed in **Figure 11**.

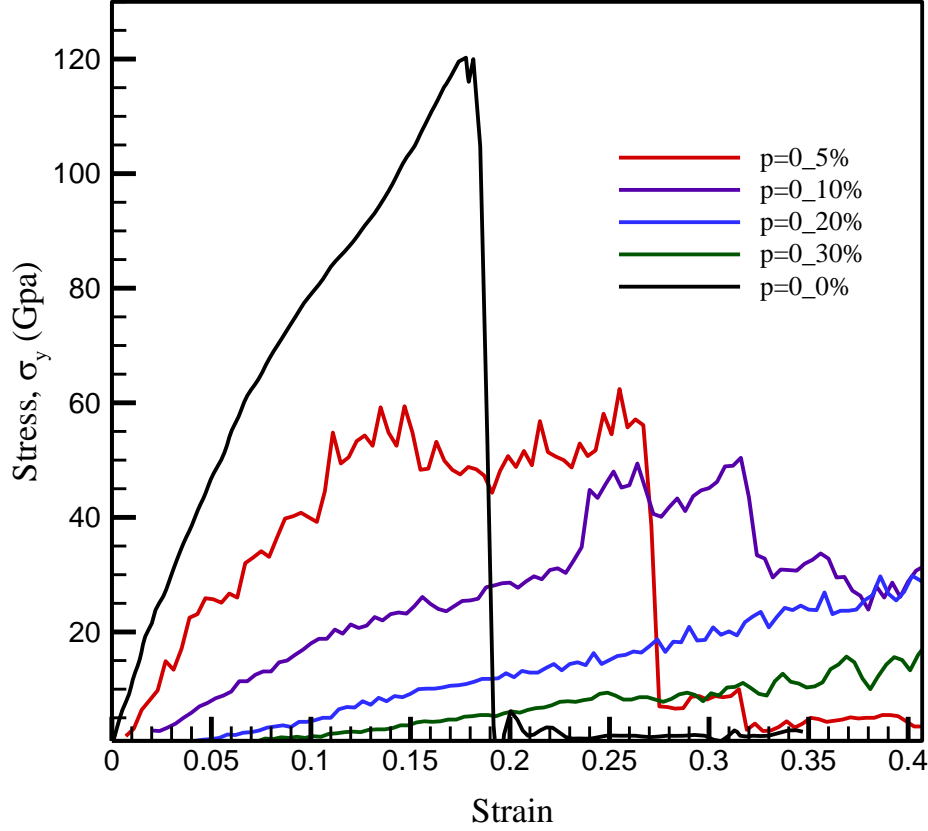


Figure 11. Variation of stress as a function of strain for flat graphene at different amount of porosity under uniaxial tensile loading along y axis.

Figure 11 most likely depicts how, at various levels of porosity, the stress on the electrode changes as the amount of strain applied to it increases. The most important findings from **Figure 11** are that the crumpled graphene loses fracture toughness as porosity increases. This shows that adding porosity can impair the crumpled graphene's resistance to fracture. Finally, it can be pointed out that the graphene's fracture toughness is almost 120 GPa at 0% porosity, but drops to 60 GPa when only 5% defect is added and gradually decreases for higher levels of porosity. **Table 4** shows the gradual change in fracture toughness in case of a flat graphene for randomly added pores.

Table 4. Fracture toughness of flat graphene with different defect levels under uniaxial tensile loading along y axis.

%Porosity	Fracture Toughness, GPa
0	120.2
5	59.8
10	50.7
20	30.2
30	20

This indicates that the mechanical characteristics of the flat graphene can be severely impacted by even minor quantities of porosity.

3.1.2.2 Fracture under uniaxial tensile load on CG at $r = 24.3 \text{ \AA}$

A comparison through stress strain analysis based on different porous configuration of CG (24.3 \AA) is encompassed in **Figure 12**

With a crumpling radius of 24.3 \AA , **Figure 12** appears to depict the relationship between stress and strain for various porosity levels for a crumpled graphene electrode. Our main finding is that as porosity rises, the maximum stress that the crumpled graphene electrode can withstand drops. The highest stress that an electrode can bear at 0% porosity is about 14 GPa, however as porosity increases, this value drops. This implies that increasing the CGs porosity can greatly decrease its ability to withstand stress, which may have implications for its use in diverse applications.

Table 5. Fracture toughness in GPa for CG with 24.3 \AA crumpling radius at different levels of porosity.

%Porosity	Fracture Toughness, GPa
0	13.7
5	11.9
10	8.8
30	6

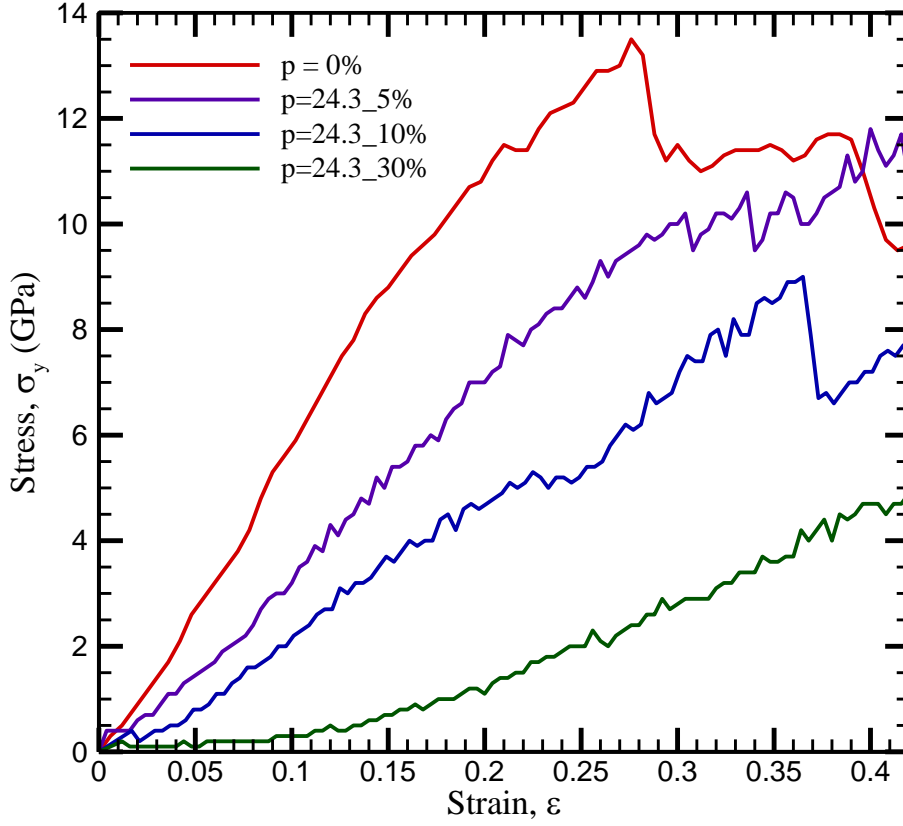


Figure 12. Variation of stress as a function of strain for CG with 24.3 Å crumpling radius at porosity of 0%, 5%, 10% and 30% under uniaxial tensile loading along y axis.

3.1.2.3 Fracture under uniaxial tensile load on CG at $r = 19.3 \text{ Å}$

A comparison through stress strain analysis based on different porous configuration of CG (19.3Å) is encompassed in **Figure 13**. For a crumpled graphene electrode with a crumpling radius of 19.3 Å at various porosity levels, **Figure 13** depicts the relationship between stress and strain. Our main finding is that as porosity rises, the maximum stress that the crumpled graphene electrode can withstand declines. The highest stress that an electrode can bear is almost 10 GPa at 0% porosity, but as porosity levels rise, this value drops until it is at a minimum of 3 GPa at 30% porosity. This means that the crumpled graphene electrode is more likely to shatter under stress as its porosity increases. Crumpled graphene electrodes may be designed and improved using this information for a variety of applications.

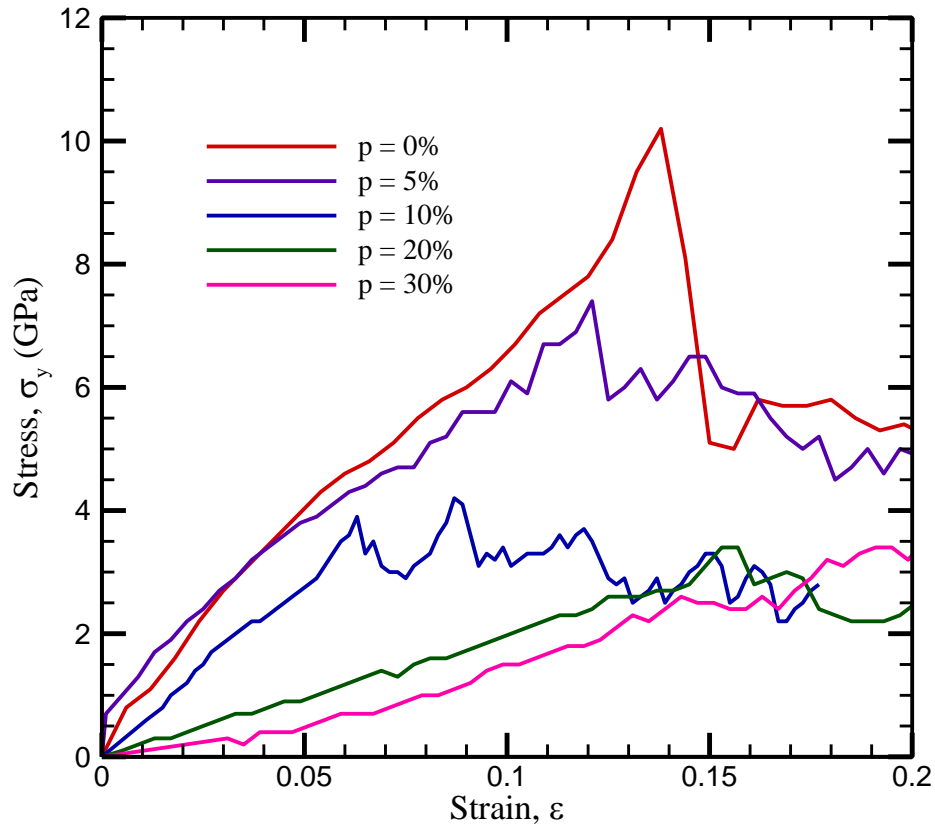


Figure 13. Variation of stress as a function of strain in case of a CG with a crumpling radius of 19.3 Å at different levels of porosity under uniaxial tensile loading along y axis.

Table 6. Fracture toughness in GPa for CG with 19.3 Å crumpling radius at different levels of porosity.

%Porosity	Fracture Toughness, GPa
0	10.5
5	6.8
10	4
20	3.5
30	3.3

3.1.2.4 Fracture under uniaxial tensile load on CG at $r = 14.7 \text{ \AA}$

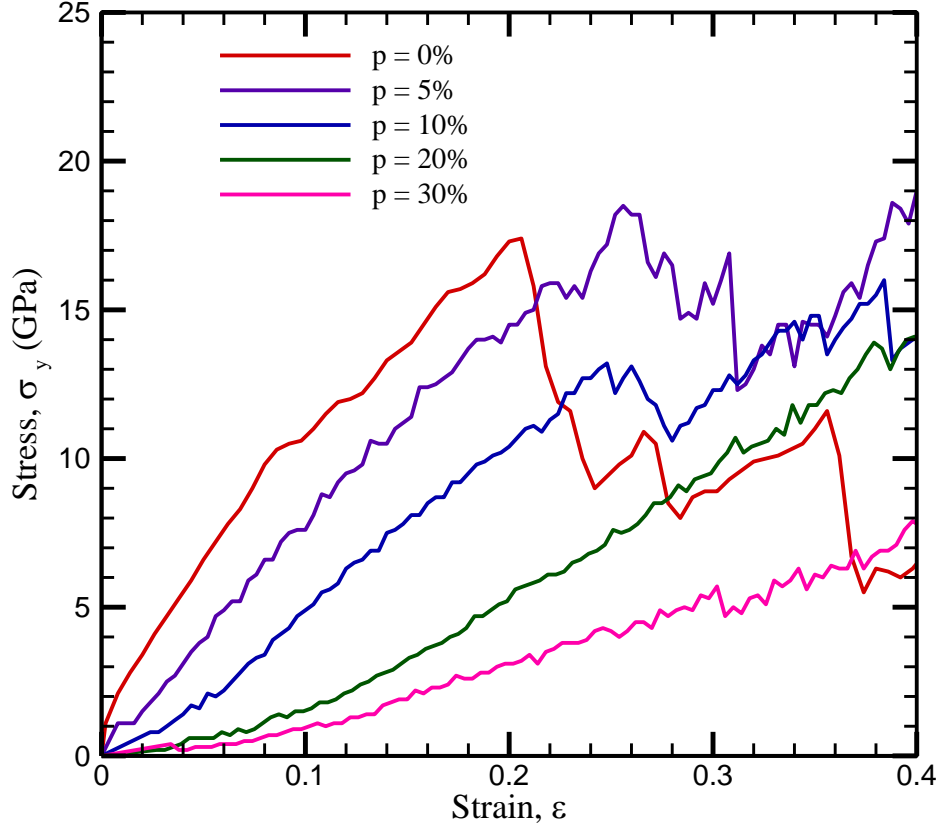


Figure 14. Variation of stress as a function of strain in case of a CG with a crumpling radius of 14.7 \AA at different levels of porosity under uniaxial tensile loading along y axis.

A comparison through stress strain analysis based on different porous configuration of CG (14.7 \AA) is encompassed in **Figure 14**. According to the data in **Figure 7**, the graph depicts the change of stress as a function of strain for a crumpled graphene electrode with a crumpling radius of 14.7 \AA at various levels of porosity (0%, 5%, 10%, 20%, and 30%). According to the findings, the CG has close fracture toughness at 5% porosity compared to a 0% porosity, showing less adverse effect of porosity than previous results.

The current results, however, differ from earlier ones obtained with a crumpling radius of 19.3 \AA , where the fracture toughness decreased with increasing porosity level. Despite this disagreement, the current results show that fracture toughness diminishes as porosity levels rise in the crumpled graphene at porosity higher than 10%, which is consistent with earlier findings. Fracture toughness for 14.7 \AA is summarized in **Table 7**.

Table 7. Fracture toughness in GPa for CG with 14.7 Å crumpling radius at different levels of porosity.

%Porosity	Fracture Toughness, GPa
0	18
5	19
10	16
20	14
30	8

3.1.2.5 Fracture under uniaxial tensile load on CG at $r = 12.3 \text{ Å}$

A comparison through stress strain analysis based on different porous configuration of CG (12.3Å) is encompassed in **Figure 15**.

For a crumpled graphene electrode with a crumpling radius of 12.3 Å at various levels of porosity (0%, 5%, 10%, 20%, and 30%), **Figure 15** illustrates the fluctuation in stress as a function of strain. According to the findings, the crumpled graphene electrode has greater fracture toughness at 0% porosity than at 5% porosity. However, in both situations, the porosity levels in the crumpled graphene electrode increased while the fracture toughness falls, which is in line with earlier results achieved with a crumpling radius of 19.3 Å. Overall, the findings imply that the crumpling radius and degree of porosity can have an impact on the fracture toughness of crumpled graphene electrodes.

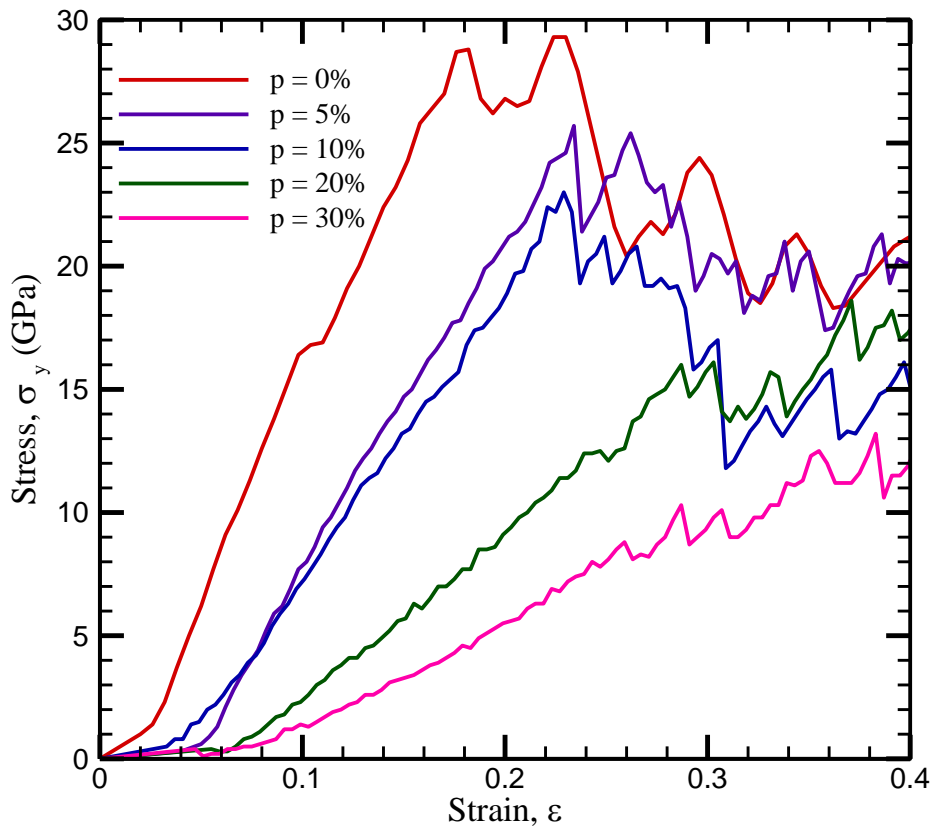


Figure 15. Variation of stress as a function of strain in case of a CG with a crumpling radius of 12.3 Å at different levels of porosity under uniaxial tensile loading along y axis.

Table 8. Fracture toughness in GPa for CG with 12.3 Å crumpling radius at different levels of porosity.

%Porosity	Fracture Toughness, GPa
0	29.5
5	26
10	23
20	18
30	13

Crumpled graphene's decreased fracture toughness with increased porosity can be linked to the material pore structure. The number and size of pores within the graphene sheets rises as porosity does as well, which might act as stress concentrators and reduce the material's mechanical strength. Therefore, the presence of holes lowers the crumpled graphene's capacity to withstand external forces and results in a reduction in fracture toughness.

The observed trend in the relationship between crumpling radius and fracture toughness is most likely caused by variations in the degree of structural disorder as well as the number, size, and location of pores inside the graphene sheets. When compared to bigger crumpling radii, a lower crumpling radius, such as 12.3\AA , can produce more structural disorder and a greater density of tiny pores, which can increase fracture toughness at 0% porosity. However, independent of crumpling radius, fracture toughness decreases as porosity rises as the size and quantity of pores take center stage.

3.1.2.6 Fracture under uniaxial tensile load on CG at $r = 7.6\text{\AA}$

A comparison through stress strain analysis based on different porous configuration of CG (7.6\AA) is encompassed in **Figure 16**.

According to the findings from **Figure 16**, crumpled graphene electrodes with a crumpling radius of 7.6\AA have a higher maximum stress withstanding capability at 0% porosity as expected, reaching around 50 GPa, than those with larger crumpling radii i.e., less crumpled. The maximum stress that results does, however, drop with increasing porosity, following a pattern identical to the preceding plots. The maximum stress at 30% porosity is about 12 GPa, which is compatible with the crumpling radius of 12.3\AA and the findings.

At 20% porosity, the fracture toughness, about 18 GPa, is nearly identical for both crumpling radii of 7.6 and 12.3\AA . The values for fracture toughness found for bigger crumpling radii, like 14.7, 19.3, and 24.3\AA , are higher than this. However, at both crumpling radii, a similar diminishing trend of resultant stress with increasing applied strain is seen at lower porosity values of 5% and 10%.

Differences in the degree of structural disorder, the size and distribution of pores, and the capacity of material to deform and recover under stress can be used to explain the mechanical behavior of CG with varied crumpling radii. The findings imply that the crumpling radius and porosity levels can be adjusted to tailor the mechanical properties of CG, which has implications for the development of graphene-based materials for varied purposes.

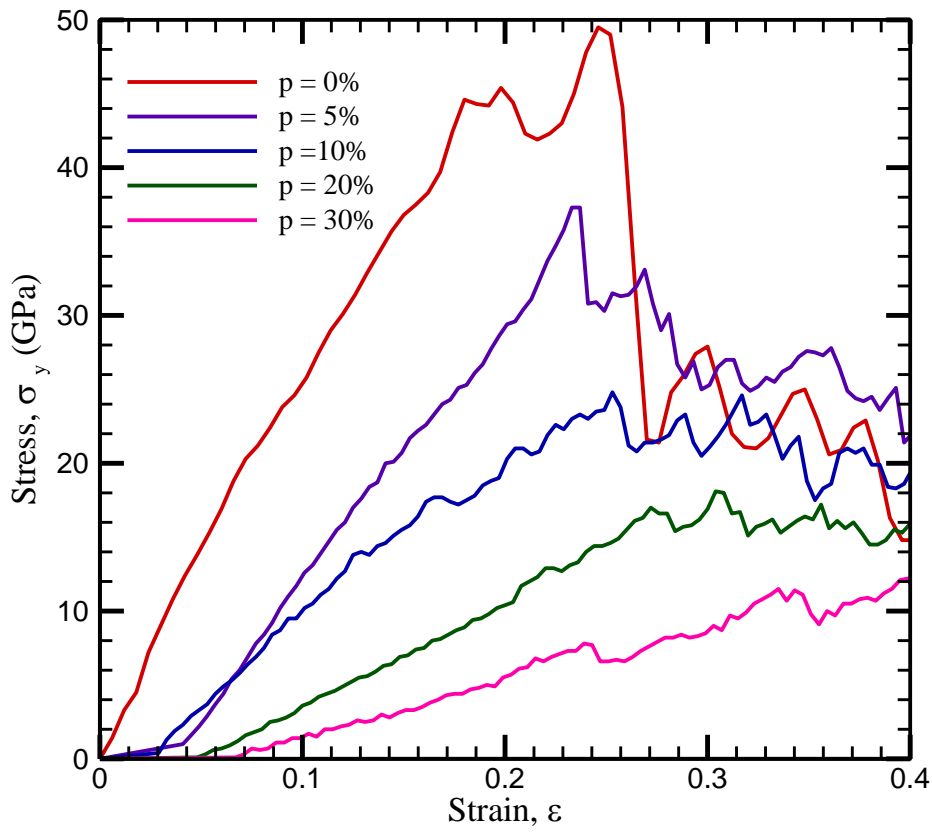


Figure 16. Variation of stress as a function of strain in case of a CG with a crumpling radius of 7.6 Å at different levels of porosity under uniaxial tensile loading along y axis.

Table 9. Fracture toughness in GPa for CG with 7.6 Å crumpling radius at different levels of porosity.

%Porosity	Fracture Toughness, GPa
0	49.5
5	37.5
10	25
20	18
30	12

Table 10. Fracture toughness in GPa for CG at different crumpling radius at 10% and 20% porosity.

r, Å	Fracture Toughness, GPa	
	10% Porosity	20% Porosity
∞	50	30
26.5	9.2	7.2
24.3	8.8	7
19.3	4	3.5
14.7	16	14
12.3	23	18
7.6	26	18

Porosity is a crucial property for different application of CG. It is clear from the above discussion that porosity has adverse impact on the tensile stress bearing capability of the material. But with smaller crumpling radius the strength increased in the end though it was low at higher radius. Previous study shows that with porosity up to 20% CG supercapacitor performance increases and then decreases gradually with higher porosity. Consequently, porosity of 10% and 20% CG should be in concern for finding the optimum CG structure.

Table 10 depicts that the fracture toughness at higher degree of CG (12.3 or 7.6 Å) are much closer at high porosity. The porosity effect is prominent at lower graded crumples

3.1.3 Comparison in light of elastic modulus under uniaxial tensile load on non-porous CGs

3.1.3.1 Effect of elastic modulus on non-porous CG with varying radius

Figure 17 illustrates the variation in elastic modulus with crumpling radius having different grades of porosity percentage. It shows how the crumpling radius and degree of crumpling of crumpled graphene influence the elastic modulus for different porosity levels. Different levels of porosity are depicted on the graph in the legends: 0%, 5%, 10%, and 30%. The graph demonstrates that when porosity levels rise, the elastic modulus decreases. At 0% porosity, the

elastic modulus is greater than at subsequent porosity levels, and it decreases significantly up to 30% porosity.

For instance, the elastic modulus is approximately 300 GPa for 0% porosity and roughly 58 GPa for 30% porosity at a crumpling radius of 7.6 Å. Furthermore, for crumpled graphene with 30% porosity, the elastic modulus did not change with crumpling radius variation at a crumpling radius of 15 Å.

The elastic modulus of crumpled graphene falls with increasing porosity because there are less carbon-carbon bonds inside the material. There are spaces and gaps in the graphene arrangement due to porosity, which lowers the material's density and reduces the number of carbon-carbon bonds that can support the material's elastic properties.

As a result, the decrease in elastic modulus can be linked to the material's density and the resulting decrease in the number of carbon-carbon bonds within the material. It is possible that the graphene structure has already lost a significant amount of carbon-carbon bonds at this level of porosity, and further reduction in crumpling radius does not result in significant additional deformations, as evidenced by the lack of change in elastic modulus for crumpled graphene with 30% porosity at a crumpling radius of 15 Å.

The elastic modulus hence stays largely constant. Regarding the lack of change in elastic modulus for crumpled graphene with 30% porosity at a crumpling radius of 15 Å, it is conceivable that at this degree of porosity, the graphene structure has already lost a sizable amount of carbon-carbon bonds, and further reduction in crumpling radius does not result in sizable additional deformations.

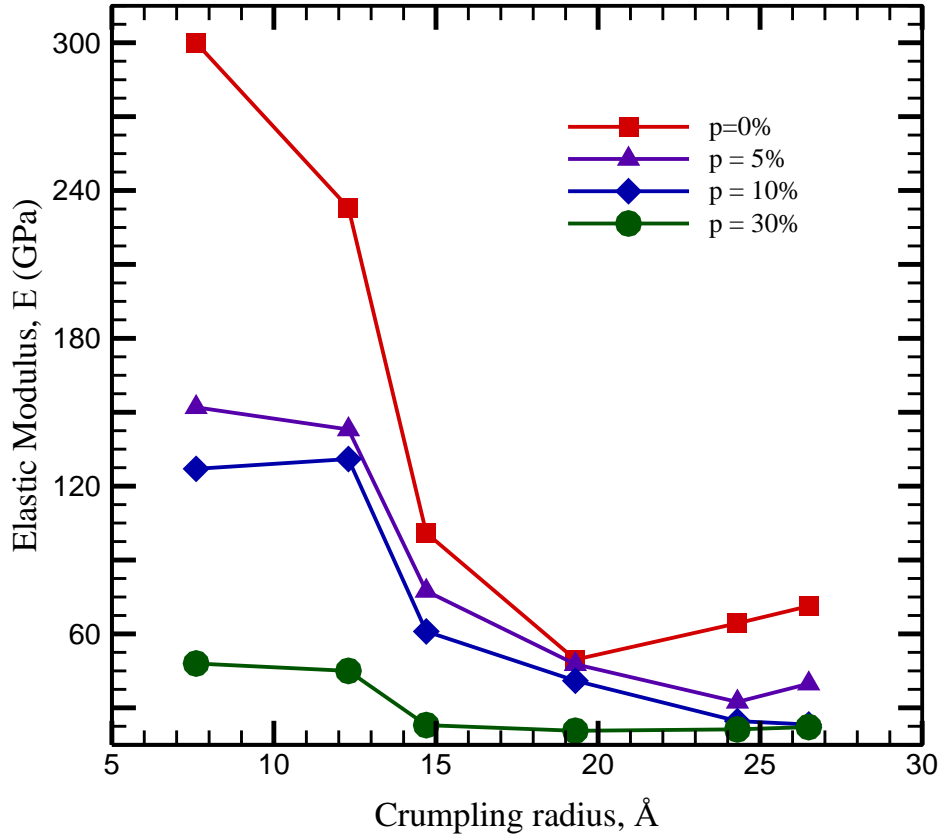


Figure 17. Variation in Elastic Modulus (GPa) with a change in crumpling radius (Å) for different grades (%) of porosity under uniaxial tensile loading along y axis.

3.1.3.2 Effect of elastic modulus on non-porous CG with varying porosity

Figure 18 illustrates the variation in elastic modulus with porosity having different grades of radius. **Figure 18** depicts the fluctuation of a CGs elastic modulus as a function of the percentage of pores put into the material for various degrees of crumpling, including flat graphene. The x-axis represents the fraction of implanted pores, while the y-axis represents the elastic modulus. The graph shows that the elastic modulus drops as the proportion of pores inserted rises, regardless of crumpling degree. The elastic modulus is larger at 0% porosity than at all levels of porosity, and it declines significantly as the fraction of pores introduced grows up to 30%.

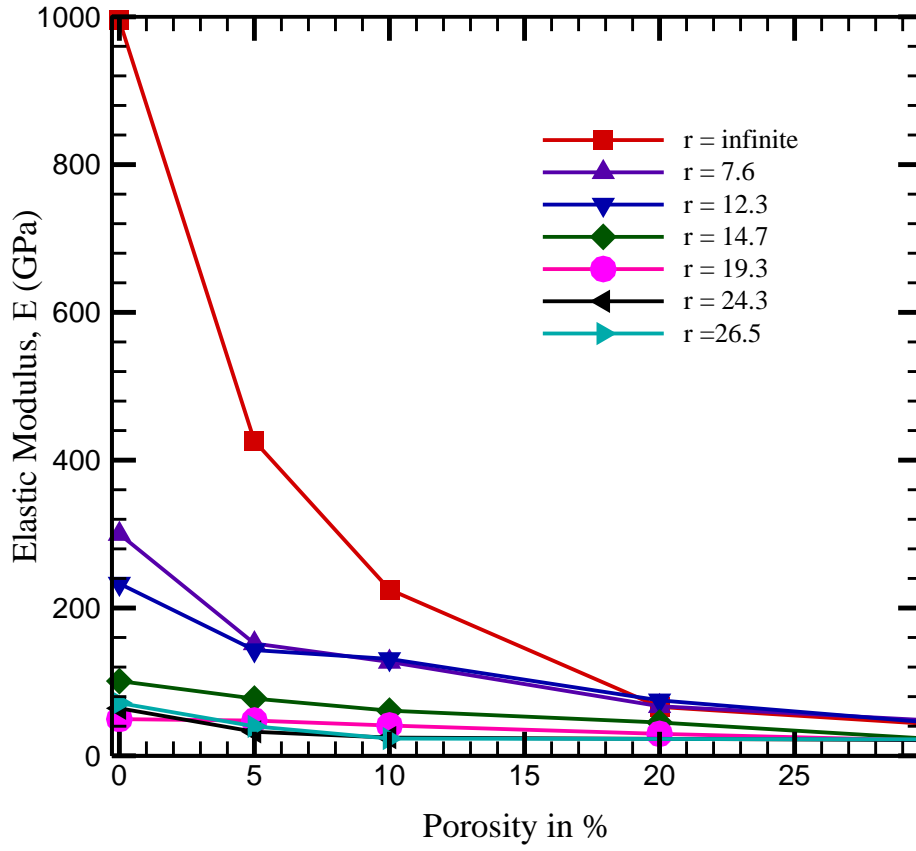


Figure 18. Variation of elastic modulus with % of porosity in electrode at different degree of crumpling under uniaxial tensile loading along y axis.

For higher crumpling radii, the difference in elastic modulus between different levels of porosity is less significant. This is due to the fact that the crumpling of the graphene structure introduces extra bonding between the carbon atoms, which partially offsets the influence of the pores on the elastic modulus. In contrast, the variation in elastic modulus between different levels of porosity for a flat electrode with smaller crumpling radius is clearly substantial.

In summary, the graph shows that the percentage of pores incorporated into the graphene has an enormous impact on the elastic modulus, with more porosity resulting in lower elastic modulus. Porosity has a fewer significant effect on elastic modulus at greater crumpling radii,

and the difference in elastic modulus between different degrees of porosity is most obvious in flat electrodes with lower crumpling radius.

The reduction in the number of effective carbon-carbon bonds in the material can explain the drop in elastic modulus with increased porosity in the CG structure. Pores in the CG structure cause holes, gaps and absence of atoms, lowering the density of the material and, as a result, fewer carbon-carbon bonds are available to sustain the material's elastic properties. As a result, the drop in elastic modulus can be linked to the material's density and, as a result, the number of effective carbon-carbon bonds within the material.

However, with smaller crumpling radii i.e., more crumpled graphene, the effect of porosity on the elastic modulus is less important. This is due to the fact that crumpling of the graphene structure causes extra bonding between the carbon atoms, which partially offsets the influence of the pores on the elastic modulus. Because of the increased bonding between the carbon atoms, the material is less vulnerable to the effect of porosity on the elastic modulus. As a result, the curve for $r = 7.6 \text{ \AA}$ and 12.3 \AA are almost similar. For a clearer understanding separate curves have been illustrated in **Figure 19 (a), (b) and (c)** for the flat as well as crumpling radius of interest.

Conversely, the variation in elastic modulus between different levels of porosity for a flat electrode with less crumpling radius is clearly substantial since the material structure is relatively simple and there are less carbon-carbon connections between neighboring atoms. As a result, the addition of pores to the structure has a bigger impact on the total density and number of effective carbon-carbon bonds, resulting in a more dramatic fall in elastic modulus as porosity increases. As a result, the curve for $r = 7.6 \text{ \AA}$ and 12.3 \AA are almost similar. For a clearer understanding separate curves have been illustrated in **Figure 19** for the flat as well as crumpling radius of interest.

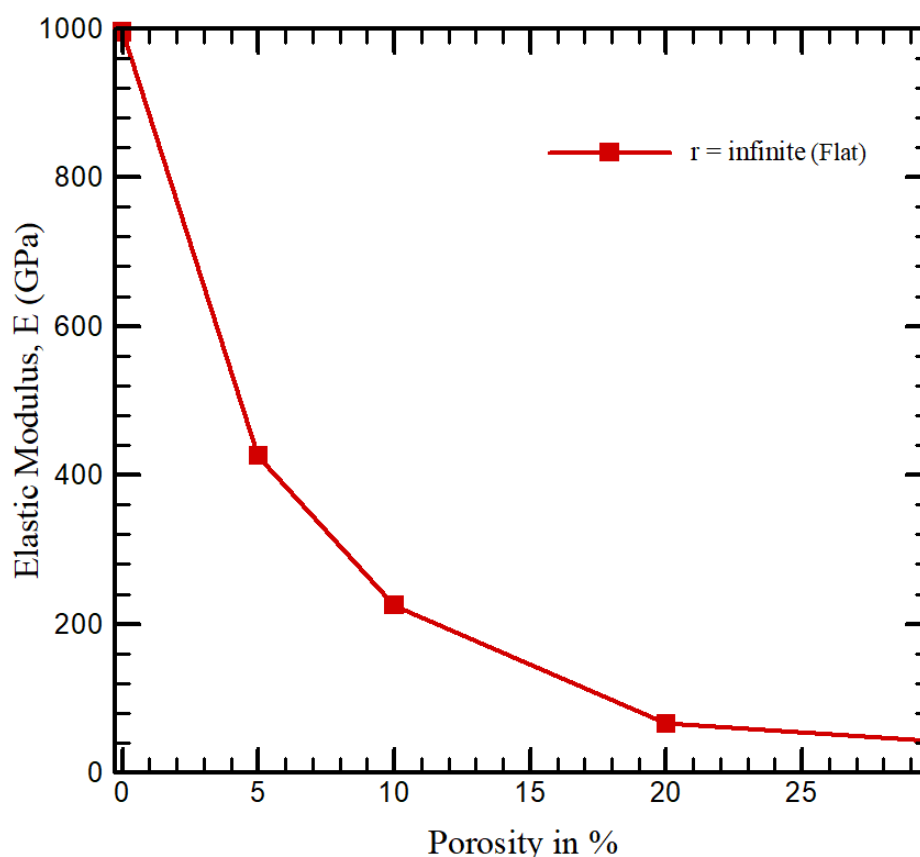


Figure 19. (a) Variation in elastic modulus as a function of % porosity for a flat graphene sheet under uniaxial tensile loading along y axis.

The resulting Young's modulus values can be compared with data found in the literature. However, there is a range in the given values since structural morphological features and the process of fabrication can both have a significant impact. For instance, relatively low carbon structures for Young's modulus and tensile strengths (5.4 - 7.7 GPa and 100 - 140 MPa, respectively) were found by Xu and Gao [79]. This experiment focuses on creating graphene fibers with both lamellar and helical structural features out of crushed graphene flakes. The scientists discovered that a closer stacking of graphene flakes, which produced shorter interlayer gaps, increased Young's modulus.

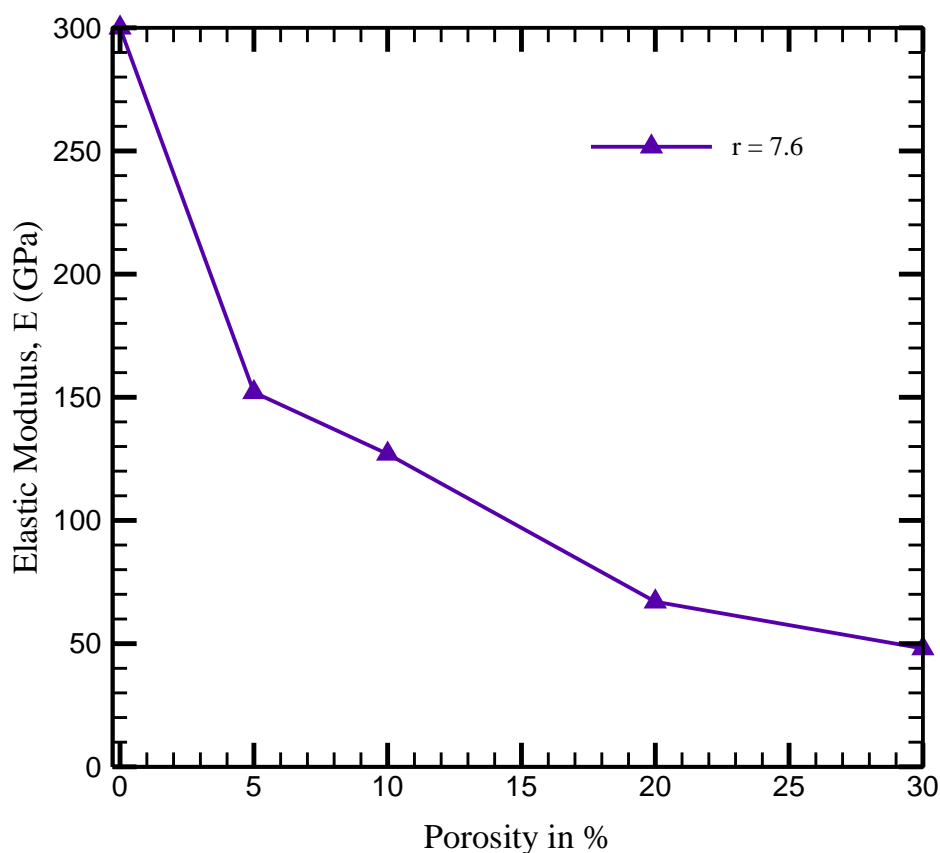


Figure 19. (b) Change in elastic modulus with % porosity for a CG with radius 7.6 Å under uniaxial tensile loading along y axis.

However, they also mentioned that by streamlining the production process, the strength of the manufactured fiber might be increased. Overall, this study emphasizes the major influence of the fabrication process on the characteristics of graphene fibers and offers insights into issues that should be taken into account during fabrication. Xu and Sen et al.[80] worked on stronger graphene fibers possessing a 500 MPa tensile strength and an 11.2 GPa modulus. Graphene fiber with a distinct microstructure and a 135 GPa modulus and 1.08 GPa tensile strength were produced by Xin et al.[81] Here, the authors demonstrated that numerous fantastic features, such as high heat conductivity and strength, are produced by a particular microstructure made up of large- and small-sized graphene sheets.

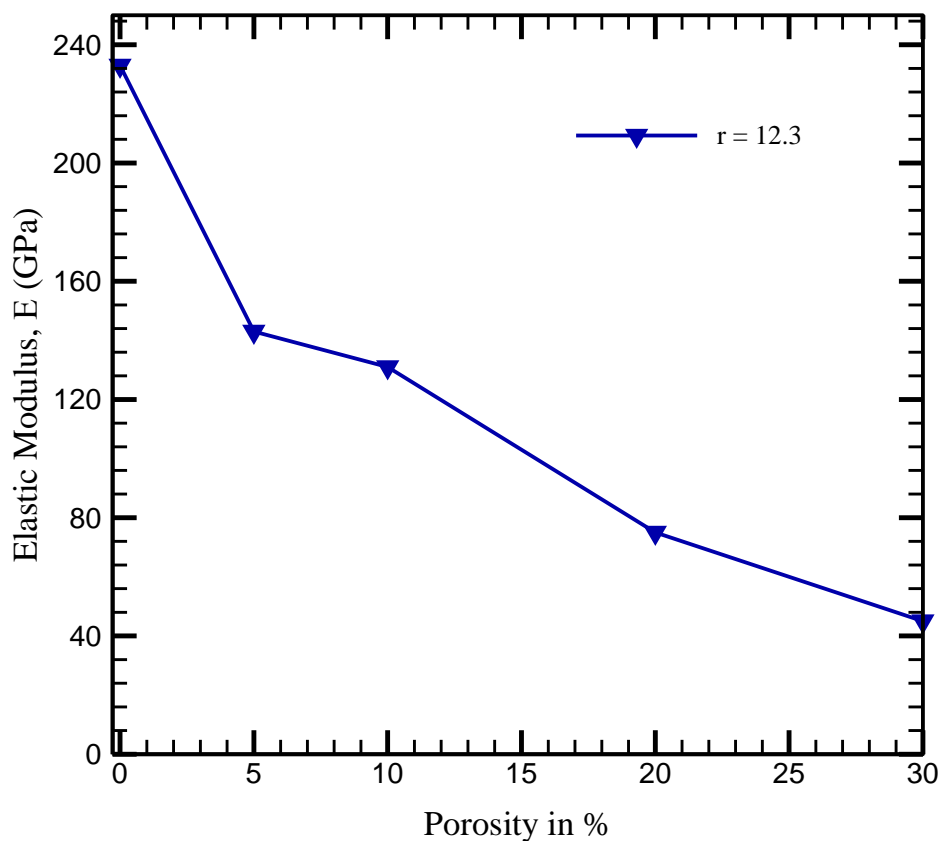


Figure 19. (c) Variation of elastic modulus with % of porosity in crumpled graphene with $r = 12.3$ Å under uniaxial tensile loading along y axis.

Molecular dynamics (MD) simulations were used in the study by Zhong et al.[6] to look at the mechanical characteristics of graphene fibers. According to the simulations, the graphene fibers' Young's modulus varied from 74 to 285 GPa while their tensile strength varied from 2.1 to 14.0 GPa. The fibers' axial direction was aligned with topological flaws in rippled graphene sheets, which made up the fibers. The findings showed that the modulus and strength of the simulated fibers significantly decreased as isotropy, or structure continuity, was reduced. The

fibers' distinct microstructures, including the number, size, and arrangement of structural features, had an impact on how they behaved mechanically.

It is important to note that the Young's modulus values were influenced by the fact that the simulated fibers had less flaws than the experimental samples. The greater strain rates used in the simulations compared to the experimental settings may also be responsible for the elevated tensile strength seen in those results. The significance of structural variables in determining the mechanical capabilities of graphene fibers is highlighted by this comparison. Furthermore, for analyzing the relation between the shape of the CG structure and its strength as well as elastic modulus uniaxial strain was added for the optimum crumpled radius 7.6 Å, which is shown in **Figure 20**.

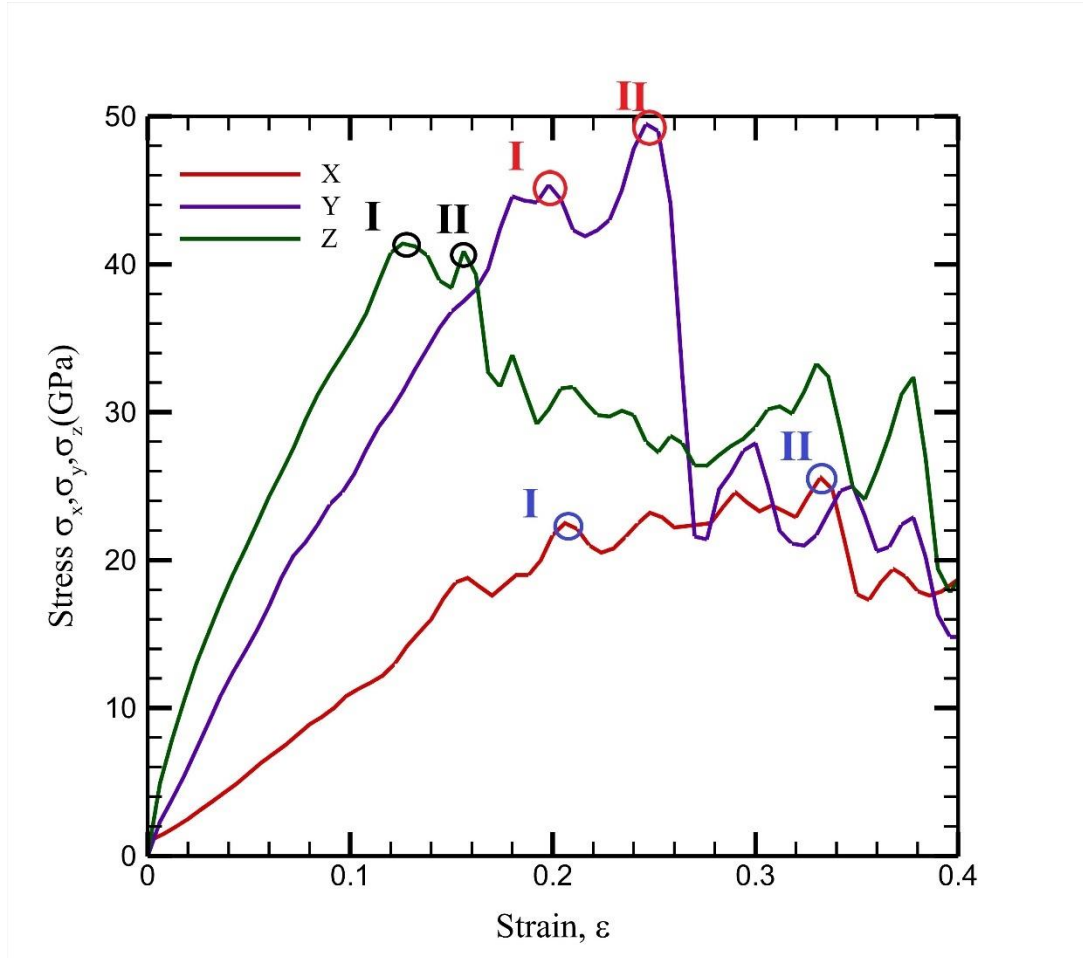
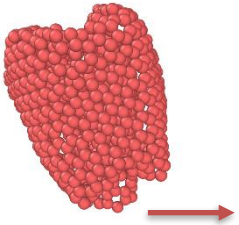
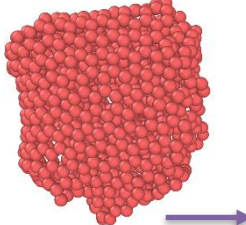
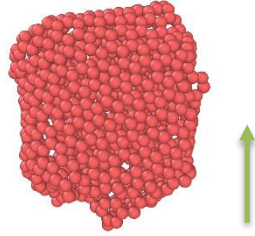
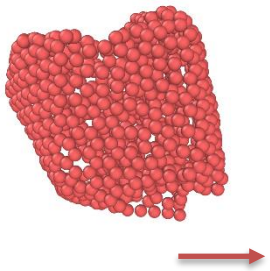
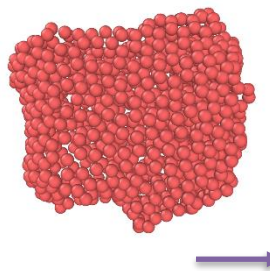
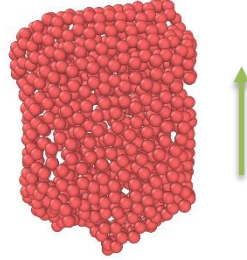
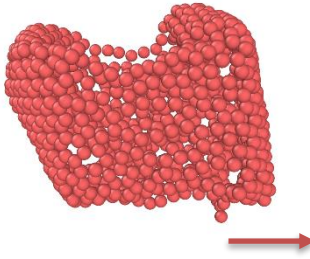
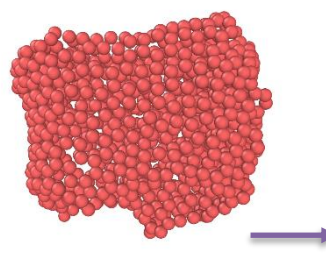
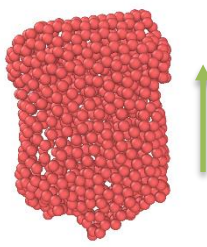
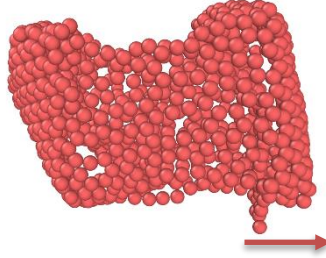
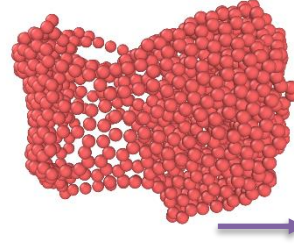
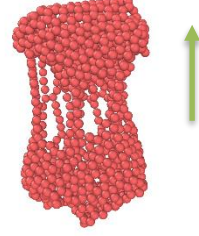


Figure 20. Variation of stress with strain for 7.6 Å CG for uniaxial tension added towards x, y and z directions under uniaxial tensile loading along y axis.

Upon examining the initial configuration presented in **Table 11**, it becomes evident that the CG structures perpendicular to the y and z axes exhibit a more organized arrangement compared to those in the x direction. Along the y and z directions, both the fracture toughness and elastic modulus are significantly higher. However, in the x direction, both the strength and modulus exhibit lower values. Remarkably, the strength and elastic modulus along the y and z axes are nearly identical. One possible explanation for this phenomenon could be attributed to the shape symmetry of the CG structures at this particular radius.

Table 11. Graphene states under uniaxial tensions along x, y, z direction.

State	X	Y	Z
Initial			
I			
	$\sigma_x : 21.7 \text{ GPa}, E = 117 \text{ GPa}$	$\sigma_y : 45 \text{ GPa}, E = 240 \text{ GPa}$	$\sigma_z : 42 \text{ GPa}, E = 285 \text{ GPa}$
II			
	$\sigma_x : 25 \text{ GPa}$	$\sigma_y : 49.5 \text{ GPa}$	$\sigma_z : 40 \text{ GPa}$
Fracture			

3.1.4 Strain Energy analysis under tensile deformation

3.1.4.1 Strain energy in non-porous crumpled graphene

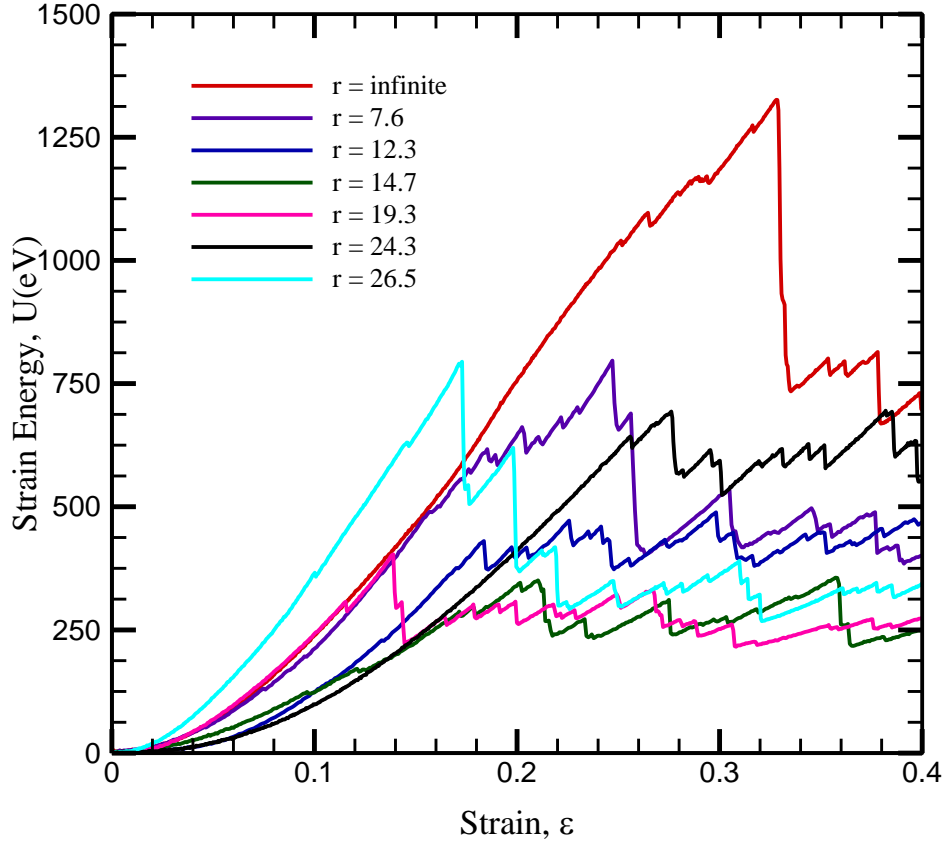


Figure 21. Variation of strain energy in non-porous crumpled graphene with applied strain at different degree of crumpling under uniaxial tensile loading along y axis.

Figure 22 depicts that the strain energy of the graphene electrode is greater when it is flat as opposed to crumpled. Furthermore, the strain energy of crumpled graphene electrodes increases with increasing applied strain, and this trend is observed until the fracture toughness is reached. The graph also shows that at varying crumpling radii, the strain energy increases with applied strain before the fracture point is achieved.

The graph shows that when the graphene electrode is flat, the strain energy is greater than when it is crumpled. However, before the fracture toughness is attained in the situation of crumpled graphene, the strain energy increases with increasing applied strain. The graph illustrates that at

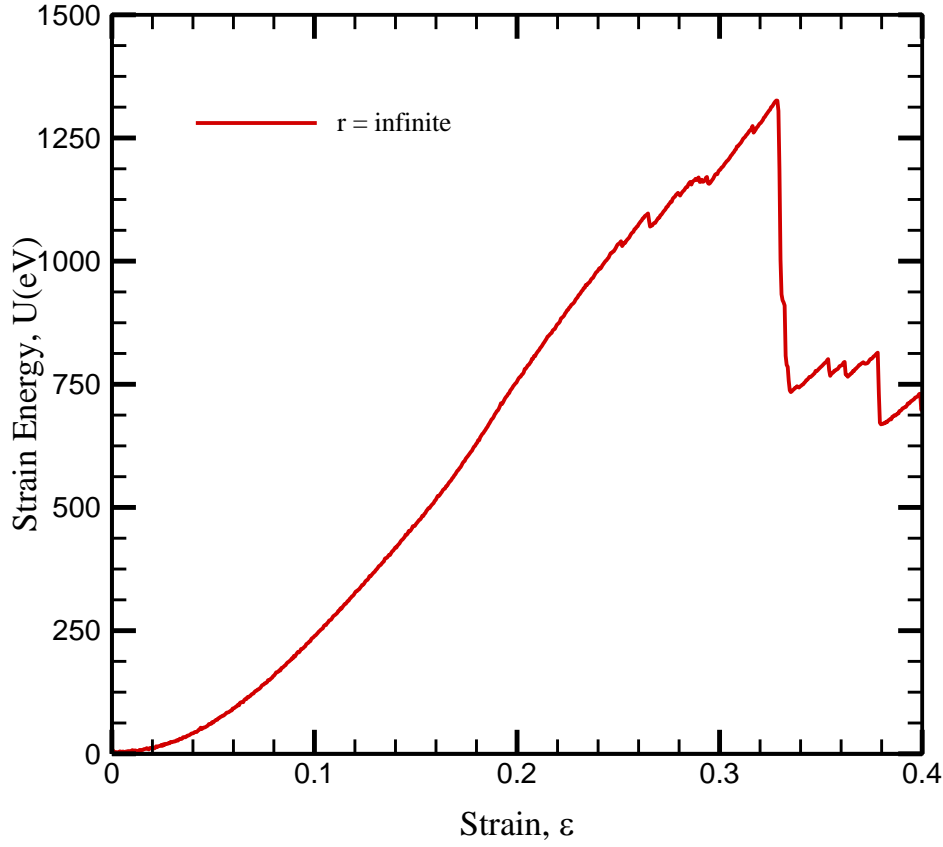


Figure 22. (a) Variation of strain energy in non-porous crumpled graphene with applied strain for flat graphene under uniaxial tensile loading along y axis.

crumpling radiuses of 7.6, 12.3, and 14.7 Å, the strain energy increases with applied strain before the fracture point is achieved. Strain energy for flat graphene is roughly 1350 eV, which decreases to around 350 eV when crumpling radius is 14.7 Å. Furthermore, the graph shows that as the crumpling radius increases, such as at 19.3, 24.3, and 26.5, the strain energy increases with applied strain until the fracture point is reached. This strain energy increases up to 750 eV if further increased in crumpling radius at 26.5 Å.

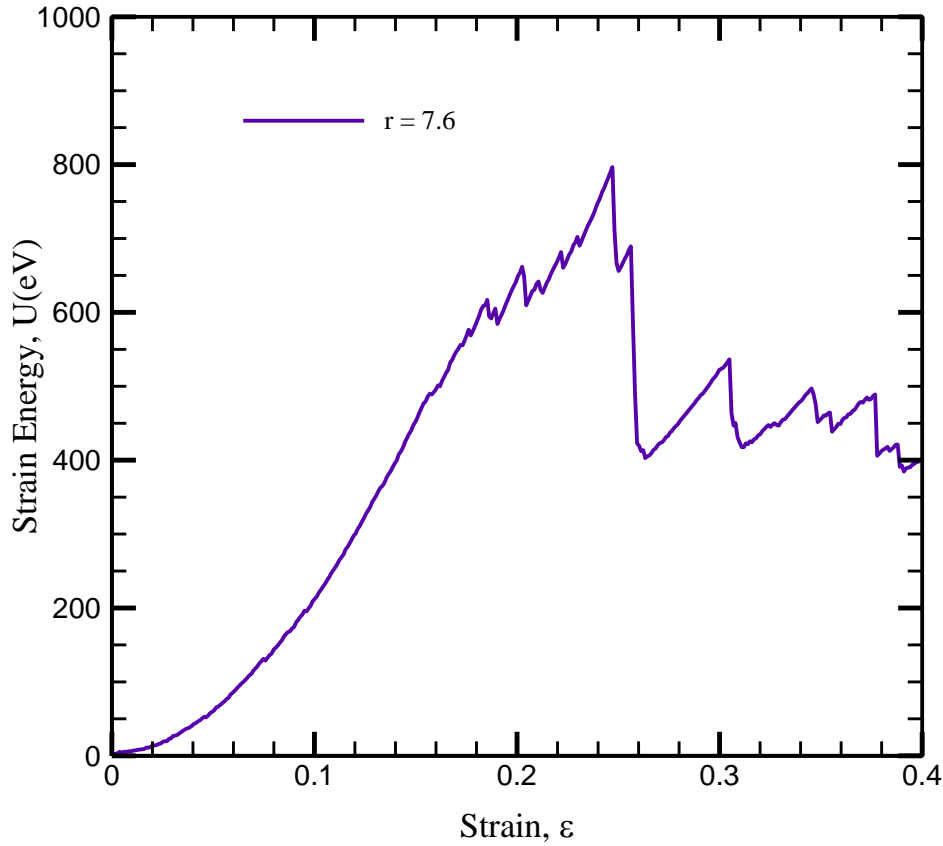


Figure 23. (b) Variation of strain energy in non-porous crumpled graphene with applied strain at $r = 7.6 \text{ \AA}$ under uniaxial tensile loading along y axis.

The increase in strain energy with applied strain for crumpled graphene can be attributed to the graphene material's peculiar crumpled structure. When an external force is applied to crumpled graphene, the crumpled portions of the graphene deform first, causing the crumpled structure to rearrange. This rearrangement allows graphene to absorb the supplied strain energy, resulting in an increase in the material's total strain energy.

Furthermore, the influence of crumpling radius on graphene deformation behavior can explain the pattern of strain energy increasing with applied strain at different crumpling radii. The graphene is stiffer and takes more applied strain energy to reach the fracture point when the crumpling radius is small. Crumpled graphene becomes more compliant and requires less

applied strain energy to reach the fracture point as the crumpling radius grows. This causes an increase in strain energy with increasing crumpling radius until the fracture point is reached.

3.1.4.2 Variation in strain energy in porous crumpled graphene

3.1.4.2.1 Variation in strain energy in porous Flat graphene

The influence of porosity on the deformation behavior of the graphene material can explain the trend of decreasing strain energy with increasing porosity in flat graphene shown in **Figure 24**. The influence of porosity on the deformation behavior of the graphene material can explain the trend of decreasing strain energy with increasing porosity in flat graphene shown in **Figure 21**. When a force is applied to the flat graphene electrode, the material deforms, allowing strain energy to be stored. The existence of pores, on the other hand, weakens the general structure of the material and diminishes its ability to store strain energy, resulting in a drop in the material's

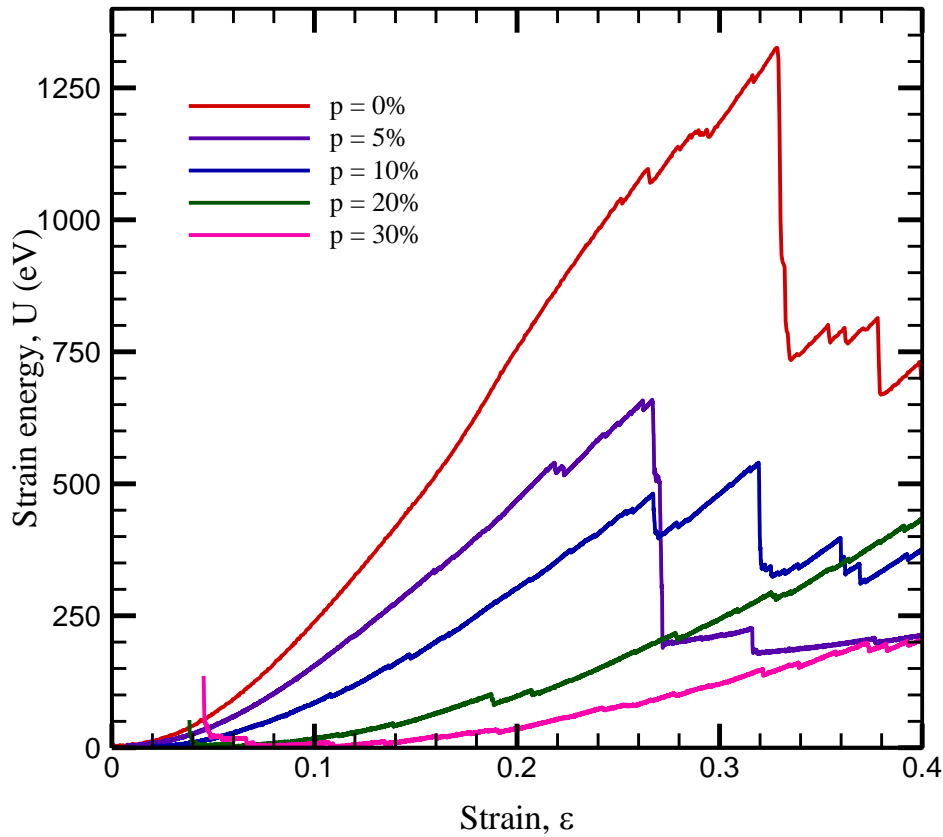


Figure 24. Variation of strain energy in Flat graphene with applied strain at different degree of porosity under uniaxial tensile load along y axis.

total strain energy. As previously stated, the presence of pores in graphene degrades its overall structure and decreases its ability to store strain energy. The pores operate as stress concentrators, causing the material to fail more easily under applied stresses and reducing the overall strain energy that the material can store.

Furthermore, the presence of pores in graphene can cause flaws in its crystal structure, further weakening its mechanical capabilities. Defects can act as crack initiation and propagation sites, lowering the material's resistance to deformation and increasing the risk of fracture.

3.1.4.2.2 Variation in strain energy in porous CG at radius 19.3 Å

Figure 25 depicts the fluctuation of strain energy with applied strain for crumpled graphene electrodes with varying degrees of porosity.

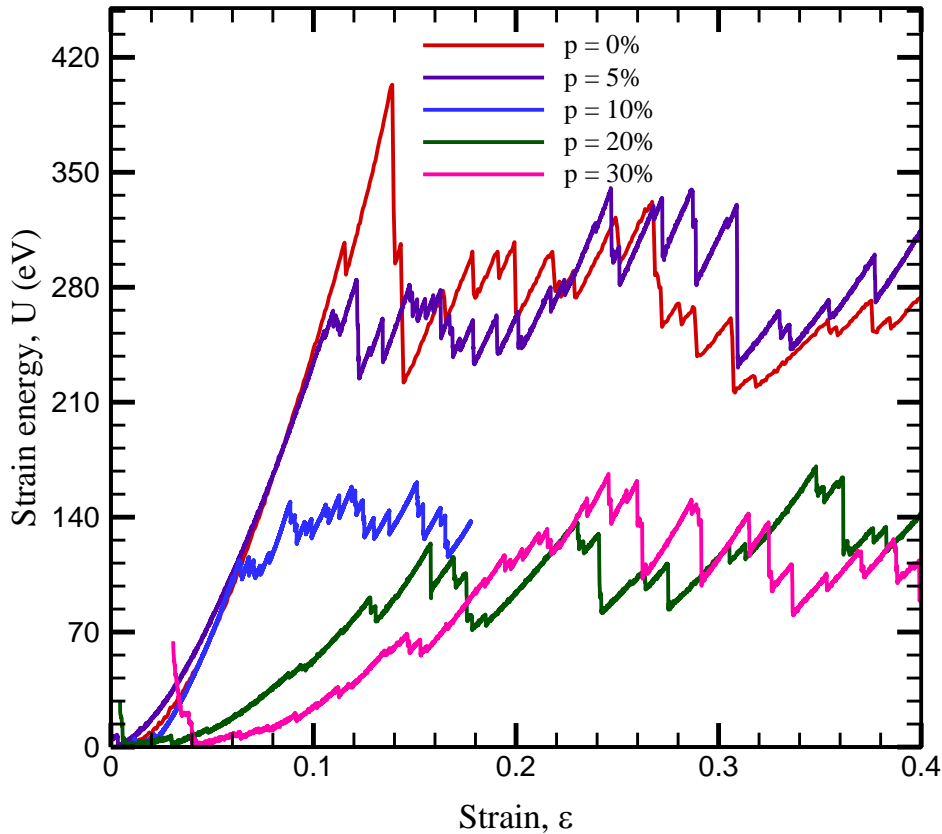


Figure 25. Variation of strain energy in crumpled graphene with applied strain at different degree of porosity with crumpling radius 19.3 Å under uniaxial tensile load along y axis.

In this study, the crumpling radius was 19.3. The maximum strain energy is 400 eV, which decreases to 120 eV with 20% porosity. When the porosity of the graphene electrode exceeds a particular threshold, the material's mechanical characteristics deteriorate, resulting in a reduction in the amount of strain energy that can be stored. To attain the appropriate performance characteristics, careful tuning of the porosity content may be required. However, the influence of porosity on strain energy in crumpled graphene is not as large as it is in flat graphene, which could be because the crumpling process provides some structural reinforcement to the material, making it less sensitive to the presence of pores.

3.1.4.2.3 Variation in strain energy in porous CG at radius 14.7 Å

Figure 26 shows that with greater porosity, the fracture toughness point is obtained at a higher strain (about 0.3) than the previous one (around 0.25).

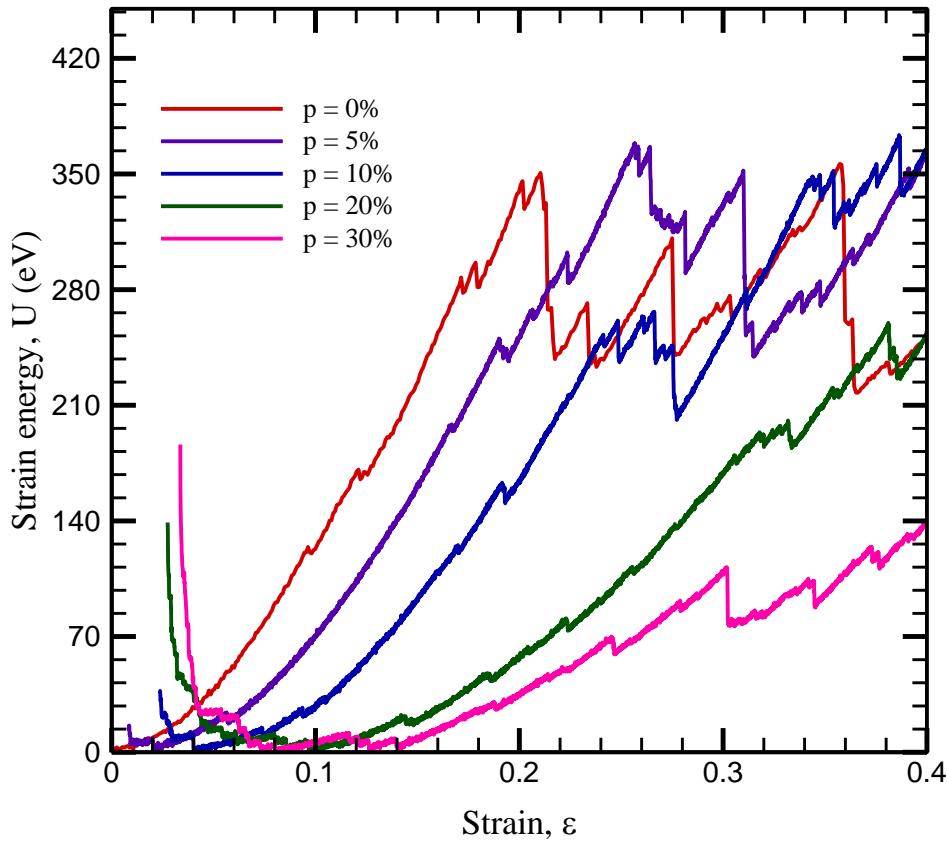


Figure 26. Variation of strain energy in crumpled graphene with applied strain at different degree of porosity with crumpling radius 14.7 Å under uniaxial tensile load along y axis.

Figure 25 shows that with greater porosity, the fracture toughness point is obtained at a higher strain (about 0.3) than the previous one (around 0.25). With this degree of crumpling and less porosity, the maximum strain energy is nearly identical, roughly 360 eV when less porosity is present. At 20% and 30% porosity, this value drops to 270 eV and 170 eV, respectively. The lower strain energy values seen with increasing porosity reflect this, as the material is less able to store energy due to its weaker structure. Furthermore, the degree of crumpling influences strain energy values, as more crumpling increases surface area and potential for energy storage, resulting in larger strain energy values at lower porosities.

3.1.4.2.4 Variation in strain energy in porous CG at radius 12.3 Å

Figure 27 depicts the fluctuation of strain energy with strain at various porosity levels with applied strain when the crumpling radius is 12.3 Å.

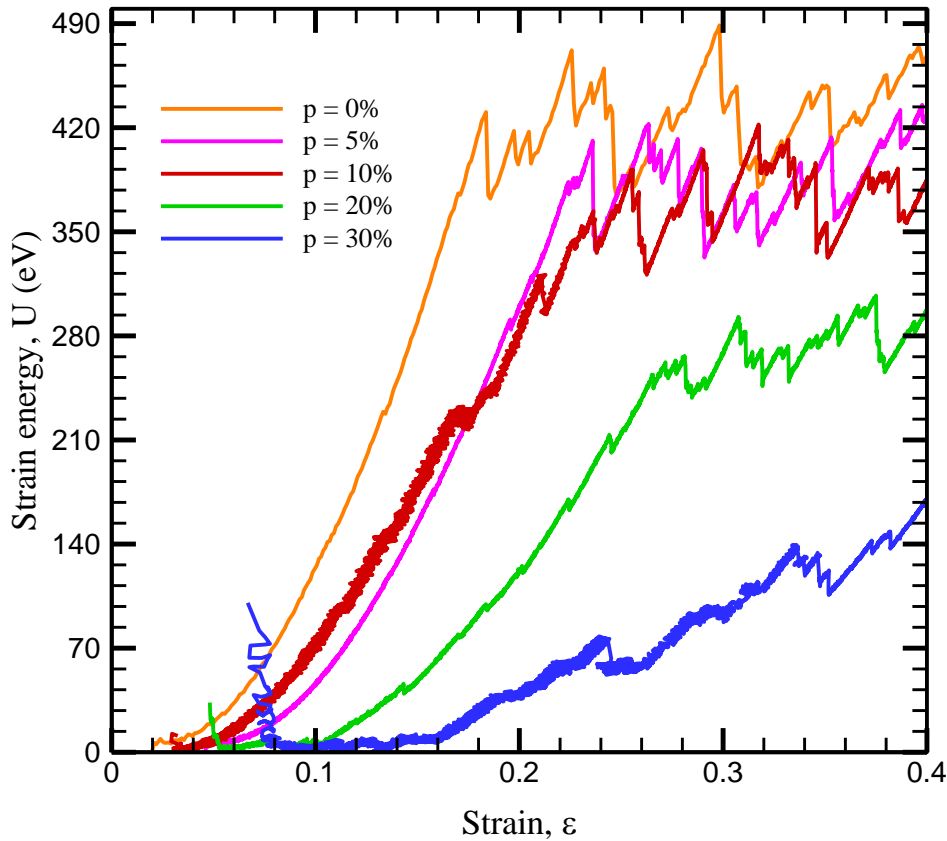


Figure 27. Variation of strain energy in crumpled graphene with applied strain at different degree of porosity with crumpling radius 12.3 Å under uniaxial tensile load along y axis.

Fracture occurs with greater strain than the prior one. Graphene collapses with 0.3 and 0.35 applied strain and 30% porosity, same as it does with 14.7 and 12.3 crumpling radius. The strain energy is greater with this crumpling radius than with the prior crumpling radius we studied for each amount of pore added. Overall, crumpling and porosity produce a more complex and changeable relationship among strain energy and applied strain.

3.1.4.2.5 Variation in strain energy in porous CG at radius 7.6 Å

Figure 28 depicts the fluctuation of strain energy with strain at various porosity levels with applied strain when the crumpling radius is 7.6 Å.

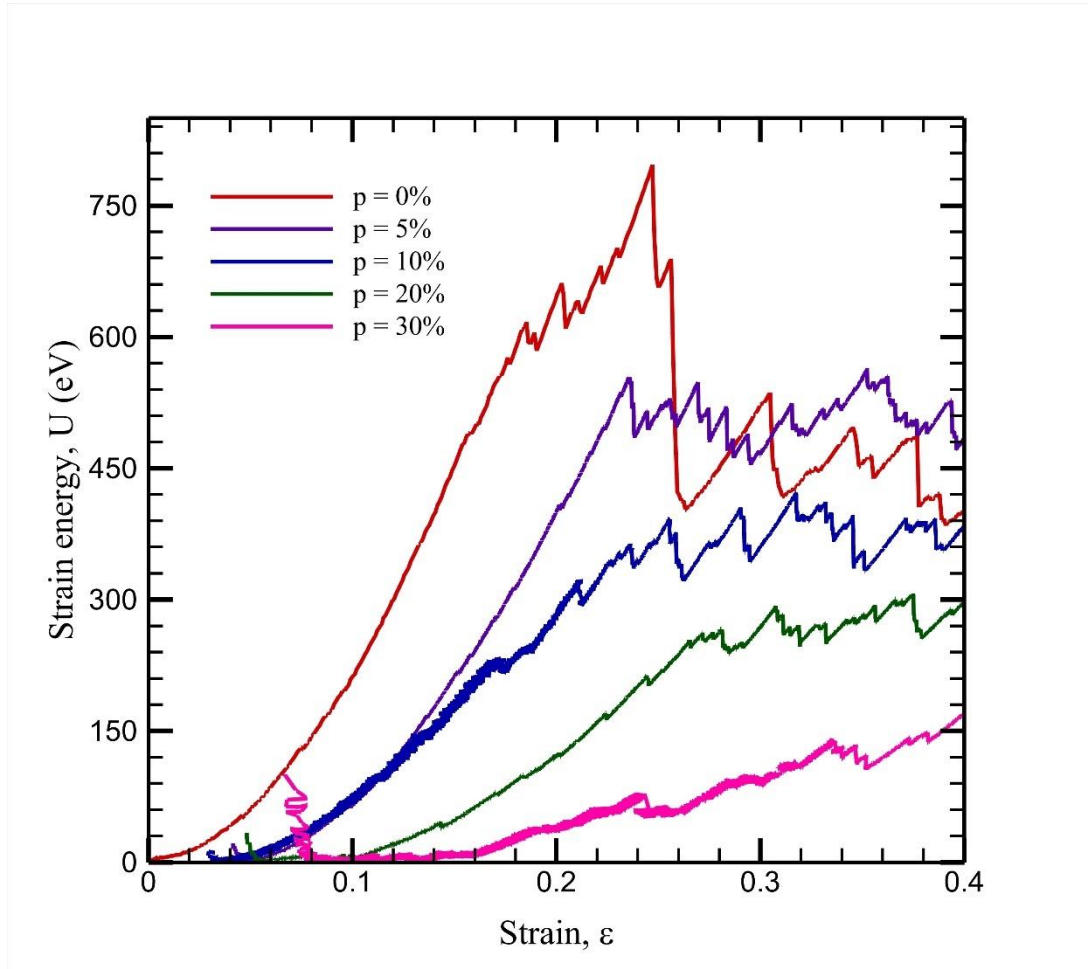


Figure 28. Variation of strain energy in crumpled graphene with applied strain at different degree of porosity with crumpling radius 7.6 Å under uniaxial tensile load along y axis.

Fracture occurs with the same strain as the previous one (i.e., 12.3) at 30% porosity about 0.35. This toughness point was attained with a smaller pore graphene electrode at varied applied

strains. The strain energy value grows until the fracture toughness point is met. The development of strain energy with increasing porosity seems to be similar to that seen in the prior figures, with increased porosity resulting in a decrease in strain energy.

3.1.5 CG under Uniaxial Compressive Load

In this study, a crumpled graphene of radius 7.6 \AA has been studied under uniaxial compressive load along x and y direction from elastic to plastic deformation region and then the load is removed to observe the unloading process.

3.1.5.1 Fracture under Uniaxial Compressive Load on Non-porous CGs along x-axis

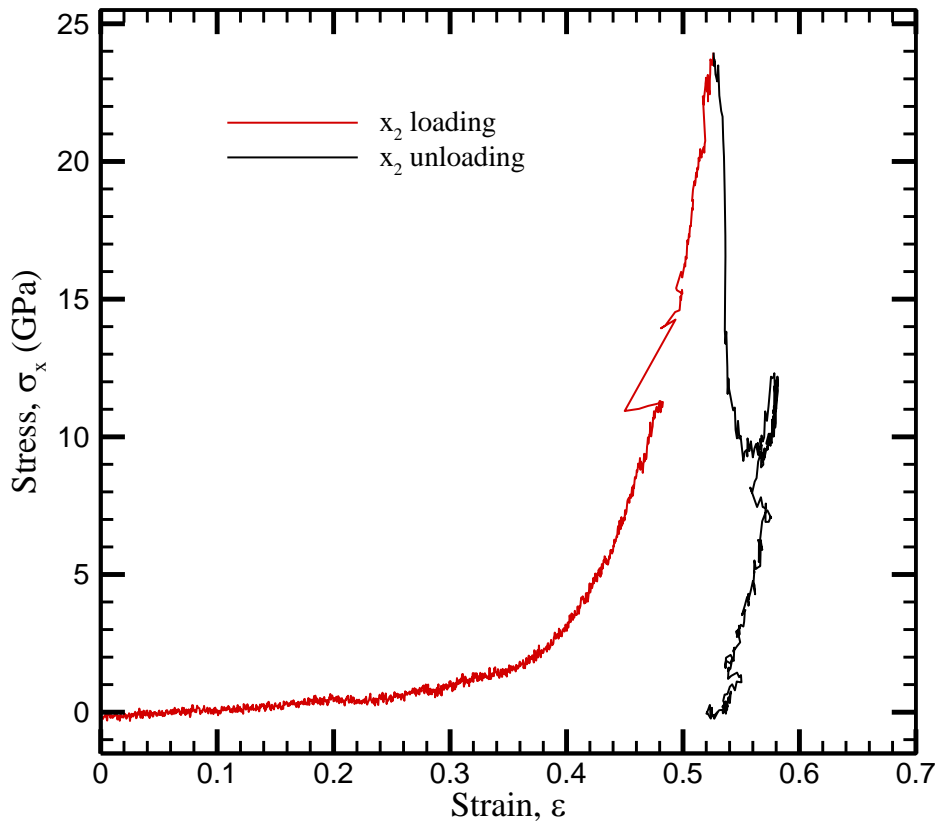


Figure 29. Variation of stress as a function of strain under uniaxial compressive loading for a non-porous CG of radius 7.6 \AA along x direction.

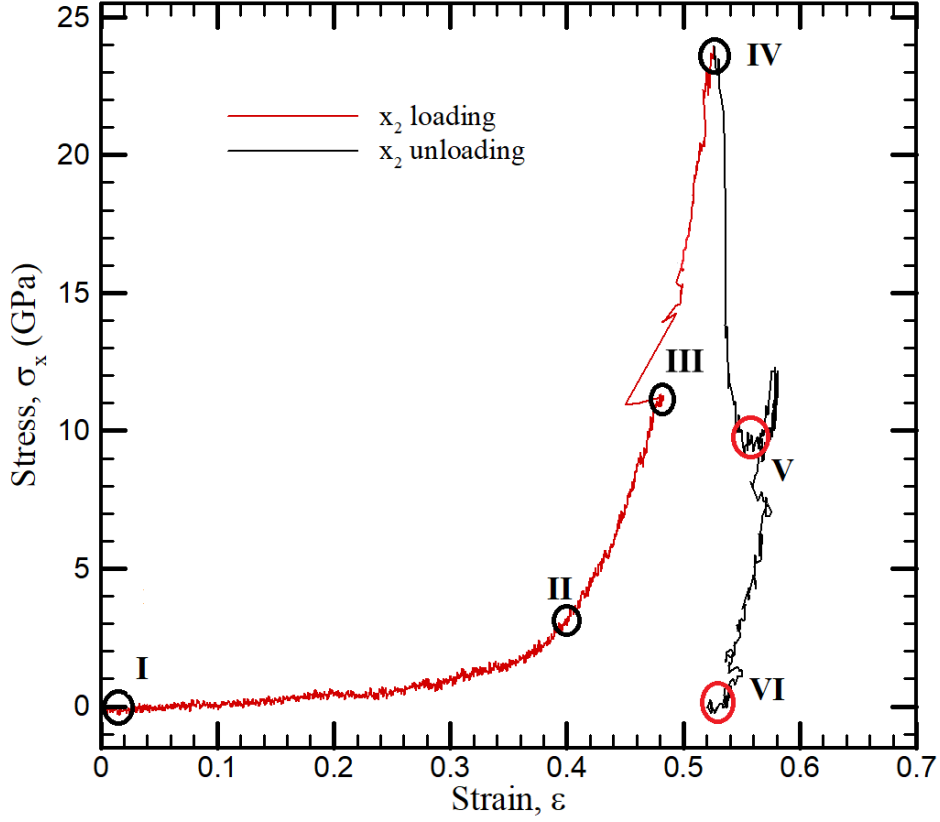
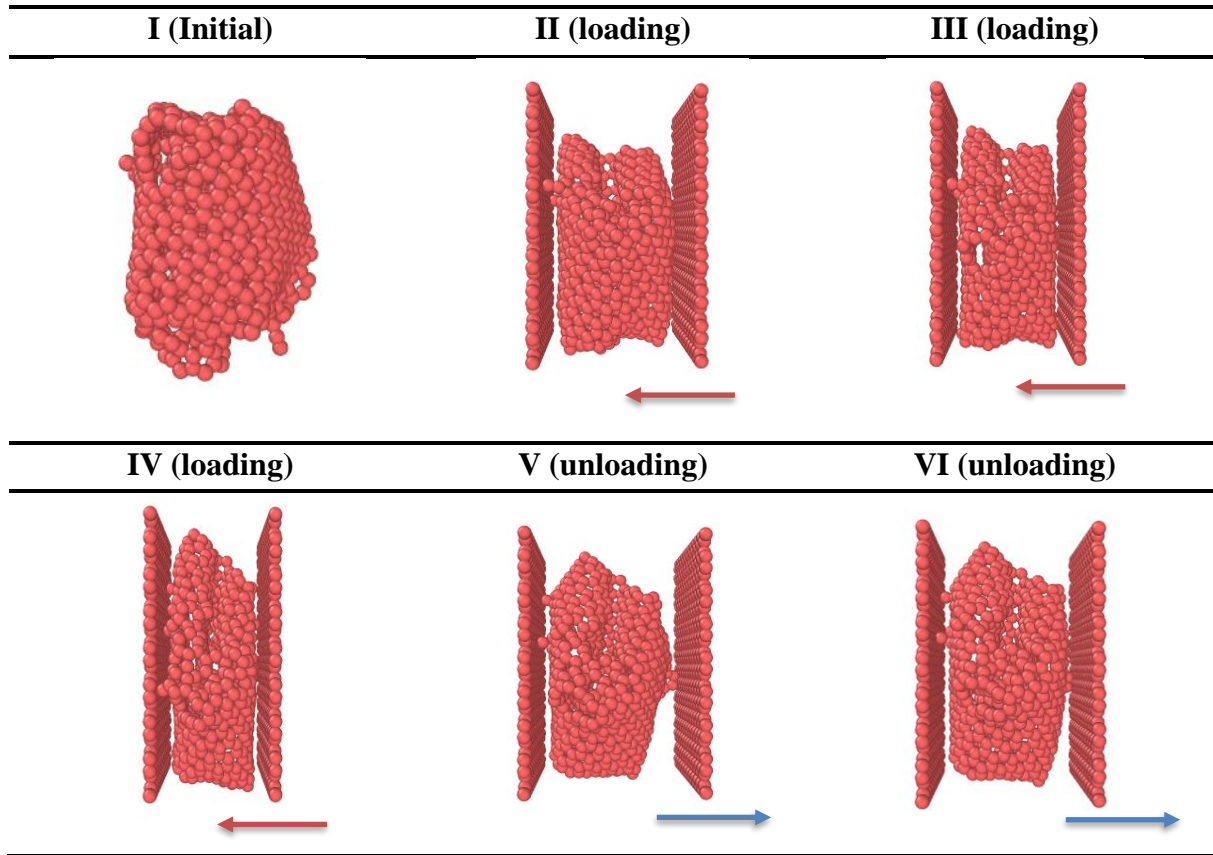


Figure 30. Variation of stress as a function of strain under uniaxial compressive loading for a non-porous CG of radius 7.6Å along x axis.

The compressive load on the CG structure along x axis is applied till fracture at about 24 GPa and then the load is removed gradually at the same strain rate applied while loading. The unloading curve is not following the loading curve. This is happening because of the plastic deformation of the CG structure. Consequently, unloading curve is falling to zero without following the loading path. **Figure 30** is showing the CG different states at different compressive load.

Table 12. Different stages of CG at crumpling radius of 7.6 Å under uniaxial compressive loading along x.



In the compressive loading scenario you described, where two graphene plates are compressing a crumpled graphene (CG) structure, the stress-strain curve exhibits a distinct behavior.

1. Loading Process:

- Initially, as the right plate moves inward, the CG structure undergoes compression. The stress increases gradually with increasing strain, following the loading curve.
- At point III, where the stress reaches around 11 GPa, a fracture occurs in the CG system. This fracture causes local disruptions and leads to fluctuations in the graph, indicating a sudden change in the material's behavior.
- As the loading continues, the stress reaches its maximum value at point IV, with a magnitude of 24 GPa. At this stage, the CG structure has experienced significant deformation and stress concentration.

- The loading process is characterized by the plastic deformation of the CG system, meaning that the material does not fully recover its original shape after unloading.

2. Unloading Process:

- After reaching the maximum stress at point IV, the unloading process begins, and the stress starts to decrease.
- It's important to note that due to the fracture and the deformed state retained in the CG system, the unloading curve does not follow the same path as the loading curve.
- Instead, the unloading curve exhibits a hysteresis effect, meaning that the stress decreases at a slower rate compared to the loading process.
- This hysteresis loop represents the irreversible or inelastic deformation that occurred during the loading process, resulting in a plastic deformation curve.

In summary, the observed behavior in the stress-strain curve indicates that the CG structure undergoes plastic deformation during compression. The fracture at point III and the irreversible deformation contribute to the retention of deformed states, leading to the hysteresis effect in the unloading curve. This behavior highlights the material's response to compressive loading and provides insights into the mechanical behavior of the CG system under these conditions.

3.1.5.2 Fracture under Uniaxial Compressive Load on Non-porous CGs along y-axis

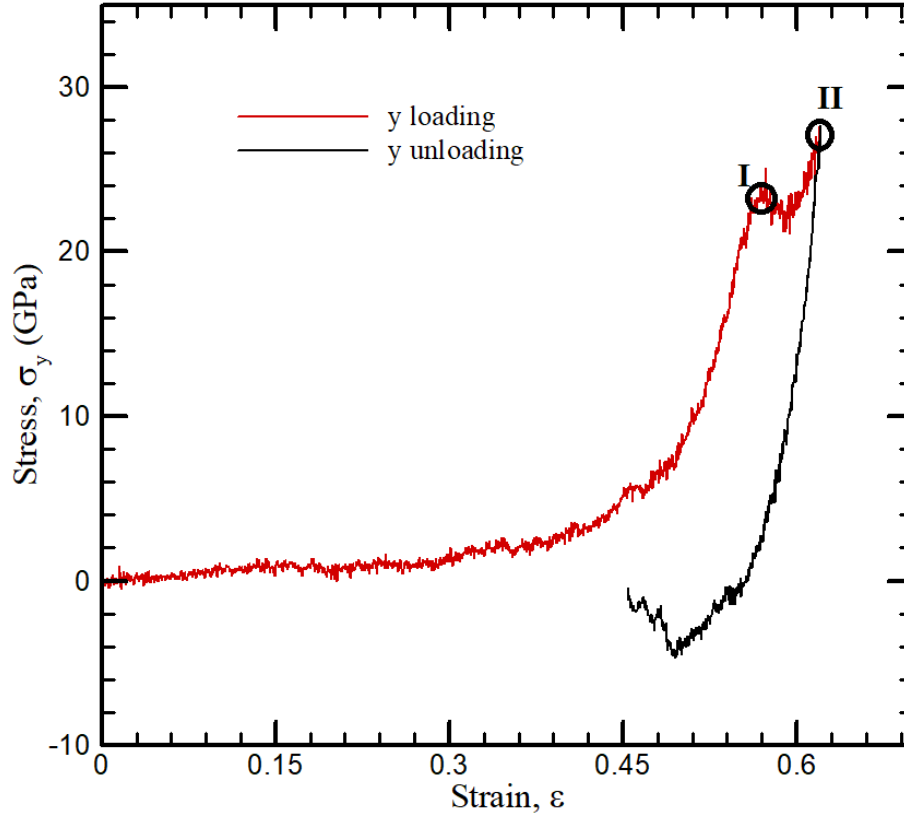


Figure 31. Variation of stress as a function of strain under uniaxial compressive loading for a non-porous CG of radius 7.6 Å along y axis.

Figure 31 shows the stress strain variation for a CG system with 7.6 Å radius. Two points are noted in the graph. Point I here is the first point to face fracture under compressive load at about 25 GPa. Moreover, the structure withstands the stress under plastic deformation until point II, to which the load has been increased. Then the unloading process starts. Following the process of unloading but before full recuperation, stress is reduced. These findings shed light on the CG structure's mechanical behavior and reveal how it reacts to compressive force along the y-axis.

Table 13. CG under compressive loading along y.

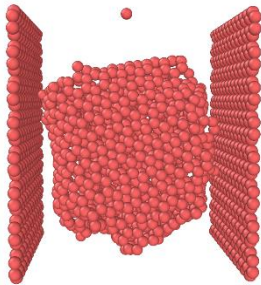
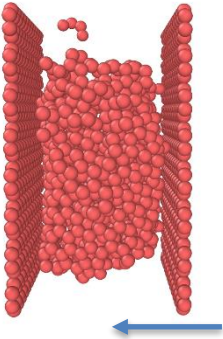
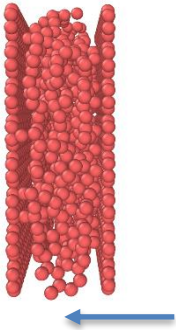
Initial	I	II
		

Table 13 depicts the initial state, state at point I and II of the CG structure. It is evident from the table that there are fractures appearing in the point I state and with the continuous loading process, point III shows the plastic deformation of the structure that cannot be retained.

3.2 Validation

The outcomes of the current investigation's simulation design were rigorously compared to those from reputable, previously published research in order to validate its use. The focus of the validation was on flat graphene as a reference because crumpled graphene's (CG) unique structure and manufacturing technique have a significant impact on the material's mechanical performances, which have been discussed earlier.

We carefully plotted the stress-strain curve, and determined the fracture toughness, and elastic modulus of the flat graphene system and compared them to well-known researches from earlier simulations and experiments. In order to evaluate the dependability and accuracy of the existing simulation approach, this comparison served as a vital benchmark.

A validation framework was created by comparing the simulation results with the predetermined values. This made it possible to analyze in great depth the patterns, trends, and similarities between the data that was acquired and the existing literature. The goal was to increase confidence in the simulation results by ensuring that the simulation architecture accurately depicts the fundamental mechanical behavior of CG.

Figure 32 illustrates a comparison between the stress strain curve from present study and a study from Dewapriya et al.[82]. Both studies have been conducted on a graphene sheet having dimensions $50 \times 50 \text{ \AA}$. The time step and strain rate were set at 0.001 ps^{-1} and 0.5 fs , respectively. Before applying strain, the sheet is given a 30 ps period of relaxation at 300 K temperature. The process of applying strain is different for the plotted studies. The first one applied strain in rescaling method, i.e., by *fix deform* command in LAMMPS.

However, in the present case, strain has been done in displacement control method. To be illustrated, by applying velocity to the movable portion of the system. It has been discussed in **CHAPTER 2**. From the graph stress up to 0.13 is shown similar to the past work. A full simulation till fracture has been conducted and a Fracture toughness of about 120 GPa has been found. Which is close to the experimented value for graphene, 130 GPa . [83] And an Elastic modulus has been found around 0.835 TPa .

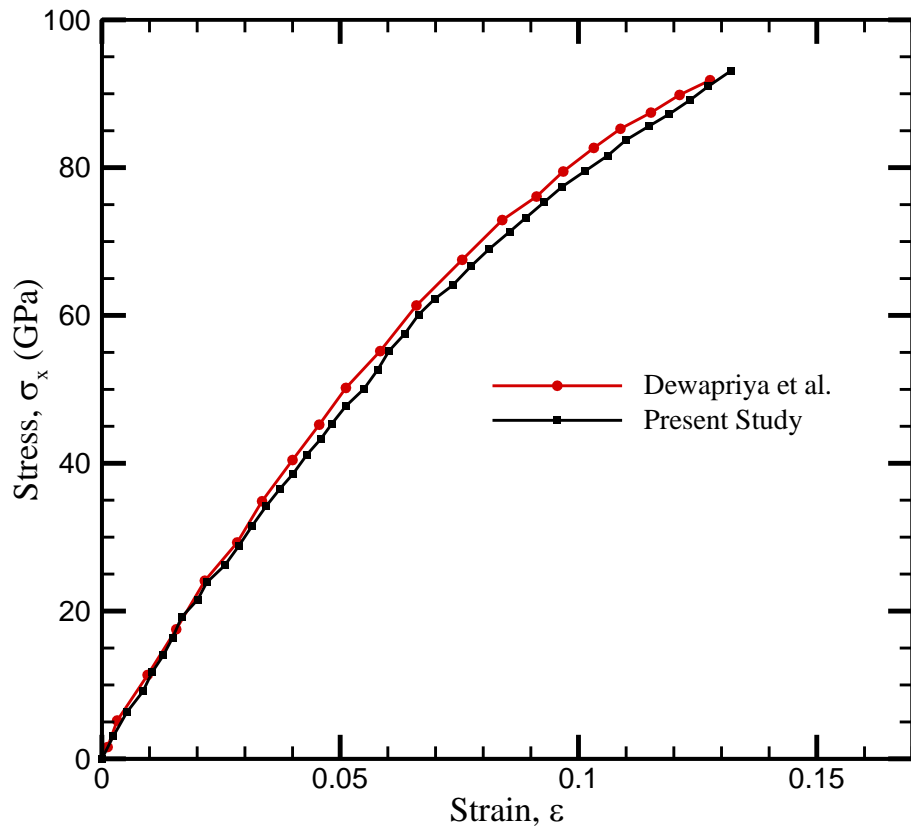


Figure 32. Variation of stress with applying strain along the armchair direction on a flat graphene for uniaxial tensile load along armchair direction.

Table 14. Young's modulus values reported in previous articles.

References	Methods	Elastic Modulus, GPa
Arroyo and Belytschko[84]	Continuum models	694
Kudin and Scuseria[85]	Ab initio and Quantum	1021
Ni and Bu[86]	MD simulations	1100
Tsai and Tu[32]	MD simulations	912
Georgantzinis et al. [87]	Finite element method	1367
Li and Chou[88]	Structural molecular mechanics	1033
Lee et al.[89]	Experiment	1033
Yupeng and Pan[90]	Experiment	891
Present study	MD simulations	835

In experimental findings, the Young's modulus ranged from 0.5 to 2 TPa. [91] The majority of studies, however, have reported on Young's modulus values near to 1TPa.[92] The value of Young's modulus has been reported in various papers, as shown in Table 14. The above discussion on graphene's mechanical behavior compared to previous studies shows the validity of the present study.

CHAPTER 4

Conclusion and Future Recommendations

4.1 Conclusion

The mechanical response of crumpled graphene with different magnitudes of crumpling and porosity to tensile loading has been investigated by molecular dynamics simulation. Response to compressive load has also been studied in case of crumpled graphene structure with a crumpling radius of 7.6 Å. The effect of morphological structure of the system on the mechanical behavior of crumpled graphene is also analyzed. Some key findings from the study can be summarized as

- Crumpling radius affects fracture toughness, elasticity under tensile loading. Initially, crumpleness lead to lower fracture toughness and elastic modulus in crumpled graphene (CG) due to increased brittleness. A considerable fall of 24% in fracture toughness and a 30% reduction in elastic modulus are observed as the crumpling radius reduces from 26.5 Å to 19.3 Å. Beyond a crumpling radius of 19.3 Å, however, a remarkable reversal takes place, and when the crumpling radius reaches 7.6Å, both fracture toughness and elastic modulus increase by 390% and 500%, respectively, which is a huge improvement.
- Porosity significantly impacts graphene's mechanical properties, making highly porous crumpled graphene structures more vulnerable. Fracture toughness, elastic modulus, and energy storing capability decrease substantially with increased porosity. With a change in porosity from 5% to 30% toughness of CG of radius 7.6 Å shows a decrease in toughness around 68%. However, at higher levels of crumpleness (lower radius), the detrimental effects of porosity can be partially compensated within a certain range.
- Strain energy is maximum at the fracture point for all cases. Moreover, the change in strain energy is also dependent on the crumpleness and porosity of graphene under tensile deformation. For a non-porous CG, the strain energy changes at a similar trend as the fracture toughness. When radius changes from 26.5 Å to 19.3 Å, a decrease in maximum strain energy is roughly 53% and opposite phenomenon occurs with further crumpling up to 7.6 Å, 128% more energy storing capability is observed.

- Porosity affects the strain energy adversely, for a CG with crumpling radius of 7.6 Å faces 66% degradation of maximum strain energy.
- Shape of the CG considered has great impact on its mechanical behavior. As mentioned earlier, compact structures (lower interlayer distance) results in higher fracture toughness and elastic modulus.
- Under compressive loading, CG tends to deform plastically and retains the deformed shape after unloading which is also dependent on the morphology of CG.
- Another important finding of the work is that it provides a better understanding of how strain affects the properties of the crumpled graphene. This is because specific deformations can affect the electronic properties of different structures.

4.2 Future Recommendations

For future work, the following points can be considered:

- The CG system of the present study was made from 5 nm x 5 nm graphene sheets. CG fabricated from larger graphene sheet can give a broader insight in addition to the present study.
- In this study, tensile force has been applied thorough dynamic loading of strain. The effect of incremental strain can also be observed to increase the scope of the study.
- This study encompasses the compressive analysis only for non-porous CGs. The effect of compressive loading on porous CG can be an interesting field to explore.
- It is possible to create composite materials with improved mechanical properties by embedding metallic nanoparticles (such as Ni, Cu). The mechanical behavior of these composites is a promising area of research.

The huge potential of this topic is only partially explored by the current study. There are many additional paths to go, and the options are limitless.

References

1. Zhang, L., et al., *Porous 3D graphene-based bulk materials with exceptional high surface area and excellent conductivity for supercapacitors*. Scientific Reports, 2013. **3**(1): p. 1408.
2. Levchenko, I., et al., *The large-scale production of graphene flakes using magnetically-enhanced arc discharge between carbon electrodes*. Carbon, 2010. **48**(15): p. 4570-4574.
3. Glukhova, O., V. Mitrofanov, and M. Slepchenkov, *The effect of the occurrence of a magnetic field of a current loop in hybrid graphene / C60 carbon systems*. Letters on Materials, 2020. **10**: p. 491-495.
4. Shunaev, V. and O. Glukhova, *Super square carbon nanotube networks: mechanical properties and electric conductivity*. Letters on Materials, 2019. **9**: p. 136-141.
5. Sun, H., Z. xu, and C. Gao, *Aerogels: Multifunctional, Ultra-Flyweight, Synergistically Assembled Carbon Aerogels (Adv. Mater. 18/2013)*. Advanced materials (Deerfield Beach, Fla.), 2013. **25**.
6. Zhong, L., H. Gao, and X. Li, *Atomistic simulations of the tensile behavior of graphene fibers*. Extreme Mechanics Letters, 2020. **37**: p. 100699.
7. Zhang, L., et al., *Porous 3D graphene-based bulk materials with exceptional high surface area and excellent conductivity for supercapacitors*. Scientific reports, 2013. **3**: p. 1408.
8. Ding, R., et al., *Nanostructured materials for electrochemical capacitors*. 2022.
9. Oakes, L., et al., *Surface engineered porous silicon for stable, high performance electrochemical supercapacitors*. Scientific reports, 2013. **3**: p. 3020.
10. Wang, M.-x., et al., *Preparation of High Surface Area Nano-Structured Graphene Composites*. Vol. 41. 2012. 95-105.
11. Vivekchand, S., et al., *Graphene-based electrochemical supercapacitors*. Journal of Chemical Sciences, 2008. **120**: p. 9-13.
12. Tarek, Y., et al., *Wrinkled Flower-Like rGO intercalated with Ni(OH)₂ and MnO₂ as High-Performing Supercapacitor Electrode*. ACS Omega, 2022. **7**.
13. Mao, S., et al., *A General Approach to One-Pot Fabrication of Crumpled Graphene-Based Nanohybrids for Energy Applications*. ACS nano, 2012. **6**: p. 7505-13.
14. Castro Neto, A., F. Guinea, and N. Peres, *Drawing conclusions from graphene*. Physics World, 2006. **19**: p. 33-37.
15. Bae, S., et al., *Towards industrial applications of graphene electrodes*. Physica Scripta, 2012. **2012**(T146): p. 014024.
16. Yang, G., et al., *Structure of graphene and its disorders: a review*. Science and Technology of Advanced Materials, 2018. **19**: p. 613-648.
17. Cooper, D., et al., *Experimental Review of Graphene*. ISRN Condens. Matter Phys., 2011. **2012**.
18. Wang, X., L. Zhi, and K. Müllen, *Transparent, Conductive Graphene Electrodes for Dye-Sensitized Solar Cells*. Nano letters, 2008. **8**: p. 323-7.

19. Yi, M. and Z. Shen, *A review on mechanical exfoliation for the scalable production of graphene*. Journal of Materials Chemistry A, 2015. **3**(22): p. 11700-11715.
20. Kataria, S., et al., *Chemical vapor deposited graphene: From synthesis to applications*. 2021.
21. Gao, M., et al., *Epitaxial growth and structural property of graphene on Pt(111)*. Applied Physics Letters, 2011. **98**(3): p. 033101.
22. Deng, S. and V.J.M.T. Berry, *Wrinkled, rippled and crumpled graphene: an overview of formation mechanism, electronic properties, and applications*. 2016. **19**(4): p. 197-212.
23. Xu, K., P. Cao, and J.R. Heath, *Scanning Tunneling Microscopy Characterization of the Electrical Properties of Wrinkles in Exfoliated Graphene Monolayers*. Nano Letters, 2009. **9**(12): p. 4446-4451.
24. Saha, V., et al. *Synthesis and characterization of reduced graphene oxide reinforced polymer matrix composite*. in *IOP Conference Series: Materials Science and Engineering*. 2018. IOP Publishing.
25. Han, Z., et al., *Ammonia solution strengthened three-dimensional macro-porous graphene aerogel*. Nanoscale, 2013. **5**.
26. Balankin, A. and O. Susarrey, *Entropic rigidity of a crumpling network in a randomly folded thin sheet*. Physical review. E, Statistical, nonlinear, and soft matter physics, 2008. **77**: p. 051124.
27. Meyer, J., et al., *The structure of suspended graphene sheets*. Nature, 2007. **446**: p. 60-3.
28. Luo, J., et al., *Compression and aggregation-resistant particles of crumpled soft sheets*. 2011. **5**(11): p. 8943-8949.
29. Tang, Z., et al., *Porous crumpled graphene with hierarchical pore structure and high surface utilization efficiency for supercapacitor*. 2018. **272**: p. 40-43.
30. Zang, J., et al., *Multifunctionality and control of the crumpling and unfolding of large-area graphene*. 2013. **12**(4): p. 321-325.
31. Becton, M., L. Zhang, and X.J.P.C.C.P. Wang, *Mechanics of graphyne crumpling*. 2014. **16**(34): p. 18233-18240.
32. Tsai, J.-L. and J.-F. Tu, *Characterizing mechanical properties of graphite using molecular dynamics simulation*. Materials & Design, 2010. **31**: p. 194–199.
33. Ranjbartoreh, A., et al., *Advanced mechanical properties of graphene paper*. Journal of Applied Physics - J APPL PHYS, 2011. **109**.
34. Luo, J., et al., *Compression and Aggregation-Resistant Particles of Crumpled Soft Sheets*. ACS nano, 2011. **5**: p. 8943-9.
35. Cranford, S. and M. Buehler, *Packing efficiency and accessible surface area of crumpled graphene*. 2012.
36. Chang, C., et al., *How graphene crumples are stabilized?* RSC Adv., 2013. **3**: p. 2720-2726.
37. Mathew, E. and M. Balachandran, *Crumpled and porous graphene for supercapacitor applications: a short review*. Carbon Letters, 2021. **31**.
38. Zang, J., et al., *Multifunctionality and Control of the Crumpling and Unfolding of Large-Area Graphene*. Nature materials, 2013. **12**.

39. Baimova, Y., et al., *Review on crumpled graphene: Unique mechanical properties*. Reviews on Advanced Materials Science, 2014. **39**: p. 69-83.
40. Montazeri, A., et al., *A molecular dynamics investigation of buckling behaviour of hydrogenated graphene*. Molecular Simulation, 2014. **41**.
41. Becton, M., L. Zhang, and X. Wang, *On the Crumpling of Polycrystalline Graphene by Molecular Dynamics Simulation*. Phys. Chem. Chem. Phys., 2015. **17**.
42. Zang, J., et al., *Stretchable and High-Performance Supercapacitors with Crumpled Graphene Papers*. Scientific reports, 2014. **4**: p. 6492.
43. Baimova, Y., et al., *From flat graphene to bulk carbon nanostructures: From flat to bulk graphene*. physica status solidi (b), 2015. **252**.
44. Baimova, Y., et al., *Mechanical properties of crumpled graphene under hydrostatic and uniaxial compression*. Journal of Physics D: Applied Physics, 2015. **48**: p. 095302.
45. Nicholl, R., et al., *The Effect of Intrinsic Crumpling on the Mechanics of Free-Standing Graphene*. Nature Communications, 2015. **6**.
46. Yamaletdinov, R. and Y. Pershin, *Finding Stable Graphene Conformations from Pull and Release Experiments with Molecular Dynamics*. Scientific Reports, 2017. **7**: p. 42356.
47. Katin, K., V. Prudkovskiy, and M. Maslov, *Molecular dynamics simulation of nickel-coated graphene bending*. Micro & Nano Letters, 2018. **13**: p. 160-164.
48. Xia, W., et al., *Structure and Dynamics of a Graphene Melt*. ACS Nano, 2018. **12**.
49. Baimova, J. and L. Safina, *Molecular dynamics simulation of fabrication of Ni-graphene composite: temperature effect*. Micro & Nano Letters, 2019. **15**.
50. Bian, L. and M. Gao, *Thermal environment and strain energy related micro-model for properties of carbon nanotubes*. Materials Science and Engineering: B, 2019. **244**: p. 72-80.
51. Raghuraman, S., et al., *Mechanics of nanoscale crumpled graphene measured by Atomic Force Microscopy*. Extreme Mechanics Letters, 2020. **40**: p. 100873.
52. Sheinerman, A.G., *Plastic deformation and fracture processes in metal/graphene composites: a review*. Critical Reviews in Solid State and Materials Sciences, 2021. **47**: p. 1-28.
53. Liao, Y., et al., *Size-Dependent Structural Behaviors of Crumpled Graphene Sheets*. Carbon, 2020. **174**.
54. Folorunso, O., et al., *Comparative study of graphene-polypyrrole and borophene-polypyrrole composites: molecular dynamics modeling approach*. Engineering Solid Mechanics, 2021. **9**: p. 311-322.
55. Baimova, Y., et al., *Mechanical properties of bulk carbon nanostructures: Effect of loading and temperature*. Physical chemistry chemical physics : PCCP, 2014. **16**.
56. Javvaji, B., et al., *Mechanical properties of Graphene: Molecular Dynamics simulations correlated to continuum based scaling laws*. Computational Materials Science, 2016. **125**: p. 319-327.
57. Zhan, H., et al., *Graphene helicoid as novel nanospring*. Carbon, 2017. **120**.

58. Valentini, P., W. Gerberich, and T. Dumitrică, *Phase-Transition Plasticity Response in Uniaxially Compressed Silicon Nanospheres*. Physical review letters, 2007. **99**: p. 175701.
59. Fang, T.-H. and J.-H. Wu, *Molecular dynamics simulations on nanoindentation mechanisms of multilayered films*. Computational Materials Science, 2008. **43**: p. 785-790.
60. Rivas Murillo, J., et al., *A molecular dynamics investigation of hydrostatic compression characteristics of mineral Jennite*. Cement and Concrete Research, 2017. **99**: p. 62-69.
61. Kilymis, D., et al., *Uniaxial compression of silicon nanoparticles: An atomistic study on the shape and size effects*. Acta Materialia, 2018. **158**: p. 155-166.
62. Zhang, Y., Q. Li, and Y. He, *ReaxFF Molecular Dynamics Simulation of Hydrostatic and Uniaxial Compression of Nitrate Energetic Materials*. ACS Omega, 2020. **XXXX**.
63. Baimova, Y., P. Polyakova, and S. Shcherbinin, *Effect of the Structure Morphology on the Mechanical Properties of Crumpled Graphene Fiber*. Fibers, 2021. **9**: p. 85.
64. Punckt, C., et al., *Electrochemical Performance of Graphene as Effected by Electrode Porosity and Graphene Functionalization*. Electroanalysis, 2010. **22**: p. 2834-2841.
65. Wang, Z.-L., et al., *In Situ Fabrication of Porous Graphene Electrodes for High-Performance Energy Storage*. ACS Nano, 2013. **7**(3): p. 2422-2430.
66. Zhang, X., et al., *Recent Advances in Porous Graphene Materials for Supercapacitor Applications*. RSC Adv., 2014. **4**.
67. Frenkel, D. and B. Smit, *Understanding molecular simulation : from algorithms to applications*. 2nd ed. Vol. 50. 1996.
68. Adams, J.B., *Bonding Energy Models*, in *Encyclopedia of Materials: Science and Technology*, K.H.J. Buschow, et al., Editors. 2001, Elsevier: Oxford. p. 763-767.
69. Pastor, R., B. Brooks, and A. Szabo, *An analysis of the accuracy of Langevin and molecular dynamics algorithm*. Molecular Physics - MOL PHYS, 1988. **65**: p. 1409-1419.
70. Allen, A., *Tumors in Domestic Animals, 4th Edition*. The Canadian veterinary journal. La revue veterinaire canadienne, 2003. **44**.
71. Lobkovsky, A., et al., *Scaling Properties of Stretching Ridges in a Crumpled Elastic Sheet*. Science, 1995. **270**: p. 1482-1485.
72. Stuart, S., A. Tutein, and J. Harrison, *A reactive potential for hydrocarbons with intermolecular interactions*. The Journal of Chemical Physics, 2000. **112**: p. 6472-6486.
73. Stuart, S.J., A.B. Tutein, and J.A. Harrison, *A reactive potential for hydrocarbons with intermolecular interactions*. The Journal of Chemical Physics, 2000. **112**(14): p. 6472-6486.
74. Badar, M., et al., *Molecular Dynamics Simulations: Concept, Methods, and Applications*. 2020.
75. Raad, M., *Fundamentals of Molecular Dynamics Simulations*. 2015.

76. Hearn, E.J., *CHAPTER 11 - STRAIN ENERGY*, in *Mechanics of Materials 1 (Third Edition)*, E.J. Hearn, Editor. 1997, Butterworth-Heinemann: Oxford. p. 254-296.
77. Zhan, H., et al., *Graphene helicoid as novel nanospring*. Carbon, 2017. **120**: p. 258-264.
78. Krylova, K., et al., *Methodology for Molecular Dynamics Simulation of Plastic Deformation of a Nickel/Graphene Composite*. Materials, 2022. **15**: p. 4038.
79. Xu, Z. and C. Gao, *Graphene chiral liquid crystals and macroscopic assembled fibres*. Nature Communications, 2011. **2**(1): p. 571.
80. xu, Z., et al., *Ultrastrong Fibers Assembled from Giant Graphene Oxide Sheets*. Advanced materials (Deerfield Beach, Fla.), 2013. **25**.
81. Xin, G., et al., *Highly Thermally Conductive and Mechanically Strong Graphene Fibers*. Science (New York, N.Y.), 2015. **349**: p. 1083-7.
82. Dewapriya, N., A.S. Phani, and N. Rajapakse, *Influence of temperature and free edges on the mechanical properties of graphene*. Modelling and Simulation in Materials Science and Engineering, 2013. **21**: p. 065017.
83. Li, C. and T.-W. Chou, *A structural mechanics approach for the analysis of carbon nanotubes*. International Journal of Solids and Structures, 2003. **40**(10): p. 2487-2499.
84. Arroyo, M., *Finite Crystal elasticity of carbon nanotubes based on the exponential Cauchy-Born rule*. Phys. Rev. B, 2004. **69**.
85. Kudin, K., G. Scuseria, and B. Yakobson, *C₂F, BN, and C nanoshell elasticity from ab initio computations*. Physical Review B, 2001. **64**: p. 235406.
86. Ni, Z., et al., *Anisotropic mechanical properties of graphene sheets from molecular dynamics*. Physica B-condensed Matter - PHYSICA B, 2010. **405**: p. 1301-1306.
87. Georgantzinos, S.K., G. Giannopoulos, and N.K. Anifantis, *Numerical investigation of elastic mechanical properties of graphene structures*. Materials and Design, 2010. **31**: p. 4646-4654.
88. Li, C. and T.-W. Chou, *A structural mechanics approach for the analysis of carbon nanotubes*. International Journal of Solids and Structures, 2003. **40**: p. 2487-2499.
89. Lee, C., et al., *Measurement of the Elastic Properties and Intrinsic Strength of Monolayer Graphene*. Science (New York, N.Y.), 2008. **321**: p. 385-8.
90. Zhang, Y. and C. Pan, *Measurements of mechanical properties and number of layers of graphene from nano-indentation*. Diamond and Related Materials, 2012. **24**: p. 1-5.
91. Cooper, D.R., et al., *Experimental Review of Graphene*. ISRN Condensed Matter Physics, 2012. **2012**: p. 501686.
92. Inglesfield, J.E., *Physics of Graphite*. Physics Bulletin, 1982. **33**(9): p. 333.

Appendices

Appendix-A:

LAMMPS code for crumpling flat graphene sheet:

```
### Credit to Eric N. Hahn ###
```

```
### ericnhahn@gmail.com ###
```

```
variable name string graphene_crumple_v2
```

```
log log.${name}
```

```
#-----Initialize Simulation-----
```

```
dimension      3
```

```
units          metal
```

```
atom_style     atomic
```

```
#-----Create Atoms-----
```

```
boundary        p p p
```

```
variable sixth equal "1/6"
```

```
variable twothirds equal "2/3"
```

```
variable alattice equal "2.4595"
```

```
variable a1lattice equal "1"
```

```
variable a2lattice equal "1.73203"
```

```
lattice custom ${alattice} a1 ${a1lattice} 0 0 a2 0 ${a2lattice} 0 basis 0 0 0 basis 0.5 ${sixth}
0 basis 0.5 0.5 0 basis 0 ${twothirds} 0
```

```
#what size do you want the graphene? assuming square sheet
```

```
variable boxside equal 50
```

```
variable xside equal "round(v_boxside/v_a1lattice/v_alattice/2)" #round ensures that we get
complete unit cells
```

```
variable yside equal "round(v_boxside/v_a2lattice/v_alattice/2)"
```

```

region    box block  -${xside} ${xside} -${yside} ${yside} -3 3 units lattice
region    graphene block  -${xside} ${xside} -${yside} ${yside} 0 0.1 units lattice
create_box      1 box
create_atoms    1 region graphene

```

```

mass * 12.011

```

```

#-----Define Interatomic Potential-----

```

```

pair_style airebo/morse 3.0
pair_coeff * * CH.airebo-m C
compute 3 all pe/atom
compute 4 all stress/atom NULL pair

```

```

#-----Run the simulation for thermal equilibration-----

```

```

velocity all create 178 4928459 dist gaussian
fix 1 all npt temp 298 298 .4 x 0.0 0.0 .5 y 0.0 0.0 .5
thermo 10
thermo_style custom step pe ke etotal temp lx ly lz press atoms

```

```

dump 1 all custom 25 dump.${name}.* id x y z vx vy vz c_3 c_4[1] c_4[2] c_4[3]
timestep 0.001

```

```

fix bp all balance 250 1 shift z 10 1

```

```

thermo_style custom step temp ke pe press pxx pyy vol
variable runeq equal 1000
run ${runeq}

```

```

group graphene region graphene
variable ymn equal ylo+4

```

```
variable ymx equal yhi-4
```

```
variable xmn equal xlo+4
```

```
variable xmx equal xhi-4
```

```
region middle block ${xmn} ${xmx} ${ymn} ${ymx} -5 5 units box
```

```
group middle region middle
```

```
group edge subtract graphene middle
```

```
#-----Run the simulation for confinement -----
```

```
unfix 1
```

```
change_box all boundary s s s
```

```
run 0
```

```
variable r0 equal (ylo^2+xlo^2+zlo^2)^0.5
```

```
variable r0fix equal ceil(${r0}) #rounding up here makes it so that the initial radius is larger  
than the furthest C atom
```

```
#and later helps gets us closer to a round number of steps
```

```
print "The starting radius of the compressing sphere is ~${r0fix} A"
```

```
variable rate equal 1.25 #A/ps
```

```
variable deltat equal "dt"
```

```
variable radius equal "v_r0fix-(step-v_runeq)*dt*v_rate"
```

```
variable finalrad equal 10
```

```
variable numberofsteps equal round((${r0fix}-${finalrad})/(${deltat}*${rate}))
```

```
print "running ${numberofsteps} steps to reach a final radius of ~${finalrad} A"
```

```
fix constrain all indent 1 sphere 0 0 0 v_radius side in units box
```

```
thermo_style custom step temp ke pe press pxx pyy vol v_radius f_constrain[1] f_constrain[2]
```

```
fix nve all nve
```

```
run ${numberofsteps}
```

```
unfix constrain
```

```
thermo_style custom step temp ke pe press pxx pyy vol v_radius
run 2000 #sim for vis at final state
print "Job's done"
```

Appendix-B:

Matlab code for adding porosity:

```
%%S_043%%

%% Adding porosity to crumpled graphene structure by deleting random atoms
timestep = 91000; %declare timestep here for rename data file in that timestep.
M = data; % atoms data matrix
n = size(M,1); %Total number of atoms present
p = [5 10 20 30];
for i = 1:4
    % percentage of atoms to remove
    rmv_atm = round(p(1,i)*n/100); % number of atoms removed
    A = randperm(n,rmv_atm); % Generates random integers from 1 to rmv_atm
    Dum = M; %Dummy matrix
    for i = 1:rmv_atm
        Dum(A(1,i),:)=[]; % Replacing atoms position with zero that has to be deleted
    end
    M = Dum(any(Dum,2),:); % Removing zero rows and it's done
    pr_atm = size(M,1); % number of atoms remaining
    x_low = ceil(min(M(:,3)));
    x_high = ceil(max(M(:,3)))+1;
    y_low = ceil(min(M(:,4)));
    y_high = ceil(max(M(:,4)))+1;
    z_low = ceil(min(M(:,5)));
    z_high = ceil(max(M(:,5)))+1;
    % Data file creation
    fid = fopen("PorousData"+timestep+"_"+i+".lammps", 'w+t');
    fprintf(fid, '\n\n');
    fprintf(fid, '%d atoms\n', pr_atm);
```

```

fprintf(fid, '1 atom types\n\n');
fprintf(fid, '%0.2f %0.2f xlo xhi\n%0.2f %0.2f ylo yhi\n%0.2f %0.2f zlo
zhi\n\n',x_low,x_high,y_low,y_high,z_low,z_high);
fprintf(fid, 'Masses\n\n1 12.01\n\nAtoms\n\n');
for i = 1:pr_atm
    fprintf(fid, '%d %d %0.4f %0.4f %0.4f\n', M(i,1),M(i,2),M(i,3),M(i,4),M(i,5));
end
fclose(fid);
end

```

Appendix-C:

MATLAB code for creating a LAMMPS data file for atomic data style from atomic position matrix:

```

%%S_043%%
%% data style: Atomic
timestep = 9600;          %declare timestep here for rename data file in that timestep.
molecule_id = 1; % molecule id of each atom; same
atoms_data = zeros(size(data,1),5); % matrix for atomic data file
atoms_data(:,1) = [1:size(data,1)];%atomic id for all atoms; column 1
atoms_data(:,2) = [molecule_id];

co_ord = [data(:,2) data(:,3) data(:,4)]; % matrix for x y z co-ordinates
co_ord_upd = [co_ord(:,1)-min(co_ord(:,1)) co_ord(:,2)-min(co_ord(:,2)) co_ord(:,3)-
min(co_ord(:,3))];% updated matrix; more understandable
atoms_data(:,3:5) = [co_ord_upd]; % arranged data file

x_low = ceil(min(atoms_data(:,3)));
x_high = ceil(max(atoms_data(:,3)))+1;
y_low = ceil(min(atoms_data(:,4)));
y_high = ceil(max(atoms_data(:,4)))+1;
z_low = ceil(min(atoms_data(:,5)));
z_high = ceil(max(atoms_data(:,5)))+1;

```

```

xlswrite("s"+timestep+".xlsx",atoms_data); %creates an excel file for porosity code
% fid_1 = fopen(+timestep+".txt",'w+t');
% tot_atms = size(data,1);
% for i = 1:tot_atms
%
%               fprintf(fid_1,      '%d      %d      %0.4f      %0.4f      %0.4f\n',
atoms_data(i,1),atoms_data(i,2),atoms_data(i,3),atoms_data(i,4),atoms_data(i,5));
% end
% Data file creation
tot_atms = size(data,1); % number of atoms remaining
fid = fopen("arranged"+timestep+".data",'w+t');
fprintf(fid, '\n\n');
fprintf(fid, '%d atoms\n', tot_atms);
fprintf(fid, '1 atom types\n\n');
fprintf(fid,  '%0.2f  %0.2f  xlo  xhi\n%0.2f  %0.2f  ylo  yhi\n%0.2f  %0.2f  zlo
zhi\n\n',x_low,x_high,y_low,y_high,z_low,z_high);
fprintf(fid, 'Masses\n\n1 12.01\n\nAtoms\n\n');
for i = 1:tot_atms
    fprintf(fid,      '%d      %d      %0.4f      %0.4f      %0.4f\n',
atoms_data(i,1),atoms_data(i,2),atoms_data(i,3),atoms_data(i,4),atoms_data(i,5));
end
fclose(fid);
clear;

```

Appendix-D:

MATLAB code for post processing data and create dat file for stress strain curve:

```

%%S_043%%
clc;
% All = xlsread('graphene0_5.def1.xlsx',2);
% data = All(2:end,1:2);

```



```

%Import data and rename it to "all"
% prompt1 = "What is the percent porosity? ";
% percent_pore = input(prompt1)
prompt2 = "What is the radius? ";
radius = input(prompt2)
all = all{:,~};          % converting table to matrix. only if the importer fails to import data as
numeric matrix.
data(:,1) = round(all(:,1),2);
data(:,2) = round(all(:,2),1);
% plot(all(:,1),all(:,2))
hold on
unique_values = unique(data(:,1));
k = length(data(:,1));
p = zeros(length(unique_values),20);
a = 1;
for i = 1:length(unique_values)
    for j = a:k
        if data(j,1) == unique_values(i,1)
            p(i,j-a+1) = data(j,2);
        else
            a = j;
            break
        end
    end
end
for i = 1:length(unique_values)
    unique_values(i,2) = max(p(i,:));
end
[strain_min,I1] = min(unique_values(:,1));
[strain_max,I2] = max(unique_values(:,1));
strain_stress = unique_values(I1:I2,:);

```

```
strain = strain_min:0.006:strain_max;  
stress = spline(strain_stress(:,1),strain_stress(:,2),strain);  
Final = zeros(length(strain),2);  
    Final(:,1) = round(strain,3);  
    Final(:,2) = round(stress,1);  
plot(Final(:,1),Final(:,2))  
writematrix(Final,"pp_np"+radius+".dat",'Delimiter','tab');  
clear;
```